2005-09

Wavelet analysis of bioacoustic scattering and marine mammal vocalizations

Scheidecker, Elizabeth M.

Monterey, California. Naval Postgraduate School

NAVAL POSTGRADUATE SCHOOL

MONTEREY, CALIFORNIA

THESIS

WAVELET ANALYSIS OF BIOACOUSTIC SCATTERING AND MARINE MAMMAL VOCALIZATIONS

by

Elizabeth M. Scheidecker

September 2005

Thesis Advisor:	D. Benjamin Reeder
Co-Advisor:	John A. Colosi

Approved for public release; distribution is unlimited

THIS PAGE INTENTIONALLY LEFT BLANK

REPORT DOCUMENTATION PAGE			Form Approved OMB No. 0704-0188
Public reporting burden for this collection of information is estimated to average 1 hour per response, including the time for reviewing instruction, searching existing data sources, gathering and maintaining the data needed, and completing and reviewing the collection of information. Send comments regarding this burden estimate or any other aspect of this collection of information, including suggestions for reducing this burden, to Washington headquarters Services, Directorate for Information Operations and Reports, 1215 Jefferson Davis Highway, Suite 1204, Arlington, VA 22202-4302, and to the Office of Management and Budget, Paperwork Reduction Project (0704-0188) Washington DC 20503.			
1. AGENCY USE ONLY ***(Leave blank)***	**2. REPORT DATE** September 2005	**3. REPORT TYPE AND DATES COVERED** Master's Thesis	
4. TITLE AND SUBTITLE: Title (Mix case letters) Wavelet Analysis of Bioacoustic Scattering and Marine Mammal Vocalizations			**5. FUNDING NUMBERS**
6. AUTHOR(S) Scheidecker, Elizabeth M.			
7. PERFORMING ORGANIZATION NAME(S) AND ADDRESS(ES) Naval Postgraduate School Monterey, CA 93943-5000			**8. PERFORMING ORGANIZATION REPORT NUMBER**
9. SPONSORING /MONITORING AGENCY NAME(S) AND ADDRESS(ES) N/A			**10. SPONSORING/MONITORING AGENCY REPORT NUMBER**
11. SUPPLEMENTARY NOTES The views expressed in this thesis are those of the author and do not reflect the official policy or position of the Department of Defense or the U.S. Government.			
12a. DISTRIBUTION / AVAILABILITY STATEMENT Approved for public release; distribution is unlimited.			**12b. DISTRIBUTION CODE**

13. ABSTRACT (maximum 200 words)

Wavelets have been used in numerous geophysical studies but few have examined their applicability to underwater acoustic signals. Wavelet transforms can remove noise from a given time series and allow data analysis at multiple levels of resolution. This unique ability is exercised as a feasible application to the signals in this thesis: a reflected scattered signal from a swimbladder-bearing fish, alewife (*Alosa pseudoharengus*), and several *Odontocetes* vocalizations. Both studies reveal that wavelet-based techniques show potential in providing viable information for these acoustic signals despite the lack of statistical analysis. The alewife portion shows a reasonable first order approximation to the absolute target strength and to the time delay correlation caused by the spatial separation of scattering features in the fish. The marine mammal application shows a possible real time method to estimate the mammal's range using the root mean square (RMS) energy of the decomposed signal. Because of wavelet function mismatch, both studies conclude that more extensive research is necessary to develop these techniques into systematic processes.

14. SUBJECT TERMS Wavelets, Acoustic Scattering, Alewife, *Alosa pseudoharengus*, Marine Mammals, Vocalizations, *Odontocetes*.			**15. NUMBER OF PAGES** 115
			16. PRICE CODE
17. SECURITY CLASSIFICATION OF REPORT Unclassified	**18. SECURITY CLASSIFICATION OF THIS PAGE** Unclassified	**19. SECURITY CLASSIFICATION OF ABSTRACT** Unclassified	**20. LIMITATION OF ABSTRACT** UL

NSN 7540-01-280-5500 Standard Form 298 (Rev. 2-89)
Prescribed by ANSI Std. 239-18

THIS PAGE INTENTIONALLY LEFT BLANK

Approved for public release; distribution is unlimited

WAVELET ANALYSIS OF BIOACOUSTIC SCATTERING AND MARINE MAMMAL VOCALIZATION

Elizabeth M. Scheidecker
Lieutenant, United States Navy
B.S., University of South Carolina, 1999

Submitted in partial fulfillment of the
requirements for the degree of

MASTER OF SCIENCE IN METEOROLOGY AND PHYSICAL OCEANOGRAPHY

from the

NAVAL POSTGRADUATE SCHOOL
September 2005

Author: Elizabeth M. Scheidecker

Approved by: D. Benjamin Reeder
Thesis Advisor

John A. Colosi
Co-Advisor

Mary L. Batteen
Chairman, Department of Oceanography

THIS PAGE INTENTIONALLY LEFT BLANK

ABSTRACT

Wavelets have been used in numerous geophysical studies but few have examined their applicability to underwater acoustic signals. Wavelet transforms can remove noise from a given time series and allow data analysis at multiple levels of resolution. This unique ability is exercised as a feasible application to the signals in this thesis: a reflected/scattered signal from a swimbladder-bearing fish, alewife (*Alosa pseudoharengus*), and several *Odontocetes* vocalizations. Both studies reveal that wavelet-based techniques show potential in providing viable information for these acoustic signals despite the lack of statistical analysis. The alewife portion shows a reasonable first order approximation to the absolute target strength and to the time delay correlation caused by the spatial separation of scattering features in the fish. The marine mammal application shows a possible real time method to estimate the mammal's range using the root mean square (RMS) energy of the decomposed signal. Because of wavelet function mismatch, both studies conclude that more extensive research is necessary to develop these techniques into systematic processes.

THIS PAGE INTENTIONALLY LEFT BLANK

TABLE OF CONTENTS

LIST OF FIGURES

ACKNOWLEDGMENTS

Special thanks to CDR Ben Reeder and Professor John Colosi for their support and guidance throughout this challenging project. Your intellect and devotion to acoustics truly stirred my scientific curiosity and motivated me to explore every avenue in search of the true answer.

Special thanks to CDR Carl Hager and Ryan Kinnett for their extreme patience and extensive support in the marine mammal study. Your intellect and devotion to marine mammal research truly stimulated my environmental awareness and further enhanced my dedication to protecting these animals.

Special thanks to Professor Monique Farques for her patience and knowledge of wavelets. Your ideas and suggestions truly put us closer to the results we were anticipating.

Special thanks to Fred Bahr for his knowledge of wavelets and their applications using MATLAB. Without your help, I would not have been able to come as far as I did on this project. I am truly grateful for your patience and advice throughout this entire study.

Special thanks to my son, Cody, for his love and support which inspired me every day to see this project through to the end. Your laughter and smile truly reminded me that any challenge can be overcome by optimism.

THIS PAGE INTENTIONALLY LEFT BLANK

I. INTRODUCTION

Wavelet analysis is gradually becoming a useful tool for analyzing localized variations of energy within a given time series. Originating in the early 1980s for geophysical applications, wavelet analysis allows researchers to isolate and manipulate specific types of trends or patterns hidden in massive amounts of data. By decomposing the time series into frequency-time space, researchers are able to determine the dominant forms of variability and their variations in time.

While the wavelet transform has been used in numerous geophysical studies, including tropical convention, El Nino-Southern Oscillation, the dispersion of ocean waves, wave growth and breaking, and coherent structures in turbulent flows, few studies have examined the usefulness of wavelet transforms on underwater acoustic signals.

Wavelet transforms provide a valuable tool in the removal of noise from a given time series and allow data analysis at multiple levels of resolution. In the process of removing noise, wavelet transforms provide a large variety of flexible basis functions which allow the signal to be projected into a coordinate system where its characteristics are distinguishable from that of the noise. Additionally, allowing data analysis at multiple levels of resolution makes wavelet transforms unique since they permit the user to selectively focus on local signal features or to take global views of the proposed signal to be analyzed.

The unique ability of these transforms is particularly relevant to the two types of acoustic signals studied in this thesis. The first signal type is composed of the reflected scattered signal from a swimbladder-bearing fish, alewife (*Alosa pseudoharengus*), which is a short duration broadband transient. The second signal type is composed of several marine mammal vocalizations from the cetacean suborder *Odontocetes*, which are short duration narrowband tonals.

The purpose of this thesis is an attempt to establish the wavelet process in bioacoustic scattering and marine mammal vocalization itself, not the statistical efficiency of the process. The wavelet denoising and feature extraction methods used in this study are an extension to, and combination of, methods found throughout various

geophysical and signal processing literatures. Chapter II will discuss the brief history of how wavelet analysis came about, an overview of Fourier theory, and the comparison between Fourier transforms and wavelet transforms. Chapter III will give an overview of wavelet theory discussing the two types of wavelet transforms. Chapter IV will briefly discuss the methodology in choosing the appropriate for wavelet function for a given data set and the proposed wavelet applications to the data in this study. Chapter V encompasses the entire alewife study from data collection to discussion of the results. Similarly, Chapter VI encompasses the entire marine mammal study. Chapter VII provides a summary and conclusions.

II. BACKGROUND

A. HISTORY

Geophysical processes are often generated by complex mechanisms which are difficult to characterize. The predictable behavior in such systems such as trends and periodicities are therefore of major interest. Traditional mathematical methods such as Fourier analysis examine periodicities in the frequency domain, implicitly assuming the underlying processes are stationary in time. However, many of these underlying processes are nonstationary in time and require resolution into a spectrum of frequencies. Many believed that the appropriate solution to this intricate dilemma was the Fourier transform. In fact, during the nineteenth century, Fourier transforms solved many problems in physics and engineering which led scientists and engineers to think of them as the preferred way to analyze phenomena of all types.

The major drawback of the Fourier transform, as recognized later in the twentieth century by mathematicians, physicists, and engineers, is that Fourier transforms have trouble reproducing transient signals or signals with abrupt changes. In 1927, the physicist Werner Heisenberg illustrated the principle underlying this problem known as the Heisenberg Indeterminacy Principle (Mackenzie, 2001). He stated that the position and the velocity of an object cannot be measured exactly at the same time. In order to know its frequency, the signal must be dilated in time by a basis function, or vice versa. Therefore, in signal processing terms, it means it is impossible to know simultaneously the exact frequency and the exact time of occurrence of this frequency in a signal (Mackenzie, 2001).

Therefore, the relatively recent development of wavelets has been considered a solution to overcome the shortcomings of the Fourier transform. In general, the disadvantage of Fourier expansion only allows frequency resolution and no time resolution. The fundamental idea of wavelet analysis is to simultaneously capture the low resolution background signal and the high resolution individual, localized variations, a concept which has completely fascinated the scientific, engineering, and mathematics communities. Ultimately, the versatile applicability of wavelets means adopting a whole new perspective in processing data.

However, in order to properly distinguish the advantages of wavelet transforms over Fourier transforms, it is important to recognize that wavelet analysis is easiest to understand as an extension of the more familiar Fourier analysis. Therefore, the remainder of this chapter briefly discusses Fourier theory before leading into the discussion of wavelet theory in chapter III.

B. FOURIER THEORY

1. Fourier Analysis

From Fourier theory, a signal can be expressed as the sum of an infinite series of sines and cosines, commonly referred to as a Fourier expansion. Therefore, any periodic function $x(t)$ with a period of T_0 can be expressed as:

$$x(t) = a_0 + \sum_{n=1}^{\infty} \left[a_n \cos(2p\, nf_0 t) + b_n \sin(2p\, nf_0 t) \right], \tag{2.1}$$

where $f_0 = 1/T_0$ is the fundamental frequency. The term nf_0 represents the n^{th} harmonic of the fundamental frequency. The coefficients a_n and b_n represent the amplitudes of the cosine and sine terms at the n^{th} harmonic of the fundamental frequency and the coefficient a_0 represent the mean value of the periodic signal $x(t)$ over one complete period.

Equivalently, the Fourier series of Eqn. 2.1 can be written in terms of complex exponentials by substituting the exponential forms of the sine and cosine into equation (2.1) to produce the equivalent complex exponential Fourier series:

$$x(t) = \sum_{n=-\infty}^{\infty} C_n e^{j\,2p\,nf_0 t}. \tag{2.2}$$

The terms C_n are the complex Fourier coefficients, and are indicative of the complex weights of the n^{th} harmonic of the complex basis function, $e^{j2p\,nf_0 t}$. These complex coefficients are found from the analysis equation:

$$C_n = \frac{1}{T_0} \int_{-\frac{T_0}{2}}^{\frac{T_0}{2}} x(t)\, e^{-j2p\,nf_0 t} dt \qquad n = 0, \pm 1, \pm 2, \pm 3.... \tag{2.3}$$

Eqn. 2.3 provides the necessary coefficients to exactly reconstruct the periodic signal from its Fourier series expansion. Furthermore, a magnitude spectrum of the periodic

signal $x(t)$ can be created by plotting the magnitude of C_n versus frequency, providing a frequency domain presentation of the signal.

2. Fourier Transform

Analogous to Eqn. 2.3, the Fourier transform of a general continuous function $x(t)$ is:

$$X(f) = \int_{-\infty}^{\infty} x(t)\, e^{-j2\pi ft}\, dt, \tag{2.4}$$

where $X(f)$ is a continuous function of the frequency variable f. Eqn. 2.4 can be derived from Eqn. 2.3 by representing $x(t)$ as a periodic function with infinite period and taking the limit as $T_0 \to \infty$. Since $X(f)$ is continuous, its magnitude spectrum will also be continuous and can be created by plotting the magnitude of $X(f)$ versus frequency.

The original signal $x(t)$ can be reconstructed from $X(f)$ using the inverse Fourier transform:

$$x(t) = \int_{-\infty}^{\infty} X(f)\, e^{j2\pi ft} df\ . \tag{2.5}$$

The two functions, $x(t)$ and $X(f)$, are commonly known as a *Fourier transform pair*.

3. Short-Time Fourier Transform

When a signal is nonstationary, it is advantageous to have a depiction of the signal that involves both time and frequency. However, the Fourier analysis techniques described above provides only a frequency domain representation of the signal and can only be applied to signals whose frequency structure is stationary in time.

An extension of the Fourier transform designed to map a signal into a two-dimensional time-frequency space is the Short-Time Fourier Transform (STFT). The STFT segments a signal into small uniform blocks of time using a sliding window function, $g_{t,f}(t)$. Each block is made short enough so that the signal can be considered stationary within that segment. The Fourier transform is then applied to each time segment to produce the STFT representation specified by:

$$S(t, f) = \int_{-\infty}^{\infty} x(t)\, g_{t,f}(t-t)\, e^{-j2p\, ft}\, dt\,, \tag{2.6}$$

where $S(t, f)$ displays the evolution of the signal's frequency information over time. The plot of the squared magnitude of $S(t, f)$ is called a *spectrogram* and depicts the signal energy in the time-frequency plane.

In practice, many different window functions may be selected which ultimately affect the resulting STFT. The shape of the chosen window function will determine the resolution of the time information (Δt) in the time-frequency plane. Due to the uncertainty principle, the time resolution and the frequency resolution (Δf) of a given signal are inversely related. This produces a trade-off between time resolution and frequency resolution. Because the choice of window fixes Δt over the entire signal length (and also thus Δf), the STFT partitions the time-frequency plane into a uniform grid.

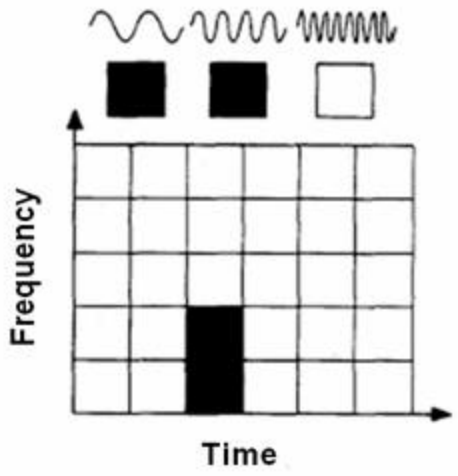

Figure 2.1: Representation of the sliding window function for the Short-Time Fourier transform, the time-frequency grid, and coverage of the time-frequency grid (From Graps, 1995).

The shortcomings of this property is that both Δt and Δf are fixed throughout the analysis of the signal, and cannot simultaneously provide both good time resolution and good frequency resolution, which require short windows and long windows, respectively.

4. Short-Time Fourier Transforms Versus Wavelet Transforms

The difference between the wavelet and the Short-Time Fourier transform (STFT) lies in the shapes of the analyzing functions, $g_{f,t}$ and $\Psi_{l,t}$.

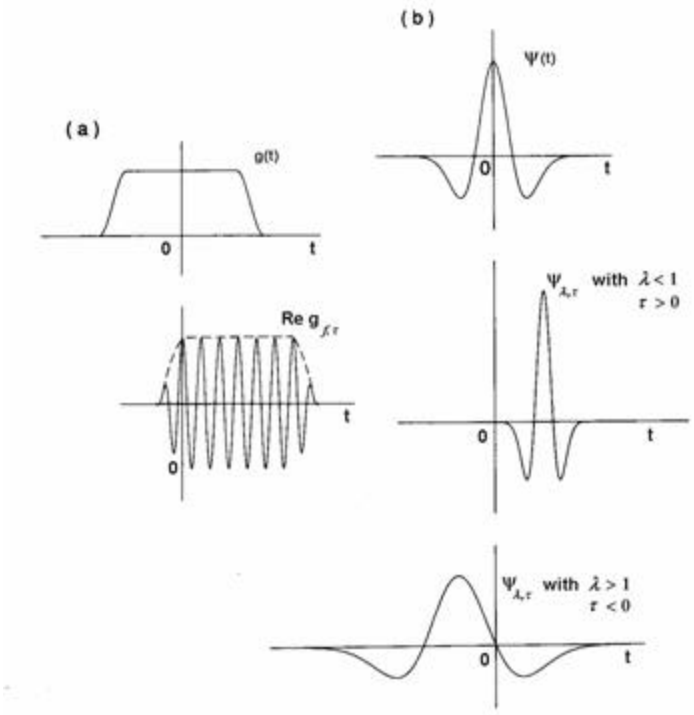

Figure 2.2: Characteristic shapes of the (a) Short-Time Fourier transform analyzing functions, $g_{f,t}$ and (b) wavelet analyzing functions, $\Psi_{l,t}$ along the time (t) axis (From Daubachies, 1992).

The functions $g_{f,t}$ all consist of the same envelope function g, translated to the proper location along the time axis, and "filled in" with higher frequency oscillations (Daubachies, 1992). Regardless of the value of f, all $g_{f,t}$ have the same width in the t direction. In comparison, the $\Psi_{l,t}$ have time-widths adapted to their frequency. High frequency $\Psi_{l,t}$ are very narrow, while low frequency $\Psi_{l,t}$ are much broader.

Recall that the STFT segments a signal into small uniform blocks of time made short enough so that the signal can be considered stationary within that segment.

Wavelets, on the other hand, segment a signal with a fully scalable modulated window which allows for recognition of nonstationary signals within that segment. Consequently, the wavelet transform is better able than the STFT to focus on very short-lived, high frequency phenomena such as transients in signals.

The spectrum is calculated for every position as the window is shifted along the signal. This process is repeated many times with slightly shorter (or longer) windows. The final result is a collection of time-frequency representations of the signal, all with different resolutions.

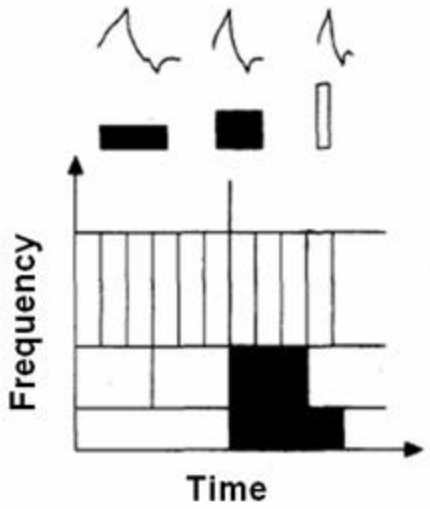

Figure 2.3: Representation of the basis functions for the Daubechies wavelet, time-frequency grid, and coverage of the time-frequency grid (From Graps, 1995).

This type of analysis can be thought of as multi-resolution analysis. In the case of wavelets, the time-frequency representations are actually *time-scale* representations because the scale in a way is the inverse of frequency since the term frequency is reserved for the Fourier transform. Although *scale* is the more general term in wavelet analysis, *scale* will be used interchangeably with *frequency* throughout the remainder of this thesis for convenience.

In general, in addition to overcoming the shortcomings of the STFT with a fully scalable modulated window, there are different shaped wavelets that more closely resemble transient signals and in turn are better able to represent, or decompose, transients of different shapes and types. Some of the various wavelets will be discussed

later in chapter III as well considerations for choosing the proper wavelet for a given data set.

The fundamental concept of wavelet analysis is to analyze data according to scale. Wavelet algorithms process data at different scales or resolutions: if a signal or function is examined through a large window, the gross features are revealed and, similarly, examining the signal or function through a small window will reveal small-scale features.

In general, the wavelet analysis procedure begins with adopting a wavelet prototype function, $\Psi_{l,t}$, commonly known as an *analyzing wavelet* or *mother wavelet*. Temporal analysis is performed with a contracted, high-frequency version of the prototype wavelet, while frequency analysis is performed with a dilated, low-frequency version of the same wavelet. Therefore, each tile of the time-frequency plane represents a single wavelet coefficient computed by applying a basis function centered on that area with the correct aspect ratio between time span and bandwidth.

Because the original signal or function can be represented in terms of a linear combination of the weighted sum of the wavelet functions, data operations can be performed using just the wavelet coefficients. Additionally, if one further chooses the wavelets best adapted to the data, or removes the coefficients below a certain threshold, the data will be scarcely represented, which makes wavelets an excellent tool in the field of data compression.

THIS PAGE INTENTIONALLY LEFT BLANK

III. WAVELET THEORY

There are two distinct classes of wavelet transforms: the continuous wavelet transform (CWT) and the discrete wavelet transform (DWT). The discrete wavelet transform is a compact representation of the data and is particularly useful for noise reduction and data compression, whereas the continuous wavelet transform is better for feature extraction purposes. The remainder of this chapter will discuss the CWT and the DWT in depth and explain their respective applicability in data analysis.

A. CONTINUOUS WAVELET TRANSFORM

The continuous wavelet transform of a function $x(t)$ is defined as the integral transform

$$C(l,t) = \int_{-\infty}^{\infty} x(t)\, \Psi^*_{l,t}(t)\, dt \qquad l > 0, \tag{3.1}$$

where

$$\Psi^*_{l,t}(t) \equiv \frac{1}{\sqrt{l}} \Psi_{l,t}\left(\frac{t-t}{l}\right) \tag{3.2}$$

represents a family of functions called wavelets. In both equations, l is a scale parameter, t is a location parameter on the time axis, and $\Psi^*_{l,t}(t)$ is the complex conjugate of $\Psi_{l,t}(t)$, the *mother wavelet*. Changing the value of l can either have a dilating effect $(l > 1)$ or a contracting effect $(l < 1)$ on $\Psi_{l,t}(t)$, and changing t translates the function $x(t)$ along the time axis. When the scale l decreases, the wavelet becomes more compressed and takes only short time behavior of $x(t)$ in account; when the scale l increases, the wavelet becomes more dilated and considers the behavior of $x(t)$ over a larger time increment. Therefore, the wavelet transform provides a flexible time-scale window that is small for analyzing small-scale features and large for analyzing large-scale features.

One important note is that $\Psi_{l,t}(t)$ has the same shape for all values of l. In addition, lower scales (smaller values of l) correspond to high frequency wavelets and provide good time resolution. Higher scales (larger values of l) correspond to low frequency wavelets with poor time resolution but good frequency resolution. Therefore, in general, the wavelet transform may be considered a mathematical microscope, where the magnification is given by $1/l$ and the optics are given by the choice of wavelet $\Psi_{l,t}(t)$.

The continuous wavelet transform as defined by Eqn. 3.1 is commonly known as "continuous" because the scale and time parameters l and t assume continuous values. The CWT of a function at any arbitrary scale l and location t is obtained by the same basis function as obtained at other scales and locations. Therefore, this type of wavelet transform provides a redundant representation of the signal. Although this transformation is infinitely redundant in theory, it can be useful in recognizing certain characteristics of a signal.

Since the wavelet, $\Psi_{l,t}(t)$, is a function with unit energy, or $\int \left|\Psi_{l,t}(t)\right|^2 dt = 1$, it has two important properties. The wavelet, $\Psi_{l,t}(t)$, is chosen so that it has compact support, or sufficiently fast decay, to obtain localization in space. In other words, $\Psi_{l,t}(t)$ must be a function centered on zero and in the limit as $|t| \to \infty, \Psi_{l,t}(t) \to 0$ rapidly. This condition produces the local nature of wavelet analysis. Additionally, the wavelet, $\Psi_{l,t}(t)$, also has to have zero mean, or $\int_{-\infty}^{\infty} \Psi_{l,t}(t)\, dt = 0$, which is known as the *admissibility condition* of the wavelet. Collectively, these properties ensure that $\Psi_{l,t}(t)$ is a wavelet: the first property ensures that $\Psi_{l,t}(t)$ is not a sustaining wave, while the second property ensures that $\Psi_{l,t}(t)$ is wave-like. Also, in Eqn. 3.2, the normalizing constant, $1/\sqrt{l}$, is chosen so that $\Psi_{l,t}(t)$ has the same energy for all scales l, or $\int_{-\infty}^{\infty} \left|\Psi_{l,t}(t)\right|^2 dt < \infty$.

1. CWT Scalogram

Comparing the time-frequency mapping of the STFT and the CWT, the STFT produces a uniform grid with a constant time resolution and frequency resolution, while the CWT has time resolution and frequency resolution that depend on the scale. Figure 3.3 below depicts the time-frequency grids of the STFT and the CWT.

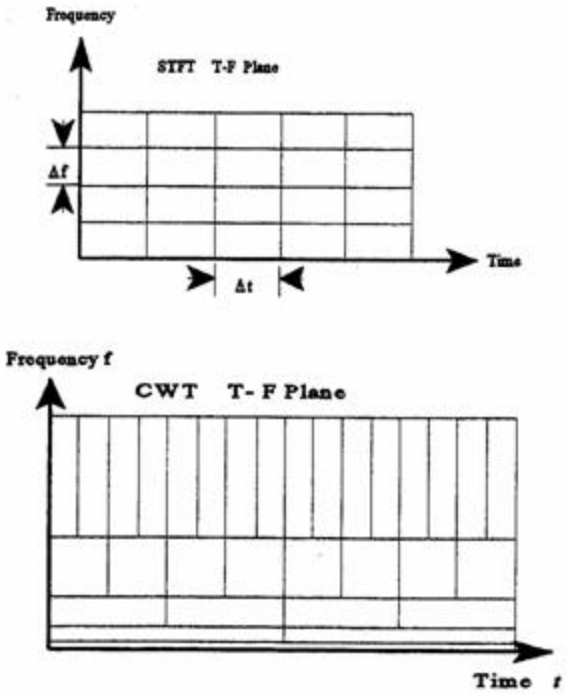

Figure 3.1: Comparison of the STFT spectrogram and the CWT scalogram (From Barsanti, 1996)

Similar to the STFT spectrogram, the CWT scalogram is defined as the squared magnitude of the complex coefficients, $C(l,t)$, and it is a measure of the energy of the signal in the time-scale plane (Barsanti, 1996). A scalogram provides an unfolding of the characteristics of a process in the scale-space plane. The presence of multiscale structures and their temporal locations are easily identified which can reveal some of the embedded small-scale features within the large-scale features.

2. Dilation

The CWT cannot always resolve events in frequency; the same holds true for resolving events in time. Quantitative metrics for time and frequency resolution are based on the *duration* and *bandwidth* respectively of the mother wavelet, $\Psi_{l,t}(t)$ (Rao &

Bopardikar, 1998). The *first moment* of a mother wavelet is given by (Rao & Bopardikar, 1998, Eqn. 1.40)

$$t_0 \equiv \frac{\int_{-\infty}^{\infty} t \left|\Psi_{l,t}(t)\right|^2 dt}{\int_{-\infty}^{\infty} \left|\Psi_{l,t}(t)\right|^2 dt} \tag{3.3}$$

where $\left|\Psi_{l,t}(t)\right|^2 \Big/ \int_{-\infty}^{\infty} \left|\Psi_{l,t}(t)\right|^2 dt$ acts like a probability density function. Therefore, t_0 provides a measure of the position at which $\Psi_{l,t}(t)$ is centered on the time axis.

Similarly, the *first moment* of $\Psi_{l,t}(w)$, the Fourier transform of $\Psi_{l,t}(t)$, makes it possible to find the center of the mother wavelet along the frequency axis, which is given by (Rao & Bopardikar, 1998, Eqn. 1.41)

$$w_0 \equiv \frac{\int_{-\infty}^{\infty} w \left|\Psi_{l,t}(w)\right|^2 dw}{\int_{-\infty}^{\infty} \left|\Psi_{l,t}(w)\right|^2 dw} \tag{3.4}$$

The *root mean square* (RMS) duration of the wavelet is a measure of its duration or spread in time. It is also known as the second moment of the wavelet about t_0, and is defined as (Rao & Bopardikar, 1998, Eqn. 1.42)

$$\Delta t \equiv \sqrt{\frac{\int_{-\infty}^{\infty} (t - t_0)^2 \left|\Psi_{l,t}(t)\right|^2 dt}{\int_{-\infty}^{\infty} \left|\Psi_{l,t}(t)\right|^2 dt}} \tag{3.5}$$

Similarly, the RMS bandwidth of the wavelet is given by (Rao & Bopardikar, 1998, Eqn. 1.43)

$$\Delta w \equiv \sqrt{\frac{\int_{-\infty}^{\infty} (w - w_0)^2 \left|\Psi_{l,t}(w)\right|^2 dw}{\int_{-\infty}^{\infty} \left|\Psi_{l,t}(w)\right|^2 dw}} \tag{3.6}$$

In order to have finite values for the integrals in the numerators in Eqns. 3.5 and 3.6, active decays in time and frequency are required for the wavelet and its transform. If a function does not decay fast enough, alternative measures can be used such as an interval in which the length is equivalent to the substantial energy (approximately 95% of the total energy).

If Δt_Ψ and Δw_Ψ are the RMS duration and bandwidth, respectively, of the mother wavelet, $\Psi_{l,t}(t)$, then the RMS duration of its dilation, $\Psi_{l,0}(t)$, is then $\Delta t_\Psi(l) \equiv |l| \Delta t_\Psi$, and the corresponding bandwidth is $\Delta w_\Psi(l) \equiv \Delta w_\Psi / |l|$. Therefore, the product of the duration and the bandwidth is invariant to the dilation and can be represented as a constant c_Ψ:

$$\Delta t_\Psi(l) \Delta w(l) = \Delta t_\Psi \Delta w_\Psi = c_\Psi \tag{3.7}$$

This equation indicates that decreasing $\Delta t_\Psi(l)$ results in an increase in $\Delta w_\Psi(l)$, and vice versa. The smaller $\Delta t_\Psi(l)$, the better the CWT is able to resolve events closely spaced in time; similarly, the smaller $\Delta w_\Psi(l)$, the better the CWT is able to resolve events closely spaced in frequency. At very small values of l, the RMS duration of the corresponding dilated wavelet is small which allows the CWT to possess good time resolution (or the ability to separate very close events in time). On the contrary, the frequency resolution is poor because the RMS bandwidth of the dilated wavelet is large. For large values of l, the exact opposite is true.

It is then worthy to note that the CWT time resolution improves and the frequency resolution degrades as frequency is increased. Due to the reciprocal relationship between scale and frequency, the CWT provides better frequency resolution at the lower end of the frequency spectrum and poorer resolution at the higher end of the frequency

spectrum. This ability to provide variable time-frequency resolution makes the wavelet transform a natural tool in the analysis of signals.

3. Translation

The CWT also involves the translation of the mother wavelet $\Psi_{l,t}(t)$, along the time axis. Recall that the translation parameter, t, affects only the location of the wavelet and not the duration or bandwidth. From Eqn. 3.3, the first moment and, subsequently, the center of $\Psi_{l,0}(t)$ are $l t_0$. Notice that if $t_0 \neq 0$, the location of $\Psi_{l,0}(t)$ depends on the value of l. Additionally, the first moment of $\Psi_{l,t}(t)$ is $l t_0 + t$. However, the second moment of $\Psi_{l,t}(t)$ about $l t_0 + t$ is the same as the second moment of $\Psi_{l,0}(t)$ about $l t_0$. This indicates that the parameter t merely affects the location of the wavelet and not the RMS duration. Also, the RMS bandwidth is not affected by t because translating a function does not affect the magnitude of its transform.

Figure 3.2 shows the variation of time and frequency resolution as a function of l using *time-frequency cells*. Obtained from the first moments in time and frequency, the center of each rectangle indicates the position of the wavelet in time and frequency. The rectangle itself bounds the spread of the wavelet in time and frequency as characterized by the corresponding second moments.

Given an event at some point (t, w) in the time-frequency plane, for any other event to be resolvable, it should be localized in the time-frequency plane outside the bounding rectangle of the time-frequency cell centered at (t, w) (Rao & Bopardikar, 1998). An alternative view associates the time-frequency cell centered at (t, w) with an ambiguity in localizing events in time and frequency to within its bounding rectangle. From Eqn. 3.7, the area of each bounding rectangle is c_Ψ. Recall that when the time frequency cell is narrow in time, it is wider in frequency. Because this decrease in the uncertainty of time localization is accompanied by an increase in the uncertainty of frequency localization and vice versa, it is impossible to simultaneously reduce the

uncertainty in both directions. Therefore, Eqn. 3.7 demonstrates the *uncertainty principle* governing the time-frequency resolution.

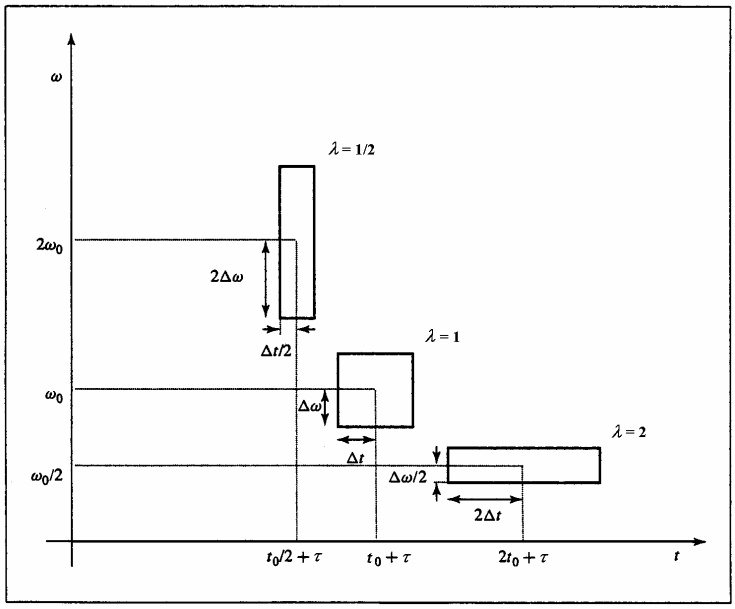

Figure 3.2: Time-frequency cells for $\Psi_{l,t}(t)$ shown for a fixed t and three different values of l. The mother wavelet and its Fourier transform are centered at t_0 and w_0 respectively (From Rao & Bopardikar, 1998).

4. Inverse CWT

The admissibility condition is useful in formulating an inverse continuous wavelet transform, which is defined by

$$x(t) = \frac{1}{C_\Psi} \int_{-\infty}^{\infty} \int_{0}^{\infty} l^{-2} C(l,t) \Psi_{l,t}(t)\, d\, l\, dt, \tag{3.8}$$

where C_Ψ is a constant depending on the choice of wavelet. The inverse CWT reconstructs $x(t)$ once its wavelet transform is known and is a superposition of wavelets, $\Psi_{l,t}(t)$.

B. DISCRETE WAVELET TRANSFORM

For a sampled signal, implementing a wavelet transform requires the scale and location parameters of the CWT be restricted to discrete values. A wavelet transform

invoked on discrete values of scale and location is referred to as a discrete wavelet transform. Using the appropriate choice of wavelet and discretization schemes, one can obtain the nonredundant representation of the sampled signal. Therefore, the DWT of a discrete signal, $x(n)$, is defined as (Barsanti, 1996, Eqn. 3.8)

$$C(a,b) = \sum_{n=1}^{N} \frac{1}{\sqrt{a}} x(n)\, \Psi^{*}\left(\frac{n-b}{a}\right), \tag{3.9}$$

where *a*, *b*, and *n* are the discrete versions of l, t, and t of Eqns. 3.1 and 3.2, respectively. In addition, the scaling factor is even further restricted to

$$a = a_0^{\,J} \qquad\qquad J = 0,1,2,..... \tag{3.10}$$

The accuracy of the signal reconstruction is governed by the choice of a_0 via the inverse transform. The most popular choice, $a_0 = 2$, provides small reconstruction errors and permits the implementation of fast algorithms. By setting $a = 2^J$, octave bands, known as *dyadic scales*, are produced. As J increases, at each scale, the analysis wavelet is stretched in the time domain, and compressed in the frequency domain by a factor of two. Therefore, as a result, an increasing value of J produces more precise frequency resolution and less precise time resolution at each dyadic scale.

Moreover, as J increases, the translation term, b/a in Eqn. 3.9 where $a = 2^J$, becomes smaller and *b* must inevitably increase to cover all translations. As a result, the DWT output grows in length by a factor of two at every scale, producing extremely large DWT vectors at the higher scales. This computational difficultly is alleviated by realizing that at each successive octave, the DWT output contains information at half the bandwidth compared to that of the previous scale, and thus can be sampled at half the rate according to Nyquist's rule (Barsanti, 1996). To accomplish this decimation or subsampling mathematically, the values of the shift parameter *b* are restricted. If $b = k \cdot 2^J$, where k is an integer, and *a* is replaced by 2^J, then the decimated DWT is given as

$$C\left(2^J, k2^J\right) = \sum_{n=1}^{N} \frac{1}{\sqrt{2^J}} x(n)\, \Psi^{*}\left(2^{-J}\left(n-k\right)\right), \tag{3.11}$$

where $J = 0,.....\log_2 N$ and $k = 1,.....N \cdot 2^J$. In the argument of the DWT, the term $k \cdot 2^J$ indicates that the coefficients are decimated by a factor of two at each successive scale J by retaining only the even points. As a result, the coefficients form a $[J \times k]$ matrix. Consequently, each element in the coefficient matrix represents the correlation between the signal and the analysis wavelet at scale J and position k. Rewritten explicitly in terms of parameter J and k, Eqn. 3.6 then becomes

$$C_{J,k} = \sum_n \frac{1}{\sqrt{2^J}} x(n) \Psi^* \left(2^{-J}(n-k)\right), \tag{3.12}$$

and is defined as the decimated DWT equation. Figure 3.4 below shows an example of a discrete wavelet transform, the Symmlet 8 wavelet, at various scales *J* and positions *k*.

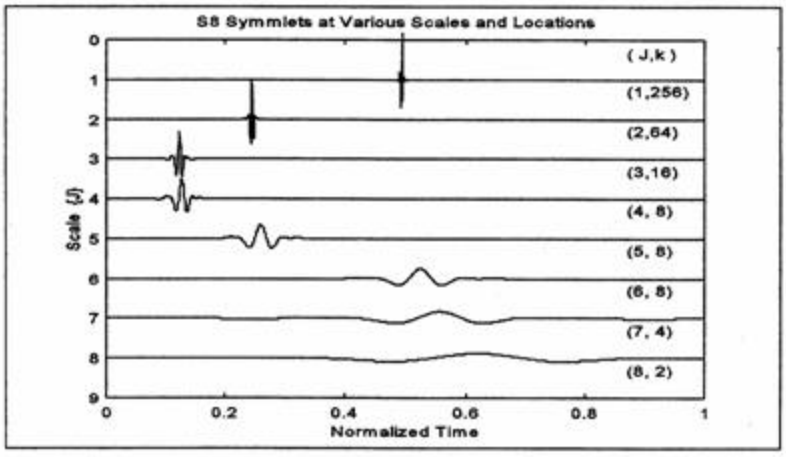

Figure 3.3: Example of a DWT at various scales *J* and positions *k* (From Barsanti, 1996).

1. Mother Wavelet

Dilations and translations of the mother function, or analyzing wavelet, define an orthogonal basis, known as the wavelet basis function:

$$\Psi_{J,k}(n) = 2^{-J/2} \Psi\left(2^{-J}(n-k)\right), \tag{3.13}$$

such that the set of functions $\{\Psi_{J,k}(n)\}$ for all J and k form an orthonormal basis. In addition, the variables J and k are integers that scale and dilate the mother function $\Psi_{J,k}$ to generate a family of discrete wavelets, such as the Daubechies or Symmlets

wavelet families. The scale index J indicates the wavelet's width, and the location index k gives its position.

The most remarkable property of $\{\Psi_{J,k}(n)\}$ is that the functions are orthogonal to their translates and their dilates. From Eqn. 3.13, the mother functions are rescaled, or "dilated" by powers of two and then translated by integers. Due to the self-similarity caused by the scales and dilations, once the unknowns of the mother functions are resolved, everything is known about the basis function at the various J scales and k positions.

2. Scaling Function

To span the data domain at different resolutions, the analyzing wavelet, $\Psi_{J,k}(n)$, is used in a scaling equation defined as

$$j(n) = \sum_{J=-\infty}^{\infty} \sum_{k=-\infty}^{\infty} C_{J,k}\, \Psi_{J,k}(n), \tag{3.14}$$

where $j(n)$ is the scaling function for the mother function $\Psi_{J,k}(n)$, $C_{J,k}$ are the wavelet coefficients that give the discrete sampled values of $j(n)$ at resolution J and location index k, and $\Psi_{J,k}(n)$ is the smoothing function as defined in Eqn. 3.13. Since $C_{J,k} = \int \Psi^*_{J,k}(n)\, x(n)\, dn$, the function $\Psi^*_{J,k}(n)$ acts as a sampling function and is referred to as the "scaling function" of the coefficients. In addition, the first summation from $J = -\infty$ to ∞ is over all scales (from small to large) and at each scale J, the sum from $k = -\infty$ to ∞ operates over all translations.

3. DWT Implementation

The most useful feature of wavelets is its ready adaptation to a given problem. The defined coefficients for a given wavelet are thought of as filters which are placed in a transformation matrix that is applied to a raw data vector. The coefficients are then ordered using two dominant patterns. The first pattern works as a smoothing filter, similar to a moving average. The other pattern works to bring out the data's detailed information.

The DWT of Eqn. 3.12 acts as a complementary pair of low pass (LP) and high pass (HP) filters. These filters equally partition the frequency axis and are known as the

quadrature mirror filters (QMF) or *analyzing filters* (Barsanti, 1996). The output of the LP filter contains the rough shape of the signal while the output of the HP filter contains the details of the signal.

Each filter output only covers half the original frequency range of the input; therefore, both filter outputs can be decimated by a factor of two by retaining only the even points. The combined decimated output of the LP and HP filters are data sets which comprise the DWT coefficients at the first scale. Figure 3.5 depicts the method in which these QMF filters are implemented at scale $J = 1$. Note that $c(n)$ and $d(n)$ are the low pass and high pass output of the signal $x(n)$.

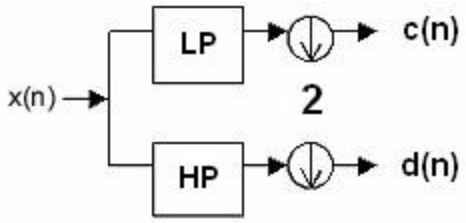

Figure 3.4: Schematic representation of the DWT filtering and downsampling operations on the signal $x(n)$.

By repeating this process on the LP filter output, the signal is further decomposed into the LPLP and LPHP parts at the next scale. The filtering and decimating operations can be continued until the number of samples is reduced to two (Barsanti, 1996). At each successive scale, the frequency range of the output is reduced in half by the LP filter, and the frequency resolution is improved by the decimation. Figure 3.5 shows the resulting transform coefficients in a tree-like structure in which the movement along the tree relates to the lower frequency (higher scale J) coefficients.

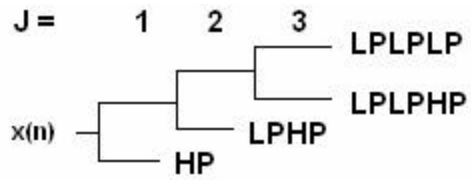

Figure 3.5: Signal $x(n)$ decomposition at higher scales of J.

If the QMF pairs are chosen properly, the decimated DWT as previously described will produce an orthogonal decomposition of the input signal. These filter pairs possess specific mathematical properties and exhibit symmetry characteristics which will be discussed more thoroughly in chapter IV.

Although the DWT filtering operations are linear and time invariant, the decimation combined with the filtering by the DWT results in a time-variant system (Barsanti, 1996). A time invariant system implies that shifts in the system input will not produce an equivalent shift in the system output. Actually, a shift of only a few samples in a signal's starting point can completely change the wavelet decomposition coefficients. This difficulty complicates the performance of signal detection, feature extraction, and classification in the wavelet transform domain (Barsanti, 1996).

Numerous methods have been proposed to deal with the time-variant nature of the discrete wavelet transform. The first method processes multiple time shifted versions of the input and averages the results. This process is known as "cycle spinning". Another method, developed in 1992 by G. Beylkin, calculates all possible circulant shifts of the input signal using a fast algorithm, and averages the results. This process has been shown to be equivalent to the undecimated DWT, and is a non-orthogonal transformation (Barsanti, 1996). A final method is to seek an optimal shift of the input signal. In this process, the transform becomes shift invariant, and orthogonal, but is signal dependent, since the shift is only optimal for the signal under consideration (Barsanti, 1996). However, these enhanced signal denoising techniques are beyond the scope of this thesis.

4. Signal Reconstruction

By reversing the quadrature mirror filtering and down sampling operations, the original signal can be reconstructed from the wavelet coefficients, $C_{J,k}$. The reconstruction of the original signal will be exact only if the QMFs (or wavelets) are properly chosen and exhibit some restrictive mathematical properties which are briefly discussed in Chapter IV. Perfect reconstruction filters of this kind exist, and are constructed by designing another pair of QMFs that perform the upsampling (interpolation) and filtering operations. These *synthesis filters* entirely compensate for any amplitude, phase, and aliasing distortion of the *analyzing filters*. Collectively, the

analysis and synthesis filters form a channel QMF bank and, as a result, the two channel QMF bank behaves like a linear, time-invariant system.

C. WAVELET TYPES

As previously described above, the possibility exists of using several different wavelet functions. Some of the most commonly used wavelets in geophysical applications are the Morlet, the Mexican hat, the Haar, the Daubechies, and the Symmlet wavelets. These are only a few of the many possible wavelets that can be used for data analysis. The purpose of this section is to briefly describe these five wavelets since these were the wavelets used collectively in both studies. Further describing other wavelet types is not pertinent and beyond the scope of this thesis.

In Eqn.3.7, the constant c_Ψ is a function of the wavelet used. Ultimately, a wavelet with a smaller value of c_Ψ will provide better simultaneous localization in the time-frequency plane than a larger value of c_Ψ. One question remains: how small can one make the time-bandwidth product of a function? The smallest time-bandwidth is associated with the Gaussian function, $-e^{-t^2}/2$ and is equal to 1/2. Therefore, the uncertainty principle in Eqn. 3.7 can be restated as

$$\Delta t_\Psi(l)\,\Delta w(l) \geq 1/2. \tag{3.15}$$

Also, it is noteworthy to mention that the Gaussian function itself is not a wavelet; however, its derivatives make sufficient wavelet basis functions for use in data analysis. Both the Morlet and the Mexican hat wavelets are subsets of the Gaussian function and are further described below.

1. Mexican Hat

The Mexican hat wavelet (Fig 3.6) is the second derivative of the Gaussian function and given as (Kumar & Georgiou, 1997, Eqn. 7)

$$\Psi(t) = \frac{2}{\sqrt{3}} p^{-1/4}\left(1-t^2\right)e^{-t^2/2}. \tag{3.16}$$

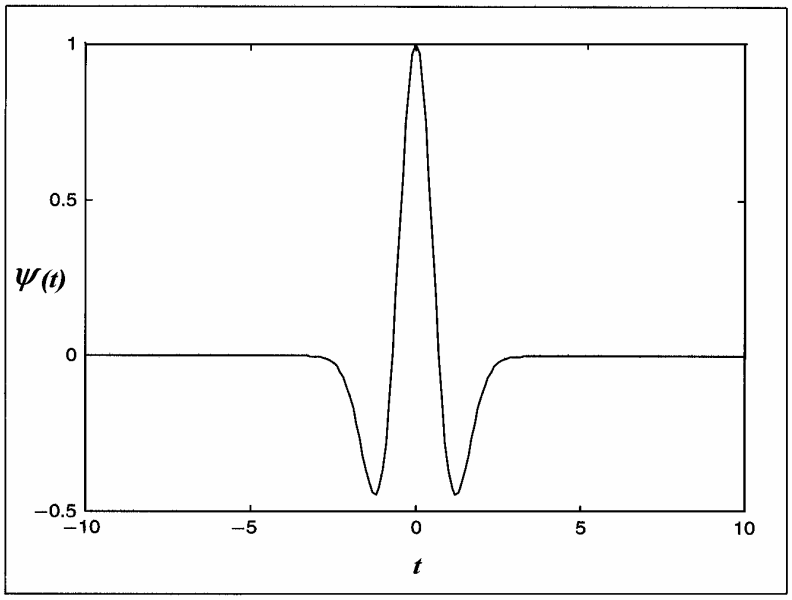

Figure 3.6: The Mexican hat wavelet (From Rao & Bopardikar, 1998).

The Mexican Hat is a real wavelet; therefore its continuous wavelet transform is also real. If the CWT were complex, it would be divided into the real part, $\Re\{C_{l,t}\}$, and the imaginary part, $\Im\{C_{l,t}\}$, enabling one to extract information about the amplitude, $|C_{l,t}|$, and phase, $\tan^{-1}\left[\Im\{C_{l,t}\}/\Re\{C_{l,t}\}\right]$. Since the Mexican Hat wavelet is real, its imaginary part is zero and the phase is undefined, leaving only information about the amplitude.

2. Morlet

The Morlet wavelet is constructed by modulating a sinusoidal function by a Gaussian function and is defined as (Kumar & Georgiou, 1997, Eqn. 8)

$$\Psi(t) = p^{-1/4}\, e^{-iw_0 t}\, e^{-t^2/2}, \qquad w_0 \geq 5. \tag{3.17}$$

This wavelet is complex, which makes its continuous wavelet transform is also complex. Therefore, the CWT can then be divided into the real part, $\Re\{C_{l,t}\}$, and the imaginary part, $\Im\{C_{l,t}\}$, enabling one to extract information about the amplitude, $|C_{l,t}|$, and phase, $\tan^{-1}\left[\Im\{C_{l,t}\}/\Re\{C_{l,t}\}\right]$, of the process being analyzed. It is also not compactly supported, meaning that it is a wavelet of infinite duration. However, as shown in Fig

3.7, more than 99% of the total energy of the function is contained in the interval $|t| \leq 2.5\text{sec}$. Therefore, this confinement of energy to a finite interval makes this function and the Mexican hat wavelet unique and useful for feature extraction purposes.

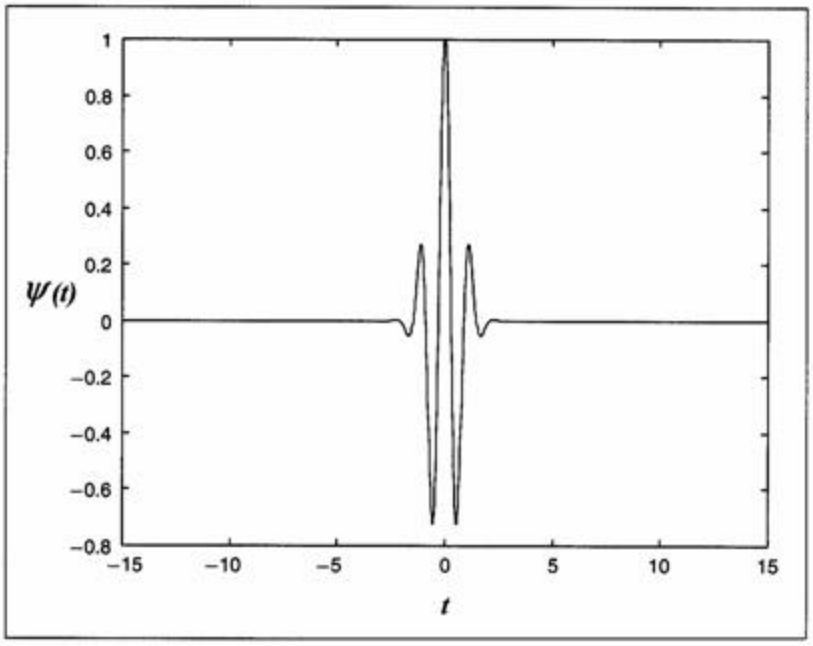

Figure 3.7: Real-value Morlet wavelet (From Rao & Bopardikar, 1998).

3. Haar

The Haar wavelet (Fig 3.8) is a piecewise continuous function defined as (Rao & Bopardikar, 1998, Eqn. 1.10)

$$\Psi(t) = 1, \ 0 \leq t < 1/2 \tag{3.18a}$$

$$\Psi(t) = -1, \ 1/2 \leq t < 1 \tag{3.18b}$$

$$\Psi(t) = 0, \text{ otherwise} \tag{3.18c}$$

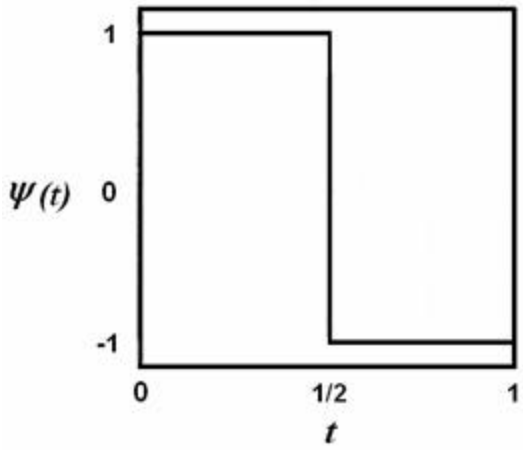

Figure 3.8: Depiction of the Haar wavelet (From Graps, 1995).

The Haar wavelet is a compact, symmetric function that is conceptually simple, fast, and exactly reversible without the edge effects that are a problem with other wavelet transforms.

The Haar wavelet uses a rectangular window to sample a given time series. The first pass over the time series uses a window of two. The window width is then doubled at each step until the window encompasses the entire time series. Each pass over the time series generates a new time series and a set of coefficients. The new time series is the average of the previous time series over the sampling window; therefore, the coefficients represent the average change in the sample window.

In generating each set of averages for the next level and each set of coefficients, the Haar transform performs an average and difference on a pair of values. Then the algorithm shifts over by two values and calculates another average and difference on the next pair. Normally, the high frequency coefficient spectrum should reflect all high frequency changes. Since the Haar window is only two elements wide, any change that takes place from an even to odd value will not be reflected in the high frequency coefficients.

4. Daubechies

The Daubechies wavelet (Fig 3.9) is not an infinite basis function; unlike the Morlet or Mexican Hat wavelet, they have the value of zero everywhere outside a certain interval or support commonly referred to as *compact support*. Additionally, the

Daubechies wavelet is a continuous function that cannot be constructed from analytic formulas like the previously mentioned wavelets. These wavelets are thought to be creatures of the computer age and are made using an iterative process.

Daubechies wavelets are also very *asymmetric* wavelets; therefore, any filter associated with this wavelet will have their energy concentrated near the starting point of their support. Thus, the magnitude of its wavelet transform is large at the center of any signal variation.

Unlike the Haar wavelet, the Daubechies wavelet algorithm uses overlapping windows so that the high frequency spectrum reflects all changes in the time series. Although the Daubechies also shifts by elements of two at each step, the average and difference are calculated over four elements so that no high frequency changes are missed.

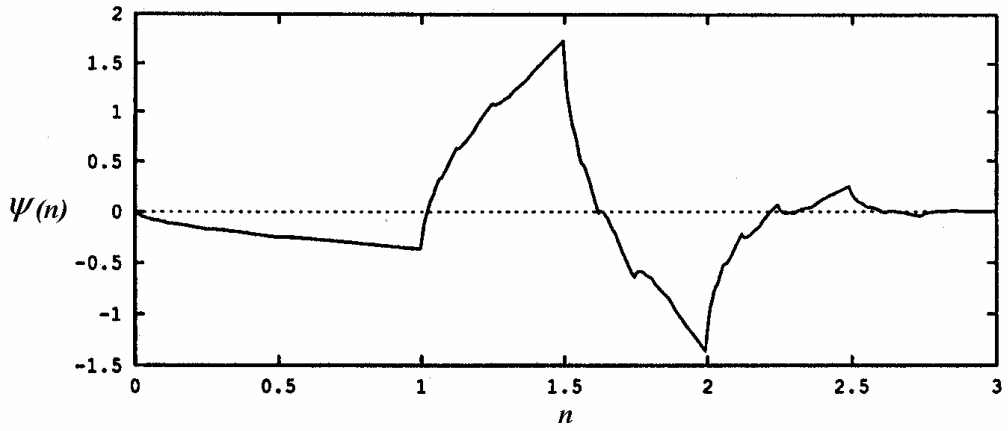

Figure 3.9: Depiction of the Daubechies wavelet (From Chui, 1992).

5. Symmlets

The Symmlet wavelet (Fig 3.10) is similar to the Daubechies wavelet in that it is a compact, continuous wavelet that cannot be constructed from analytic formulas. The main difference is the Symmlet wavelet is nearly symmetric; thus, any filter associated with this wavelet will have their energy not as concentrated near the starting point of their support. Thus, the magnitude of its wavelet transform will be larger near the boundaries of any signal variation.

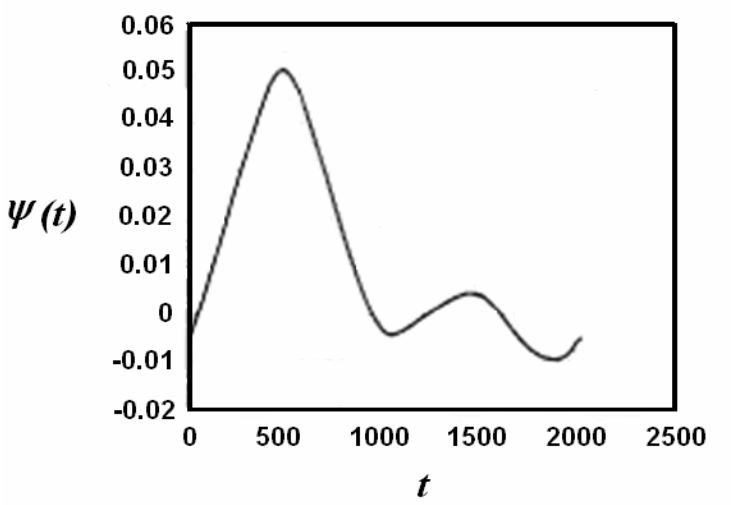

Figure 3.10: Depiction of the Symmlet wavelet (From Graps, 1995).

IV. CHOOSING THE PROPER WAVELET

Wavelet analysis has been criticized for its seemingly arbitrary choice of the wavelet basis function $\Psi_{l,t}$. Consequently, the choice of the transform and of the appropriate wavelet is dictated by the goals of the analysis and the kind of information the user wants to extract from the signal. In the end, wavelet selection plays an important role in the results obtained by wavelet analysis.

As previously discussed, in general, the continuous wavelet transform is better suited for analyzing purposes because its redundancy allows a clear representation of the signal's characteristics. The orthogonal discrete wavelet transform or the newly developed wavelet packet technique are preferable for compression or modeling purposes because they decompose the signal into a minimal number of independent coefficients. But, the different categories and various types of the analyzing wavelet provide a host of options when analyzing a specific process of interest. Selecting the most appropriate basis function requires a thorough comparison of these options and consideration of several factors. The remainder of this chapter will discuss the process of choosing the appropriate wavelet for a given data set.

A. WAVELET PROPERTIES

1. Orthogonal Versus Nonorthogonal Wavelets

In general, orthogonality is a feature of complex exponential signals of different frequency. In mathematics, two vectors are considered orthogonal if their inner product is zero, and therefore, it is customary to think that these vectors are at right angles to one another. However, the waveforms have no obvious direction. Thus, orthogonality simply means that their inner product is zero, or $\langle x_1 | x_2 \rangle = 0$.

The choice between orthogonal and nonorthogonal wavelets is guided by the considerations of the role of redundancy. The use of an orthogonal basis function implies the use of the discrete wavelet transform (DWT) while a nonorthogonal basis function implies the use of either the discrete or continuous wavelet transform (CWT).

When the user needs quantitative information about the data set, often the orthogonal wavelets provide the best choice. In orthogonal wavelet analysis, the number

of convolutions at each scale is proportional to the width of the wavelet basis function at that scale (Torrence & Compo, 1998). Subsequently, this produces a wavelet spectrum containing discrete segments of wavelet power. An orthogonal basis function is useful for signal processing as it gives the most compact representation of the signal and allows for perfect reconstruction of the original signal. However, the difficulty in using orthogonal wavelet functions in time series analysis is any aperiodic shift in the time series produces a different wavelet spectrum.

Conversely, nonorthogonal wavelet analysis is highly redundant at large scales, where the wavelet spectrum at adjacent times is highly correlated (Torrence & Compo, 1998). Therefore, in applications such as noise suppression, redundant representation of wavelet frames is an appropriate choice. Nonorthogonal wavelets are useful when qualitative or exploratory analysis is required at small increments of scale. This is merely due to their ability to perform analysis at scales that are finer than dyadic increments. Thus, nonorthogonal wavelets are useful for time series analysis because any aperiodic shift will not produce a different wavelet spectrum. Therefore, only smooth, continuous variations in wavelet amplitude can be expected.

2. Real Versus Complex Wavelets

Generally speaking, real wavelets cover both measurements in the (J,k) plane and are often used to detect sharp signal transitions. A real wavelet transform is complete and conserves the energy of the signal, as long as the wavelet satisfied the admissibility condition, discussed previously in Chapter III. A real wavelet function returns only a single component and can be used to isolate peaks or discontinuities (Torrence & Compo, 1998). Therefore, in time series analysis, a real wavelet function captures both the positive and negative oscillations as separate peaks in the wavelet power spectrum or scalogram.

On the contrary, a complex wavelet transform expands a signal in terms of complementary real and imaginary parts, which allow the separation of the magnitude and phase of the data. Thus, a complex wavelet function will return information about both amplitude and phase and is better adapted for capturing oscillatory behavior, which is then more easily interpreted. Recent complex wavelet methods are believed to offer a

useful combination of properties: perfect reconstruction, greater directional selectivity, and a natural multiscale decomposition.

3. Smooth Versus Irregular Wavelets

In time series analysis, the wavelet basis function $\Psi_{l,t}$ should reflect the type of features present in the prescribed data set. If the user is primarily interested in wavelet power spectra, then the choice of the wavelet basis is not critical, considering one basis function will give the same qualitative results as another.

On the contrary, an irregular or discontinuous wavelet such as the Haar wavelet often provides a good and simple choice for time series with sharp variations. For smooth-varying or continuous time series, one would choose a smooth function such as a damped cosine.

4. Symmetric Versus Antisymmetric Wavelets

By definition, symmetric wavelets are those basis functions in which computations which begin from the right-hand side will yield the same results as those which begin from the left. More importantly, to define symmetric wavelets, the pair of filter coefficients used to move to a coarser resolution level will be different from the pair used to move to a finer resolution level. When using a symmetric wavelet, the magnitude of the wavelet transform is large at the boundaries of the variation. Therefore, the user cannot emphasize any sharp transitions in a signal and should reserve a symmetric wavelet for a continuous signal.

On the contrary, wavelets that are not perfectly symmetric, or antisymmetric, mean that approximations for these functions are ones in which computations beginning from the right-hand side will yield different results than those which begin from the left. Therefore, when using an antisymmetric wavelet, the magnitude of the wavelet transform is large at the center of the variation. Overall, this shows that the user can emphasize a region either of sharp transition or of stationary activity by the appropriate choice of wavelet function.

B. WAVELET PARAMETERS

1. Localization

When strong localization properties are desired for applications in filtering, the choice of the wavelet basis function should be guided by considering the spectral properties of the function itself. In order to localize variations in time or frequency, it should be known that the resolution of a wavelet function is determined by the balance between the width of the basis in real space and the width in Fourier space. The width of a wavelet function is defined as the *e*-folding time of the wavelet amplitude (Torrence & Compo, 1998). This e-folding time is chosen so that the wavelet power for a discontinuity at the edge drops by a factor of e^{-2} and ensures that the edge effects are negligible beyond this point (Torrence & Compo, 1998). Consequently, a narrow wavelet function in time will have good time resolution but poor frequency, while a broad wavelet function has poor time resolution aside from good frequency resolution. Ultimately, the user must determine what is more important to resolve based on the prescribed goal of their study and choose a basis accordingly.

2. Scales

Once a wavelet basis function is chosen, choosing a set of scales, l and *a*, to use in the wavelet transform Eqns. 3.1 and 3.9 is an essential part of the analysis. For the continuous wavelet transform (or nonorthogonal wavelet), the user can utilize an arbitrary set of scales to build a more complete picture of their data set. In the case of the discrete wavelet transform, the user is limited to a discrete set of scales as discussed previously in chapter III and by Farge (1992).

Additionally, for a discrete-time signal, $x(n)$, the scaling operation by an arbitrary factor is not well-defined, making it difficult to obtain an unambiguous interpretation of scaling in the discrete-time domain. Upsampling, interpolation, downsampling, and fractional sampling rate alteration can have scaling interpretation, but cannot handle all possible scaling factors. Therefore, Rao & Bopardikar (1998) presented a different approach to discrete-time scaling that can handle continuous scaling factors. Because the scaling operations in continuous time are well defined, their approach defined discrete-time scaling operations in a way that effectively converts $x(n)$ into a

continuous-time signal through invertible mapping, applying the scaling operation to the continuous-time signal, and finally inverse transforming the signal back to the discrete-time domain.

Torrence & Compo (1998) showed that the peak amplitude of a wavelet function does not necessarily occur at a frequency of l^{-1} and a^{-1} for the continuous and discrete wavelet function, respectively. Meyers et al. (1993) developed a method to determine the relationship between the equivalent Fourier period and the wavelet scale. This relationship can be derived analytically for a particular wavelet function by substituting a cosine wave of a known frequency into Eqns. 3.1 and 3.9, respectively, and computing the scale at which the wavelet power spectrum reaches its maximum.

Therefore, the user should certainly convert from scale to Fourier period prior to plotting the wavelet power spectrum; especially since the user is certainly interested in equating the wavelet power at a certain time and scale at the equivalent Fourier period.

C. WAVELET CHOICE

The purpose of this thesis is to apply wavelets to acoustic signals scattered by marine organisms and to marine mammal vocalizations. Since the Mexican hat wavelet and the Morlet wavelet are considered unique and useful for feature extraction purposes, these wavelets will be applied to the received backscattered voltage signal (v_{bs}^{R}) as acquired in the study by Reeder *et al*. (2004) to further aid in describing the scattering characteristics of fish. Both wavelets are non-orthogonal, symmetric continuous wavelets and were chosen to find variations in v_{bs}^{R} in order to determine the absolute target strength as a function of angle.

In addition, the Daubechies and Symmlet wavelets will be applied to the same signal (v_{bs}^{R}) for the purpose of correlating the time between the multiple arrivals of a high frequency chirp to the spatial separation of the scattering features of the fish. Both wavelets are orthogonal, anti-symmetric discrete wavelets and were chosen to give the most compact representation of the signal and to emphasize sharp transitions in the received backscattered voltage signal (v_{bs}^{R}).

In the marine mammal study, the Haar wavelet was applied to several vocalizations in order to determine the root mean square (RMS) energy of the signal as a function of range from the passive receiver. This wavelet is a nonorthogonal, symmetric discrete wavelet and was chosen to decompose each vocalization to determine its relative amplitude as received on four separate hydrophones.

V. ALEWIFE STUDY

A. BACKGROUND

In ecology, traditional methods of surveying marine organisms such as direct sampling with nets furnishes biological data such as abundance, biomass, direct measurements of organism size and species identification. However, these methods encounter various problems such as net avoidance, small sampling volumes, and catch destruction of delicate specimens. Acoustically surveying ecologically important organisms could avoid these problems, especially in the case of large-scale synoptic surveys that require high resolution data. While acoustic sampling does not directly produce biological data like the traditional methods, inference of biological information from acoustic scattering by the marine organism requires an understanding of the process by which the organism scatters sound.

Detailed investigations into the scattering mechanisms of marine organisms are required in order to determine and decipher the extent to which the various anatomical features contribute to the overall scattering characteristics (Reeder *et al.*, 2004). For example, understanding the scattering mechanisms of fish is challenging because the fish anatomy is unmistakably complex which makes the acoustic scattering characteristics of the fish equally complex. Therefore, studies must embody careful, accurate measurements of the acoustic scattering and associated modeling to effectively illustrate these mechanisms. Considering the ample number of organisms that live in the ocean, it is nearly impossible to study the scattering by all species. Nevertheless, marine organisms generally can be categorized by morphological groups. For example, fish can be grouped by its morphological characteristics, such as size, shape, and the presence or absence of swimbladders.

In the past, various studies have focused on measurements and modeling of acoustic scattering by fish at single frequencies or more precisely, frequencies within a narrow band. Although these have proven to be successful in surveying common fish species, the relationships are not predictive or cannot be applied directly to other fish types (Reeder *et al.*, 2004).

Additionally, various analytical and numerical acoustic scattering models have been developed that are predictive but are limited in regards to frequency range, surface types, boundary conditions, eccentricity of shape, and numerical efficiency. Generally these models only encompass the swimbladder as the dominant scatterer while excluding all other body parts. Ignoring other body parts works well for angles of incidence near the main lobe of scattering or angles near normal incidence to the surface of the swimbladder. However, as the angles move away from the main lobe of scattering, there is a potential for the models to underpredict the scattering where other organs may contribute significantly to the echo (Reeder *et al.*, 2004).

In order to successfully use acoustics in ocean observations, scattering models should be accurate for each category of animal. In addition, these models require testing and refinement through accurate, extensive measurements of scattering from fish as well as reliable algorithms for numerical implementation of the models. More importantly, advanced scattering models must include shapes that closely resemble the dominant scattering features within the fish, which require high resolution morphological measurements of the fish to be made. Finally, the most important requirement is that the acoustic scattering measurements are conducted over a wide range of frequencies, preferably with continuous coverage over the frequency band.

Despite the need for broad spectral coverage, the majority of acoustic measurements on fish are in terms of target strengths at single frequencies. Although this information has been continually proven to be useful for specific applications, such as fishery population estimates, traditional target strength measurements lack spectral coverage for rigorous model development (Reeder *et al.*, 2004). More specifically, narrow-band measurements of fish are limited to separate frequencies. This restricts the ability to measure frequency-dependent scattering mechanisms by the use of multiple discrete frequencies.

Considering an animal's scattering properties vary considerably with the frequency of the transmitted signal, the use of broadband transducers offers continuous coverage over a significant range of frequencies. This will inherently increase the amount of information contained in the signal. Additionally, the broadband signals have high temporal resolution which can be recognized through the use of an impulse signal or

pulse compression of a longer signal. Therefore, with high temporal resolution, scattering features can possibly be resolved in time and identified.

In spite of the considerable advantages of broadband signals, relatively few studies have investigated or exploited the animal's spectral characteristics. Reeder *et al*. (2004) addressed the need for broadband acoustic measurements and advanced scattering models that incorporated high-resolution morphology. A portion of this study conducted extensive broadband acoustic measurements on live, adult alewife (*Alosa pseudoharengus*) that were tethered while being rotated in 1-deg increments of orientation angle over all angles in two planes of rotation (lateral and dorsal/ventral) (Fig 5.1).

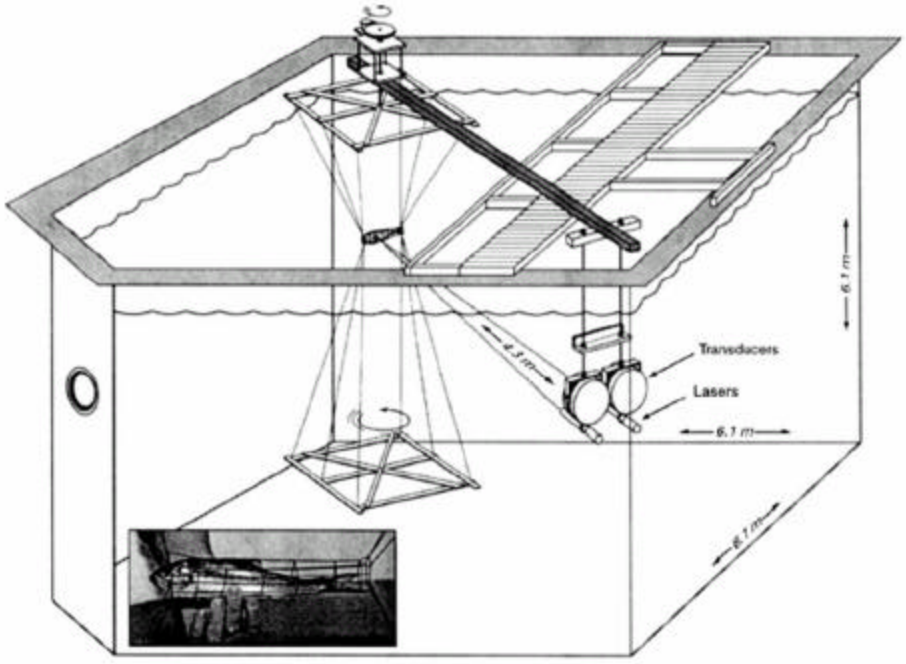

Figure 5.1: Schematic representation of the laboratory system used in measuring the acoustic backscattering by live, individual alewife as a function of angle orientation and frequency (From Reeder *et. al.*, 2004).

The spectral and time-domain analyses of these measurements identified dominant scattering features of the alewife as well as demonstrated the extent to which the scattering depends on size, shape, acoustic frequency, and orientation angle. This study also utilized traditional x-rays and advanced techniques involving computerized tomography (CT) scans to rapidly and noninvasively image the anatomy of the fish so that digitizations of swimbladder shape could be incorporated into two scattering models.

These two models were the KRM (Kirchhoff-ray mode) model which used the traditional x-rays to image the fish anatomy, and the Fourier matching method (FMM) for axisymmetric finite-length bodies, a newly developed scattering formulation which used the newly developed PCX process (CT scans) to image the fish anatomy (Fig 5.2). This high resolution imagery from the PCX process contains much finer detail than the traditional x-rays which dramatically aids the determination of the scattering features in fish.

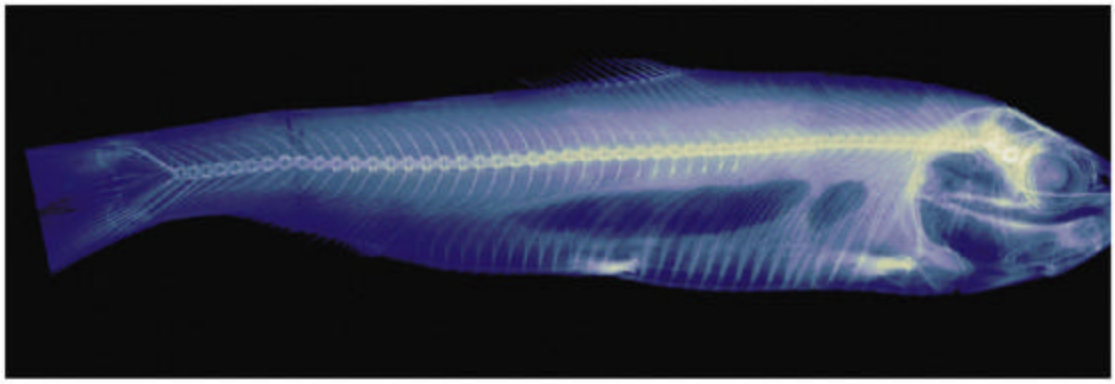

Figure 5.2: Phase-contrast x-ray (PCX) of an alewife. This extremely high-resolution imaging technique is sensitive to, and illustrates well, the small-scale anatomical features of the alewife such as fins, ribs, striations in muscle tissue, gills, and weakly scattering soft tissue (From Reeder *et al.*, 2004).

The remainder of this chapter will briefly discuss the acoustic data acquisition from Reeder *et al*. (2004), the methodology using wavelets to examine the acoustic scattered signal characteristics, the results of the proposed methodology and a thorough discussion of these results, and recommendations for further research.

B. ACOUSTIC DATA ACQUISITION

Reeder *et al*. (2004) chose alewife for their study because they are readily caught and are similar to the commercially and ecologically important fish, the Atlantic herring (*Clupea harengus*), in their body size, shape, and swimbladder construction. Both fish expand and contract their swimbladders primarily by transferring air through a pneumatic duct between their esophagus and swimbladder.

The acoustic backscattering measurements were conducted in a large freshwater tank as shown in Fig 5.1. The experimental setup included the use of a power amplifier, signal generator, a pair of transducers, preamplifier, signal generator, a pair of

transducers, preamplifier, bandpass filter, digital oscilloscope, and personal computer. All data was acquired at a 4-MHz sampling rate by the oscilloscope. During the measurements, the individual fish was secured in an acoustically transparent harness in the center of the acoustic beam and rotated (Fig 5.1 insert). Reeder *et al*. (2004) noted that the fish was alive and well throughout the entire experiment.

A pair of Reson TC2116 broadband acoustic transducers was mounted horizontally in the tank facing the fish in the tethering system. The center of the transducers was attached to a computer-controlled stepper motor which rotated the assembly in 1° increments through two full rotations, resulting in individual data sets with 720 pings. The two transducers were identical and closely spaced approximating a monostatic configuration; one was used as the transmitter and one as the receiver. Reeder *et al*. (2004) explained that using two transducers allows closer scattering ranges, minimal effects of transmitter ringing, and ease in calibrating the system.

Reeder *et al*. (2004) insonified the fish with a shaped chirp signal in a frequency spectrum ranging from 40 to 95 kHz at a constant range of $r_{bs} = 4.3\,m$ for a duration of 600 *m*sec. The transmitted signal was shaped to make the composite response of the transducer pair approximately uniform over the usable bandwidth. Additionally, the transmitted voltage time series, $v_{bs}^{T}(t)$, and the received time series (the backscattered return echo from the fish), $v_{bs}^{R}(t)$, were stored on a personal computer for further analysis.

Reeder *et al*. (2004) carefully calibrated the system prior to each set of backscattering measurements by mounting the transducers facing each other, separated by a range of $r_{cal} = 4.1\,m$. The shaped chirp, transmitted calibration voltage signal, $v_{cal}^{T}(t)$, and the average of hundreds of received calibration voltages, $v_{cal}^{R}(t)$, were stored on the computer and used later in calculating the absolute target strength of the fish (Fig 5.3).

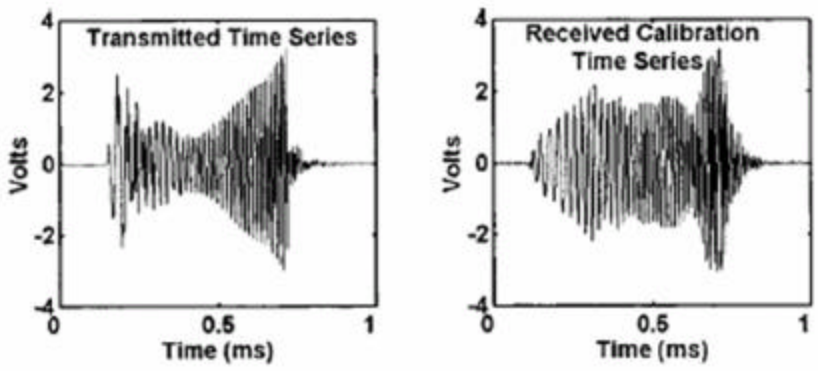

Figure 5.3: Broadband chirp signals of the transmitted calibration voltage signal (v_{cal}^{T}) (left) and the received calibration voltage signal (v_{cal}^{R}) (right) used during the calibration process. The transmitted signal waveform (v_{bs}^{T}) was also used during the scattering experiment (From Reeder *et al.*, 2004).

The first step in calculating the absolute target strength requires computing the magnitude of the scattering amplitude of the fish, $|f_{bs}|$, for each ping given by (Reeder *et. al.*, 2004, Eqn. 12)

$$|f_{bs}| = \frac{V_{bs}^{R}}{V_{cal}^{R}} \frac{V_{cal}^{T}}{V_{bs}^{T}} \frac{r_{bs}^{2}}{r_{cal}}, \tag{5.1}$$

where V_{bs}^{R}, V_{bs}^{T}, V_{cal}^{R}, and V_{cal}^{T} are the absolute values of the Fourier transforms of the bandpass filtered voltage signals v_{bs}^{R}, v_{bs}^{T}, v_{cal}^{R}, and v_{cal}^{T}.

Due to the large dynamic range of the scattering amplitude, the backscatter is often expressed in logarithmic terms as target strength (TS), expressed in units of decibels (dB) relative to 1 m and given by (Reeder *et. al.*, 2004, Eqn. 2)

$$TS = 10\log_{10}|f_{bs}|^{2} = 10\log_{10} s_{bs}, \tag{5.2}$$

where $s_{bs} \equiv |f_{bs}|^{2}$ is the differential backscattering cross section. Note that s_{bs} differs from the often-used backscattering cross section, s by a factor of $4p$ ($s = 4ps_{bs}$).

C. METHODOLOGY

The purpose of this portion of the thesis was to apply the wavelet transform to the received backscattered voltage signal (v_{bs}^{R}) as acquired in the study by Reeder *et al.* (2004) to further aid in describing the scattering characteristics of the fish. Since broadband signals through the matched filter process provide high temporal resolution and, as a result, allows the scattering features of fish to be resolved in time, applying the wavelet transform in Eqn. 5.1 instead of the Fourier transform has been considered a possible analogous method to the one defined in Reeder *et al.* (2004). One immediate difference when comparing the previous method and the proposed wavelet method is wavelets further resolve these features in time and at the same time in frequency, while the Fourier transform method defined in Reeder *et al.* (2004) resolved only the features in frequency. The objective in this chapter is to test this proposed wavelet method as well as display any other spectral characteristics as derived from applying the wavelet transform. The remainder of this section will describe the development of the proposed method; the remaining sections of this chapter will discuss the results and the recommendations for further research.

MATLAB version 7.0 is a computational software package distributed by The MathWorks, Inc. which contains a wavelet toolbox with numerous built-in functions to be used for mathematical and scientific computing. For this study, the received backscattered voltage signals (v_{bs}^{R}) were processed via the built-in continuous and discrete wavelet functions in this toolbox.

1. Absolute Target Strength

Reeder *et al.* (2004) discusses partial wave target strength (PWTS) which highlights the characteristics of selected portions of the backscattered signal and the interactions between the multiple arrivals within the portions which apparently cause the interference patterns in the spectral plots (Fig 5.4). Through pulse-compression processing, the individual arrivals from the different parts of the body are resolved, resulting in several significant scattering features being extracted from the received backscattered signal.

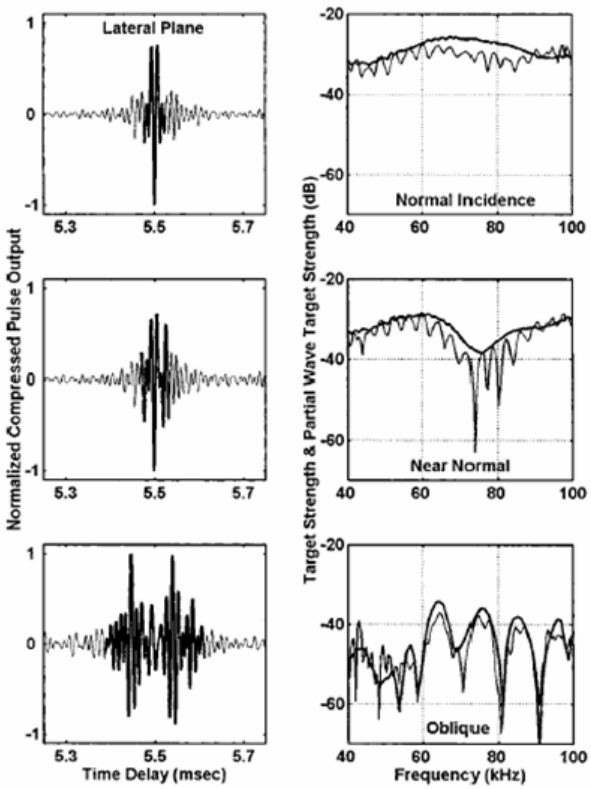

Figure 5.4: Normalized compressed pulse output (CPO) of v_{bs}^{R}, target strength, and the PWTS of the alewife at three different orientations (one ping per orientation) in the lateral plane. The target strength (TS) was computed from the whole time series (thin lines in the plots on the right) and the PWTS (thick lines in the plots on the right) was computed from the thick-lined (time-gated) portions of the time series on the left (From Reeder *et al*., 2004).

As the fish's orientation changes, the constructive and destructive interferences between the multiple arrivals vary according to the separation of the scattering features (relative to the transducers) with respect to the wavelength of the sound. At the angle of normal incidence, the multiple arrivals are in phase and add coherently, resulting in a relatively flat response over the band (Fig 5.4, top right). As the angle orientation moves away from normal incidence, the arrivals add less coherently, causing the individual waves to add destructively at certain frequencies. The result is a series of peaks and nulls in the target strength over the frequency band (Fig 5.4, bottom right).

If the multiple arrivals are analyzed separately, the interference mechanism can be further explained (Fig 5.5).

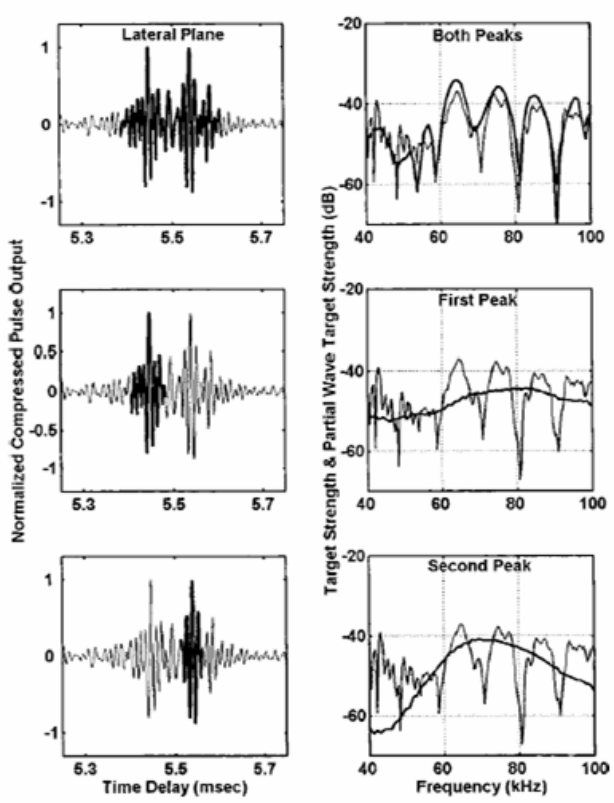

Figure 5.5: Normalized CPO of v_{bs}^{R}, target strength, and PWTS for the alewife in the lateral plane at the same oblique angle of orientation, but representing processing of different segments of the CPO. The top pair of plots is the same as the bottom pair in Fig 5.10 for reference, while the lower two rows illustrates the characteristics of the separate arrivals (From Reeder *et al*, 2004).

Reeder *et al*. (2004) demonstrated that the PWTS of the individual first and second major arrivals at oblique angles exhibit frequency responses that were smooth and relatively slowly varying compared with that of a combination of the two arrivals. This further illustrated the hypothesis that these resolved echoes were due to multiple singular scattering features which make significant contributions to the overall received scattered signal.

In an attempt to further illustrate the above hypothesis, two different continuous wavelet transform (CWTs) were applied to each signal, v_{bs}^{R}, to further extract scattering features of the fish: the Morlet wavelet and the Mexican hat wavelet. The CWT has problems at the beginning and end of the time series due to edge effects. This can create wrap around effects which will misrepresent the wavelet power spectrum associated with

a given signal. Torrence and Compo (1998) mention that it is useful to a pad a signal with zeroes to avoid such effects as well as pad up to a power of two as this makes the transform go faster. Therefore, each received backscattered signal (v_{bs}^{R}) containing 6000 points was first padded with zeroes up to 8192 (2^{13}) points. In addition, the transmitted signal (v_{bs}^{T}), the transmitted calibrated signal (v_{cal}^{T}), and the received calibrated signal (v_{cal}^{R}) were padded with zeroes for the same reason up to 8192 points.

The result of applying these CWTs to a given time series in MATLAB is the calculated amplitude of the wavelet coefficient at each corresponding scale and time. Torrence and Compo (1998) define the wavelet power spectrum as the coefficient amplitude squared, or $\left|C_{l,t}\right|^{2}$. Thus, these amplitudes can then be represented in a scalogram shown later in this chapter to display the wavelet power spectrum at the corresponding scale and time.

Mathematically, the calculated coefficient amplitudes form a matrix in which the number of columns is associated with the number of points in time in the signal and the number of rows is associated with the prescribed number of scales. For example, the received backscattered signal (v_{bs}^{R}) with 8192 points analyzed over 100 scales would result in a 100×8192 matrix. To produce an analogous wavelet method to the Fourier method described in Reeder *et al*. (2004), the absolute value of the coefficient amplitudes in each row were summed up and divided by the number of points in the original signal (6000) to produce the normalized backscattered energy amplitude at that scale. Overall, this was done for every row and, as a result, produced the normalized backscattered energy spectrum, V_{bs}^{R}, over all scales. This process was done for the received backscattered signal at every angle (1-720).

In order to calculate the scattering amplitude in Eqn. 5.1, the same process as described for the received backscattered signal (v_{bs}^{R}) was also done for the transmitted signal (v_{bs}^{T}) resulting in the normalized energy spectrum, V_{bs}^{T}; the transmitted calibrated signal (v_{cal}^{T}) resulting in the normalized energy spectrum, V_{cal}^{T}; and the received

calibrated signal (v_{cal}^{R}) resulting in the normalized energy spectrum, V_{cal}^{R}. Therefore, the magnitude of the scattering amplitude of the fish was expressed in terms of a wavelet-based absolute target strength analogous to the Fourier-based target strength using Eqn. 5.2 as a function of angle.

2. Multi-level Decomposition

Reeder *et al*. (2004) demonstrated that the separation in time of the arrivals from the individual scattering features in the fish as it is rotated in the acoustic beam correlates to the physical separation of the anatomical features in the fish. The separation of the largest peaks of the normalized compressed pulse output (CPO) correlates with the physical separation between the skull and swimbladder of the alewife. Using the equation (Reeder *et al*., 2004)

$$separation = (timedelay) * c / (2\cos b), \tag{5.3}$$

where b is the angle of orientation relative to the transducer beam, and c is the speed of sound in water, the spatial separation between the scattering features of the fish can be determined.

At a tail-on orientation, the scattering features nearest the tail scatter the incident wave first followed by scattering from other features as the incident wave travels from tail to head. As the orientation moves towards normal incidence, the time separation between the partial waves decreases as the physical separation of the scattering features along the line of the transducers decreases. As the orientation moves away from normal incidence, the time separation increases again. Reeder *et al*. (2004) also illustrated that the temporal separation from the contributions of individual scatterers in the fish as a function of the orientation can be converted to the spatial separation along the length-wise axis of the fish.

Recall that a signal decomposed by a given discrete wavelet results in the low frequency component of the signal (approximations) and the high frequency component of the signal (details). For many signals, the low-frequency content is the most important part. By further decomposing the low frequency component, the signal will contain less noise than the original signal and will further enhance the details of the signal.

Anticipating further demonstration of the time-spatial separation correlation at each angle, the received backscattered signal (v_{bs}^{R}) was decomposed separately with two discrete wavelet transforms: the Daubechies wavelet and the Symmlet wavelet. Based on the size of received backscattered signal (8192×1) and the type of wavelet used to decompose the signal, the maximum decomposition level can be determined via a built-in function in the wavelet toolbox. For both wavelets, the maximum decomposition level for the signal, v_{bs}^{R}, is $J=9$. At this level, the signal was flattened and there were no distinct features. Therefore, the received backscattered signal (v_{bs}^{R}) was only decomposed to $J=8$ levels with both wavelets for further scattering feature analysis.

D. RESULTS

1. Scalograms

The scalograms in Fig 5.6 and 5.7 depict the wavelet power spectrum of v_{bs}^{R} for the normal incidence angle using the Morlet wavelet and the Mexican hat wavelet, respectively.

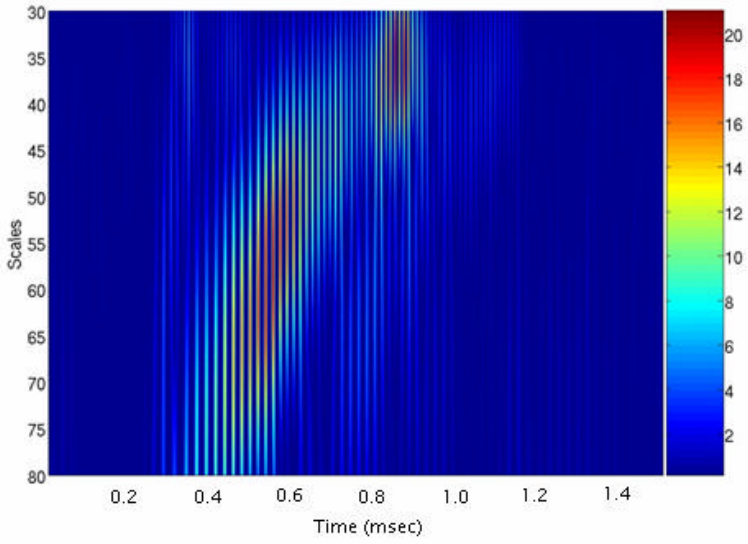

Figure 5.6: The scalogram of the received backscattered signal (v_{bs}^{R}) at the normal incidence angle using the Morlet wavelet. The colorbar (right) corresponds to the minimum and maximum coefficient amplitudes. Scales are displayed inversely (y-axis) to correspond with the frequency band, 40-95 kHz, from Reeder *et al*. (2004).

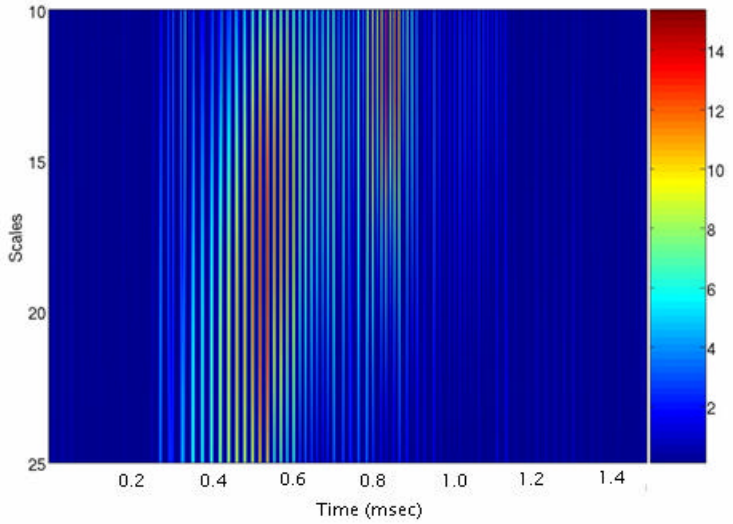

Figure 5.7: The scalogram of the received backscattered signal (v_{bs}^{R}) at the normal incidence angle using the Mexican hat wavelet. The colorbar (right) corresponds to the minimum and maximum coefficient amplitudes. Scales are displayed inversely (y-axis) to correspond with the frequency band, 40-95 kHz, from Reeder *et al*. (2004).

One difference between Fig 5.6 and 5.7 is the number of scales representing the frequency band of the received backscattered signal; Fig 5.6 ranges from 30 to 80 scales while Fig 5.7 ranges from 10 to 25 scales, both corresponding to a frequency range of 40 to 100 kHz. These frequencies in which the scales correspond to are known as *pseudo-frequencies*. The idea is to associate a purely periodic signal of frequency with the given wavelet (in this case, the Morlet and Mexican Hat). These pseudo-frequencies are determined by the relationship (The Math Works, Inc., 2004)

$$F_l = \frac{F_c}{l \cdot \Delta}, \tag{5.4}$$

where l is a scale, Δ is the sampling period, F_l is the pseudo-frequency corresponding to the scale l in Hz, and F_c is the center frequency of the given wavelet in Hz. For the Morlet wavelet, the center frequency is 0.8125 Hz; for the Mexican hat wavelet, the center frequency is 0.25 Hz. The center frequency, F_c, is the frequency which optimizes the wavelet transform of the given wavelet. Therefore, the scalograms of the received backscattered signal are plotted with the associated wavelet approximation of the signal

based on the center frequency of the given wavelet. Thus, the scalogram is considered a *center-based approximation* of the wavelet transformed signal.

Another difference of Fig 5.6 and 5.7 is the range of coefficient amplitudes in their corresponding colorbars. Fig 5.6 has coefficient amplitudes ranging from 0 to 21 while Fig 5.7 has smaller coefficient amplitudes ranging from 0 to 15. Recall from Eqn. 3.1 and 3.2 that the coefficient amplitude depends on the given wavelet; therefore, this difference in amplitude is a result of using two different wavelets on the received backscattered signal.

Finally, Fig 5.6 and 5.7 depict the received backscattered signal differently. Fig 5.6 shows a clearer depiction of the wavelet power spectrum for v_{bs}^{R} than Fig 5.7; therefore, it seems easier to approximate the scale and time of the maximum or larger coefficient amplitudes for v_{bs}^{R} with the Morlet wavelet than the Mexican hat wavelet.

Similarly, the scalograms (Fig 5.8 and 5.9) depict the wavelet power spectrum of v_{bs}^{R} for the near normal incidence angle using the Morlet wavelet and the Mexican hat wavelet, respectively.

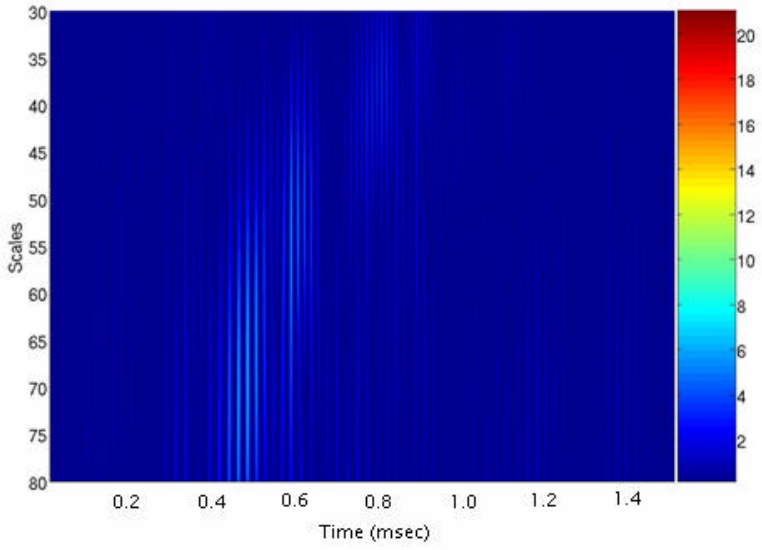

Figure 5.8: The scalogram of the received backscattered signal (v_{bs}^{R}) at the near normal incidence angle using the Morlet wavelet. The colorbar (right) corresponds to the minimum and maximum coefficient amplitudes. Scales are displayed inversely (y-axis) to correspond with the frequency band, 40-95 kHz, from Reeder *et al*. (2004).

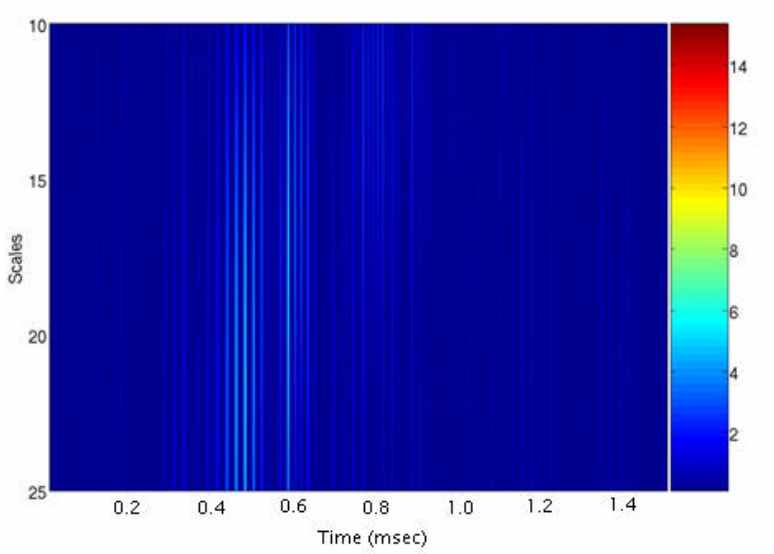

Figure 5.9: The scalogram of the received backscattered signal (v_{bs}^{R}) at the near normal incidence angle using the Mexican hat wavelet. The colorbar (right) corresponds to the minimum and maximum coefficient amplitudes. Scales are displayed inversely (y-axis) to correspond with the frequency band, 40-95 kHz, from Reeder *et al*. (2004).

The differences between Fig 5.8 and 5.9 are the same as those for the differences between Fig 5.6 and 5.7. However, the near normal incidence angle wavelet power spectrum in Fig 5.8 and 5.9 differs from the normal incidence angle wavelet power spectrum in Fig 5.6 and 5.7. The coefficient amplitudes are much less for the near normal incidence angle than the coefficient amplitudes of the normal incidence angle. This reduction in signal intensity between the scalogram for the normal and near normal incidence is consistent with the transducers moving away from the main lobe of scattering.

Similarly, the scalograms (Fig 5.10 and 5.11) depict the wavelet power spectrum of v_{bs}^{R} for the oblique incidence angle using the Morlet wavelet and the Mexican hat wavelet, respectively.

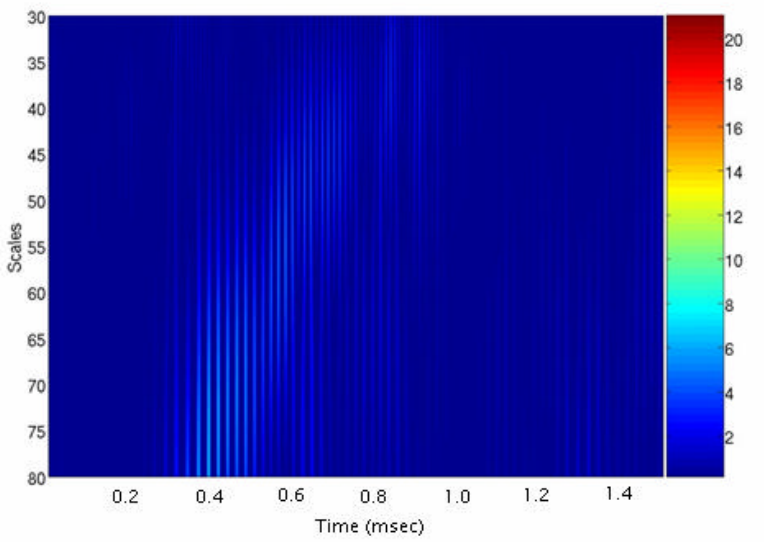

Figure 5.10: The scalogram of the received backscattered signal (v_{bs}^{R}) at the oblique incidence angle using the Morlet wavelet. The colorbar (right) corresponds to the minimum and maximum coefficient amplitudes. Scales are displayed inversely (y-axis) to correspond with the frequency band, 40-95 kHz, from Reeder *et al*. (2004).

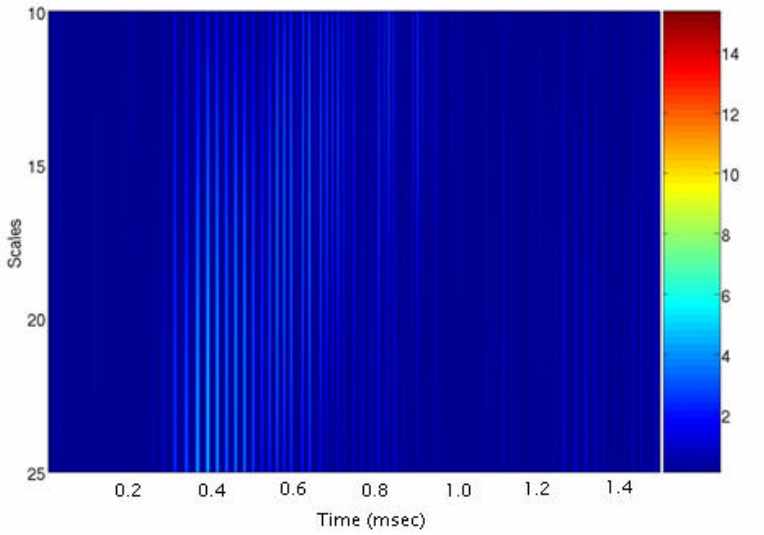

Figure 5.11: The scalogram of the received backscattered signal (v_{bs}^{R}) at the oblique incidence angle using the Mexican hat wavelet. The colorbar (right) corresponds to the minimum and maximum coefficient amplitudes. Scales are displayed inversely (y-axis) to correspond with the frequency band, 40-95 kHz, from Reeder *et al*. (2004).

The differences between Fig 5.10 and 5.11 are the same as those for the differences between Fig 5.6 and 5.7 and Fig 5.8 and 5.9, respectively. However, the oblique incidence angle wavelet power spectrum in Fig 5.10 and 5.11 slightly differs

from the near normal incidence angle wavelet power spectrum in Fig 5.8 and 5.9. Overall, the coefficient amplitudes are slightly less for the oblique incidence angle than the coefficient amplitudes of the near normal incidence angle. This reduction in signal intensity between the scalogram for the near normal and oblique incidence is consistent with the transducers moving even further away from the main lobe of scattering.

2. Absolute Target Strength

The absolute target strength of the received backscattered signal (v_{bs}^{R}) at normal, near normal, and oblique angles of incidence as determined by applying the Morlet wavelet and the Mexican hat wavelet are shown in Fig 5.12 – 5.17. Overall, these figures demonstrate a high degree of variability in absolute target strength over all scales.

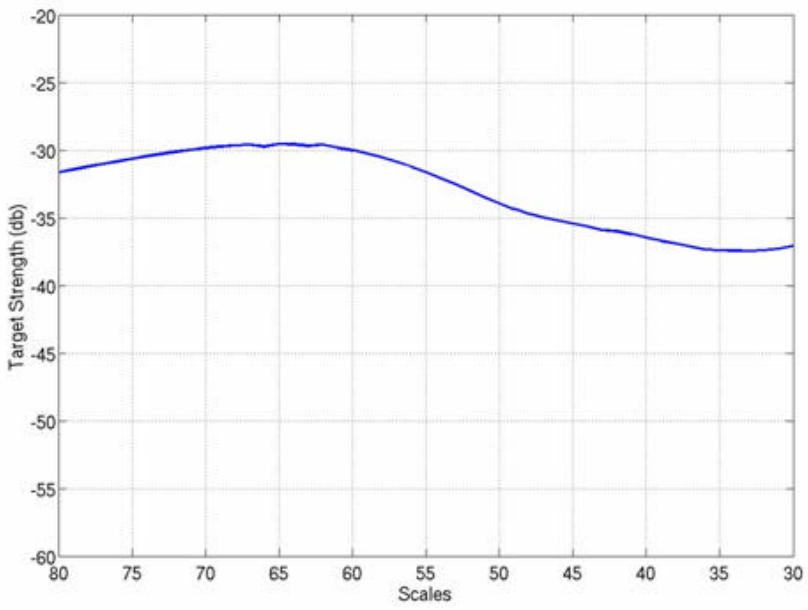

Figure 5.12: Target strength of v_{bs}^{R} at normal incidence as a function of scales using the Morlet wavelet. Scales are displayed inversely (x-axis) to correspond with the frequency band, 40-95 kHz, from Reeder *et al*. (2004).

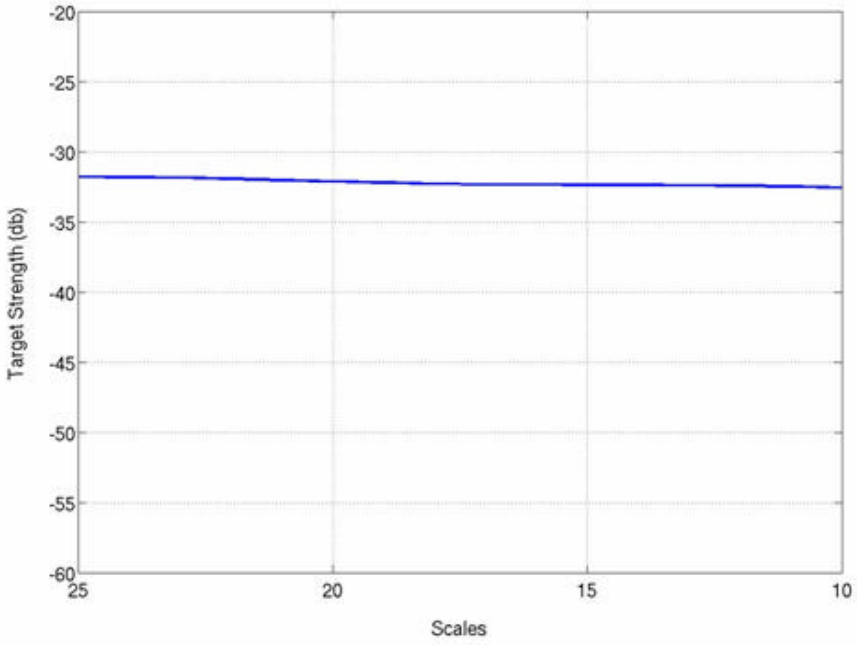

Figure 5.13: Target strength of v_{bs}^{R} at normal incidence as a function of scales using the Mexican hat wavelet. Scales are displayed inversely (x-axis) to correspond with the frequency band, 40-95 kHz, from Reeder *et al*. (2004).

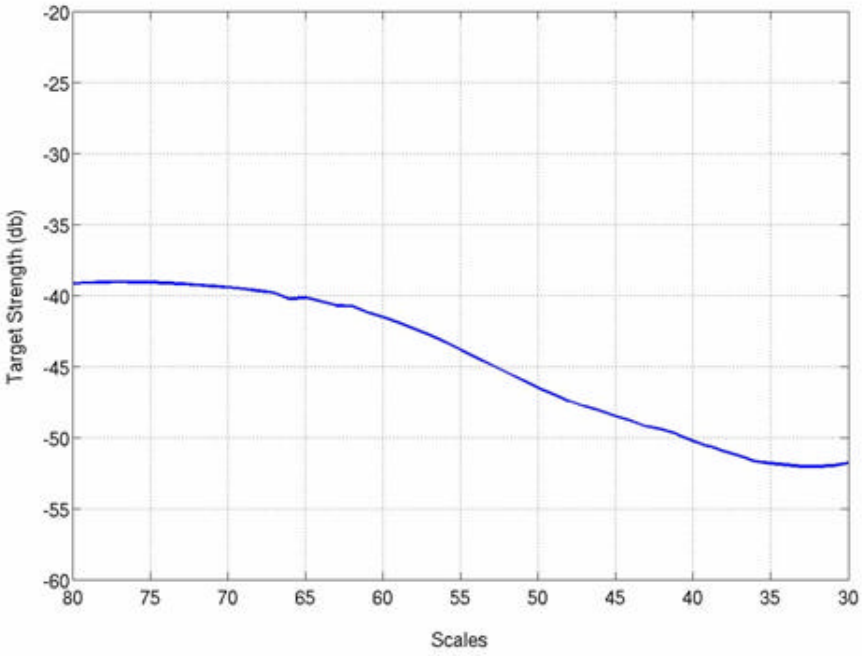

Figure 5.14: Target strength of v_{bs}^{R} at near normal incidence as a function of scales using the Morlet wavelet. Scales are displayed inversely (x-axis) to correspond with the frequency band, 40-95 kHz, from Reeder *et al*. (2004).

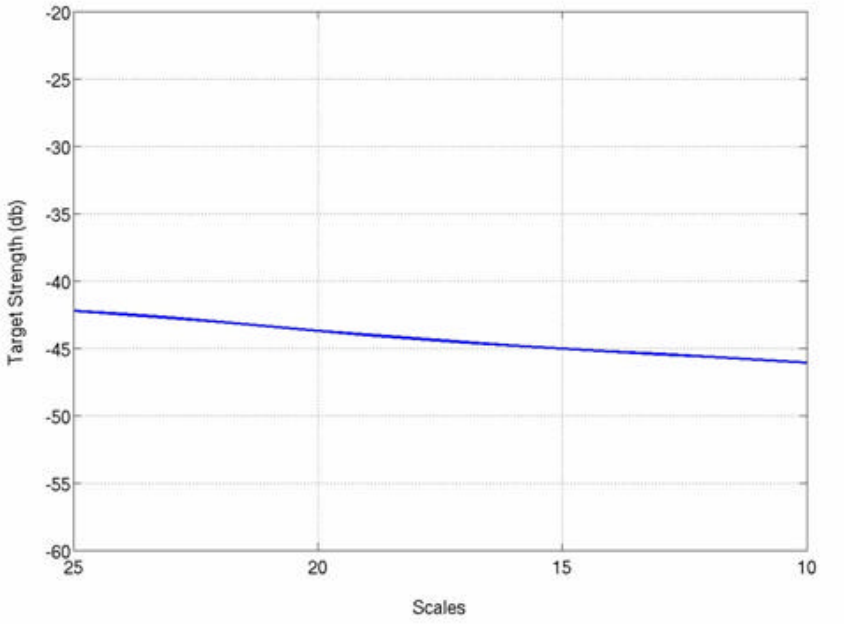

Figure 5.15: Target strength of v_{bs}^{R} at near normal incidence as a function of scales using the Mexican hat wavelet. Scales are displayed inversely (x-axis) to correspond with the frequency band, 40-95 kHz, from Reeder *et al*. (2004).

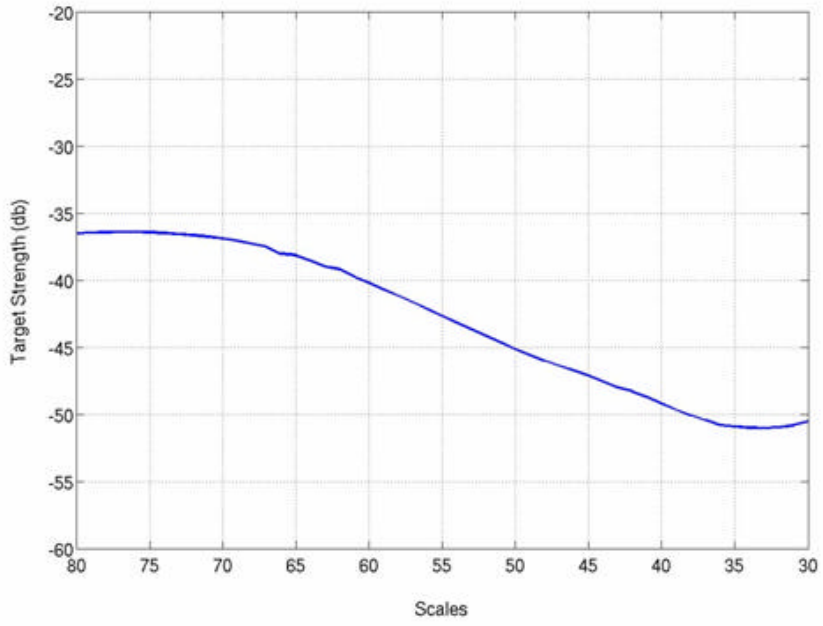

Figure 5.16: Target strength of v_{bs}^{R} at oblique incidence as a function of scales using the Morlet wavelet. Scales are displayed inversely (x-axis) to correspond with the frequency band, 40-95 kHz, from Reeder *et al*. (2004).

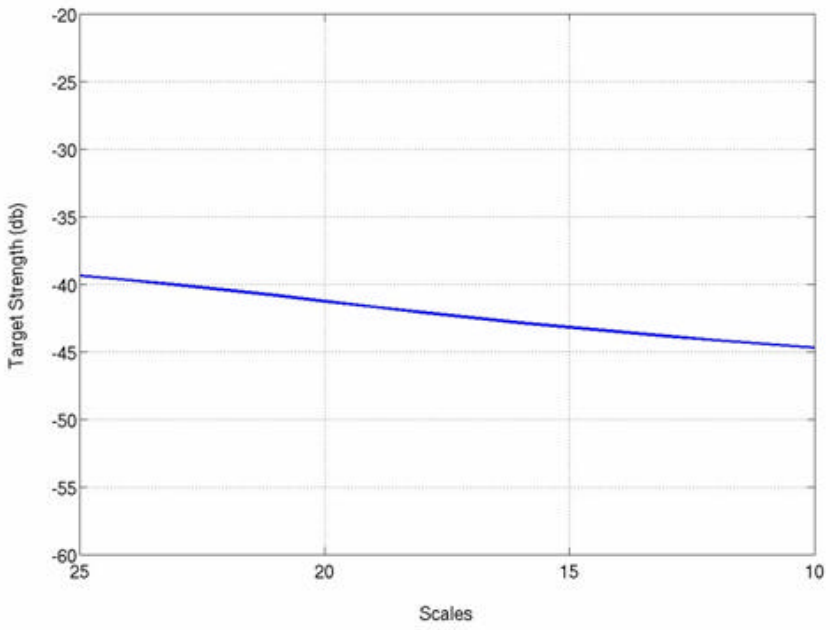

Figure 5.17: Target strength of v_{bs}^{R} at oblique incidence as a function of scales using the Mexican hat wavelet. Scales are displayed inversely (x-axis) to correspond with the frequency band, 40-95 kHz, from Reeder *et al*. (2004).

Comparing Fig 5.12 to Fig 5.4 (top right) for the normal incidence orientation, the range of target strengths over all scales (between -28 and -38 db) is very similar in shape and close in value to the range of target strengths (between -25 and -35 db) of the PWTS over all frequencies. Similarly, Fig 5.13 shows the range of target strengths over all scales (between -38 and -44 db) somewhat close to the PWTS target strengths, but instead linearly shaped. Also, Fig 5.12 and Fig 5.13 fall within the range of target strengths computed for the whole time series (thin lines, Fig 5.4 top right), but are not similar in shape.

Comparing Fig 5.14 to Fig 5.4 (thick lines, middle right) for the near normal incidence orientation, the range of target strengths over all scales (between -38 and -52 db) is also somewhat similar in shape and close in value to the range of target strengths (between -30 and -40 db) of the PWTS over all frequencies. From scale 80 to 65 which is approximately equivalent to frequencies ranging from 40 to 50 kHz, the target strength is within the range of -30 to -40 db of the PWTS. Beyond scale 65, the target strength falls out of the PWTS range. Fig 5.15 shows that the range of target strengths (from -42

to -46) over all scales falls just outside the PWTS range. Similar to Fig 5.13, the range of target strengths over all scales is linearly shaped. Also, Fig 5.14 and Fig 5.15 fall within the range of target strengths computed for the whole time series (thin lines, Fig 5.4 middle right), but are not similar in shape.

Comparing 5.16 to Fig 5.4 (bottom right) for the oblique incidence orientation, the range of target strengths over all scales (between -37 and -52 db) falls within the range of target strengths (between -35 and -70 db) of the PWTS over all frequencies, but is not similar in shape. Similarly, Fig 5.17 shows that the range of target strengths over all scales falls within the range of the PWTS target strengths, but is linearly shaped. Also, Fig 5.16 and Fig 5.17 fall within the range of target strengths computed for the whole time series (thin lines, Fig 5.4 bottom right), but are not similar in shape.

Additionally, Fig 5.16 looks similar in shape although reversed to the first peak of the PWTS for the oblique angle (Fig 5.5 middle right). The range of target strengths in Fig 5.16 is very close to and falls within the range of target strengths for the first peak of the PWTS. The same also holds true for the second peak of the PWTS (Fig 5.5 bottom right).

3. Multi-level Decomposition

Fig 5.18 - 5.23 shows the received backscattered signal v_{bs}^{R} decomposed at $J = 8$ levels at normal, near normal, and oblique angles of incidence by the Daubechies and Symmlet wavelets.

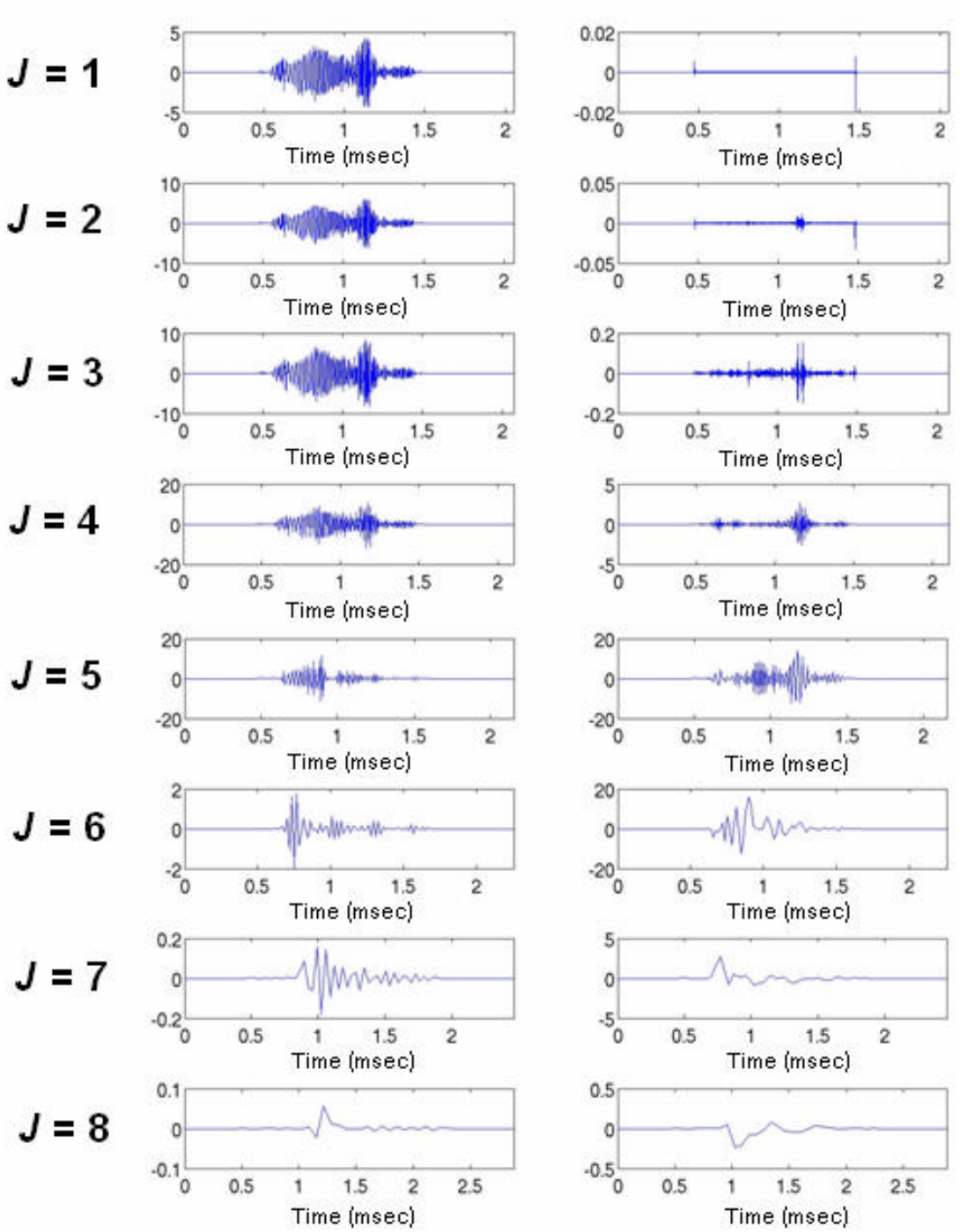

Figure 5.18: Multi-level decomposition for $J = 8$ levels of the received backscattered signal, v_{bs}^{R}, at normal incidence using the Daubechies wavelet. The plots on the left are the low frequency content of the signal while the plots on the right are the high frequency content.

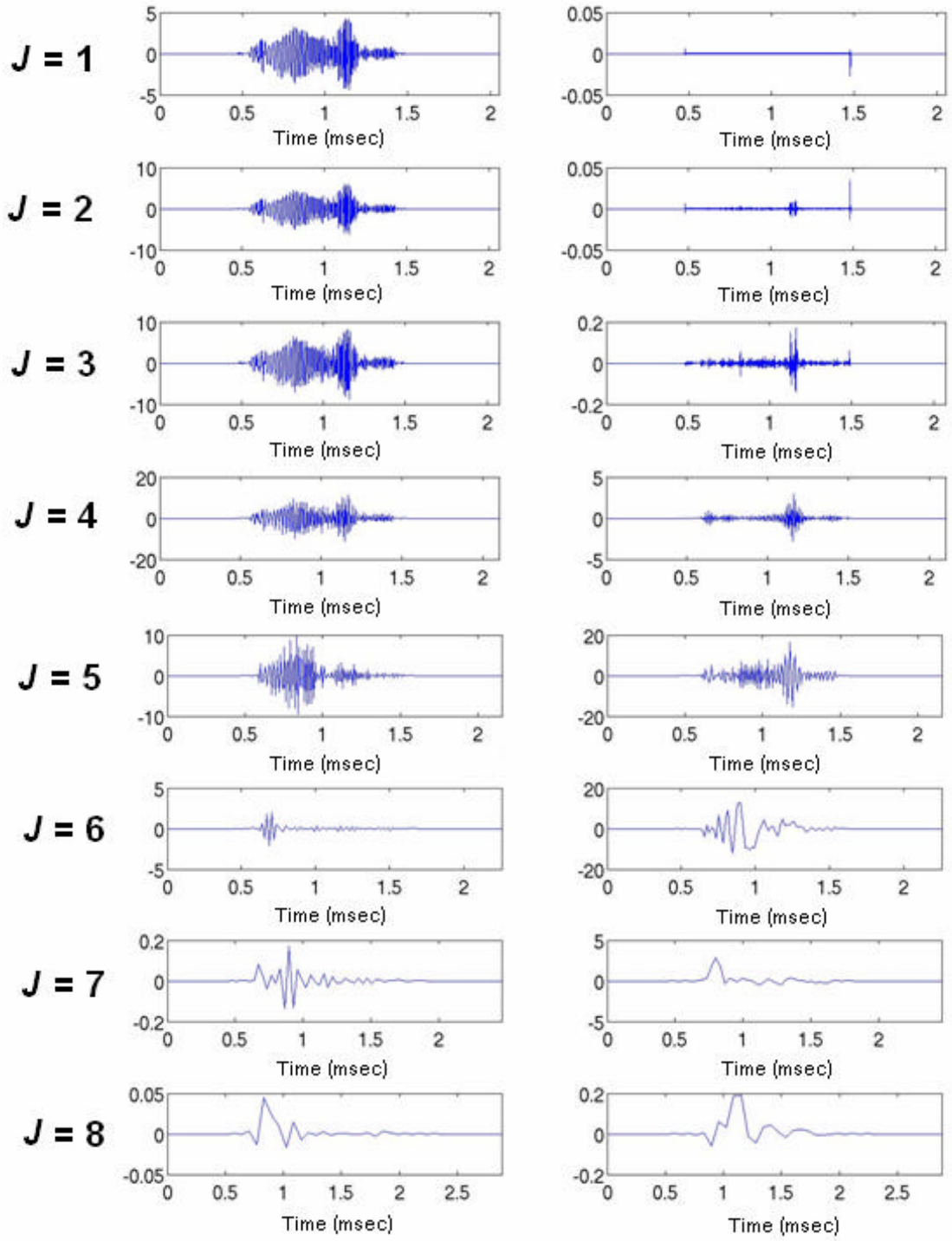

Figure 5.19: Multi-level decomposition for $J = 8$ levels of the received backscattered signal, v_{bs}^{R}, at normal incidence using the Symmlet wavelet. The plots on the left are the low frequency content of the signal while the plots on the right are the high frequency content.

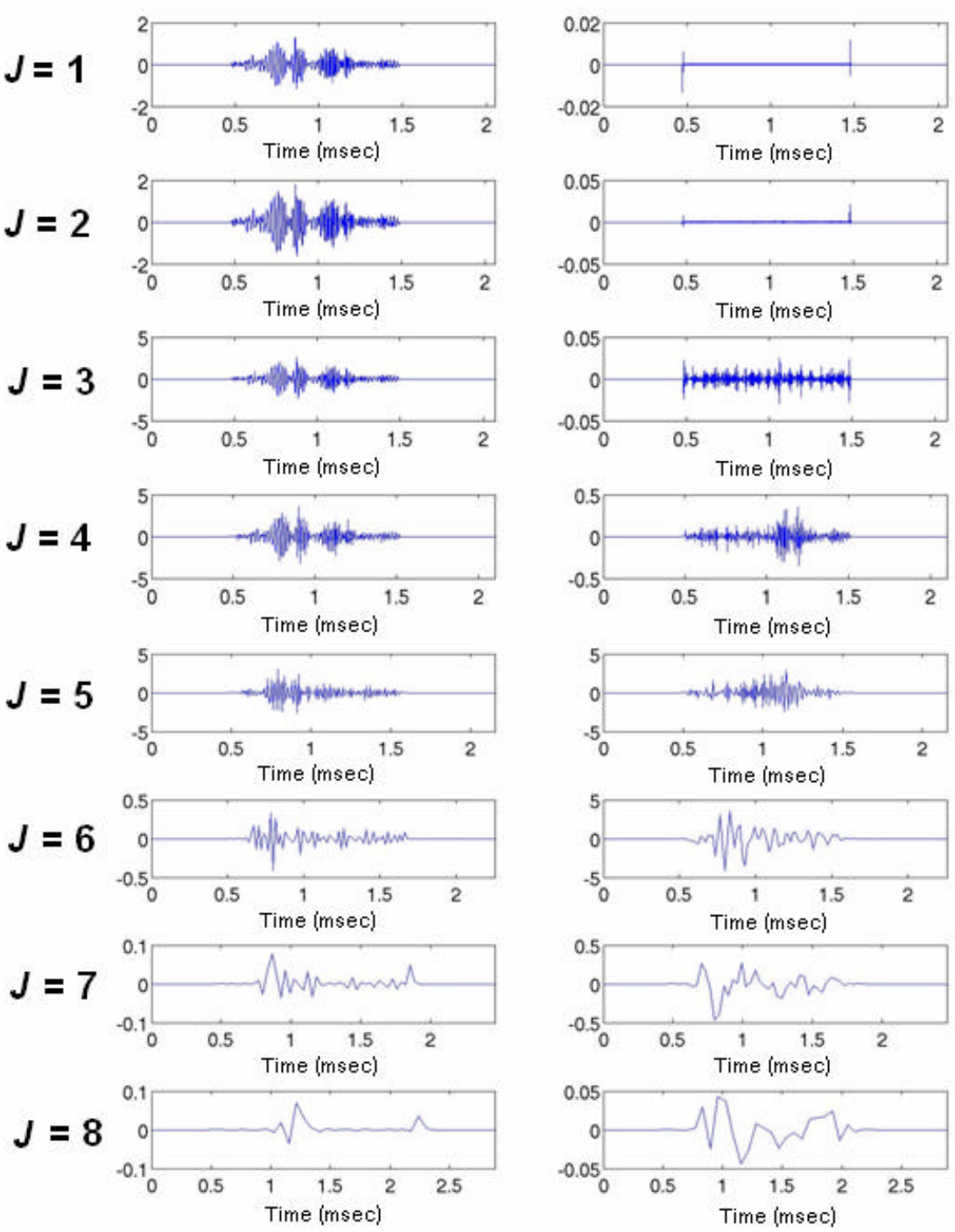

Figure 5.20: Multi-level decomposition for $J = 8$ levels of the received backscattered signal, v_{bs}^{R}, at near normal incidence using the Daubechies wavelet. The plots on the left are the low frequency content of the signal while the plots on the right are the high frequency content.

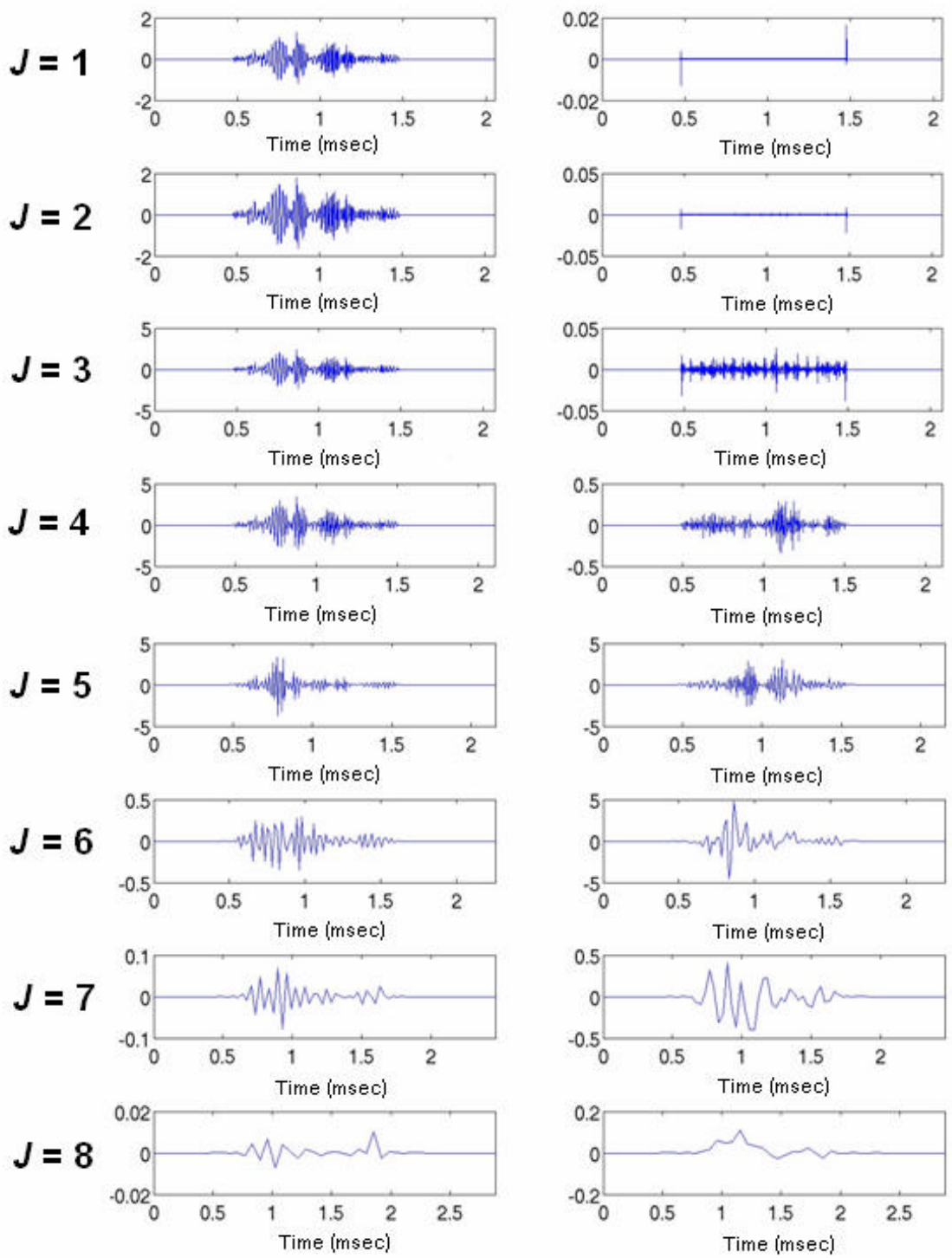

Figure 5.21: Multi-level decomposition for $J = 8$ levels of the received backscattered signal, v_{bs}^{R}, at near normal incidence using the Symmlet wavelet. The plots on the left are the low frequency content of the signal while the plots on the right are the high frequency content.

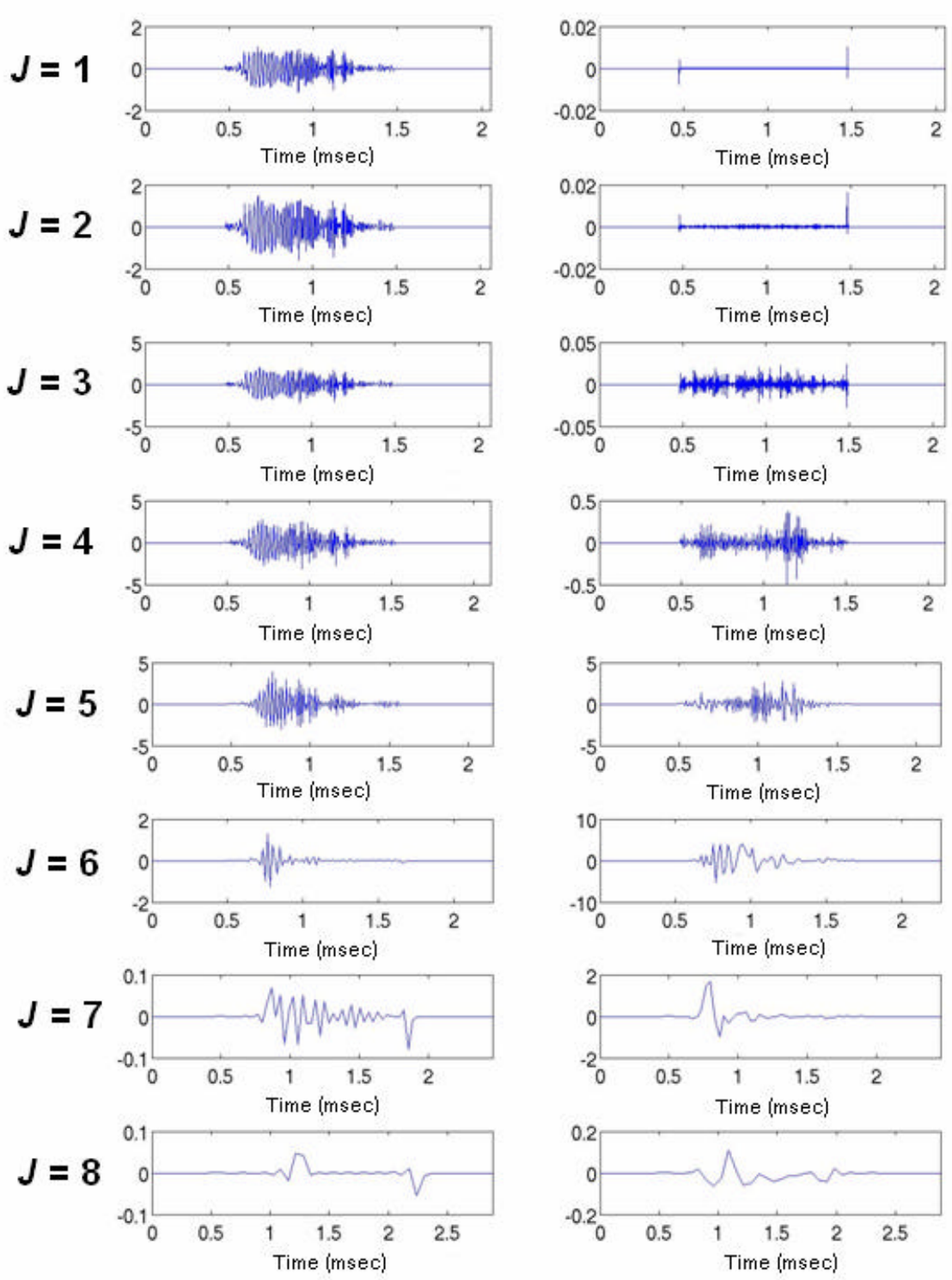

Figure 5.22: Multi-level decomposition for $J = 8$ levels of the received backscattered signal, v_{bs}^{R}, at oblique incidence using the Daubechies wavelet. The plots on the left are the low frequency content of the signal while the plots on the right are the high frequency content.

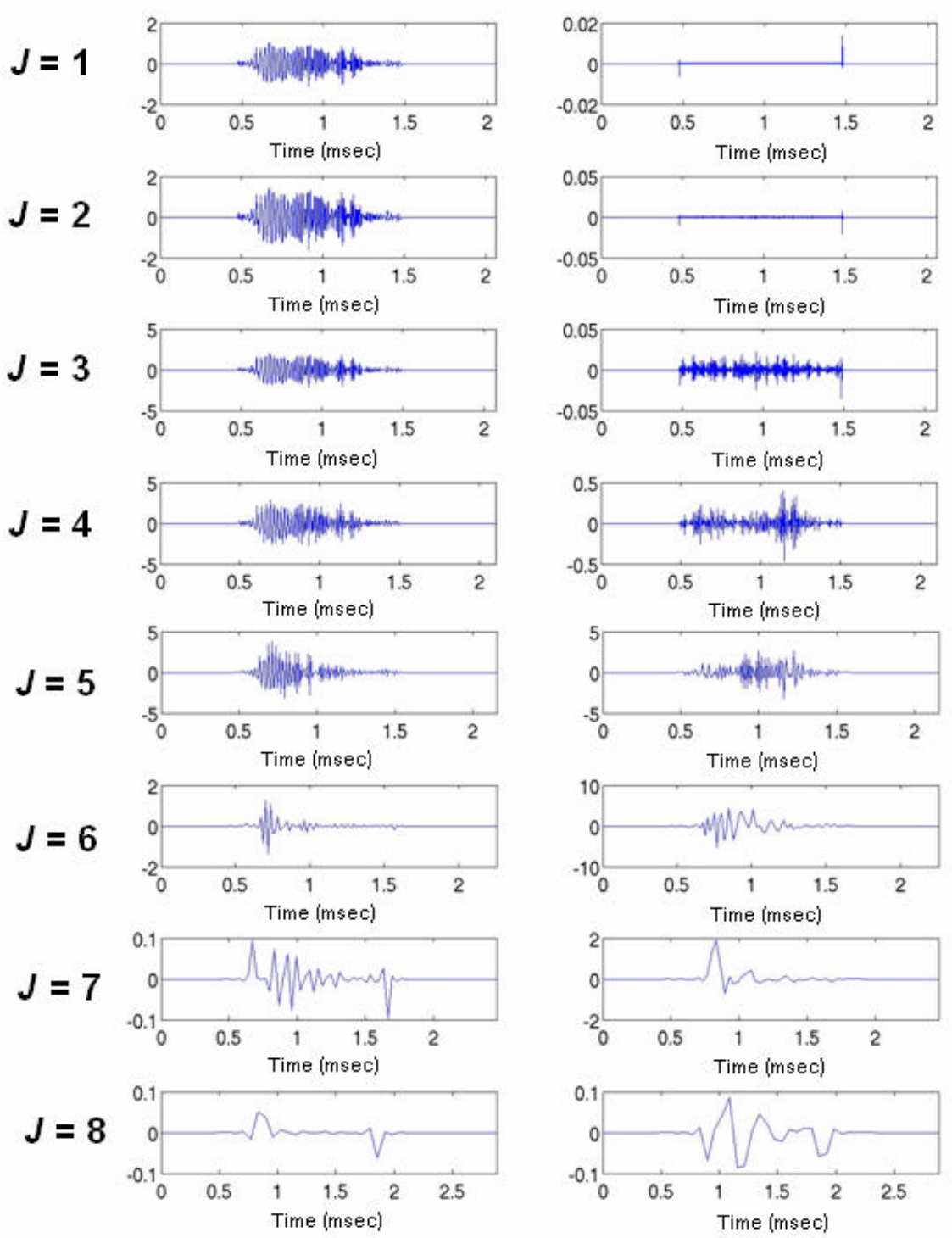

Figure 5.23: Multi-level decomposition for $J = 8$ levels of the received backscattered signal, v_{bs}^{R}, at oblique incidence using the Symmlet wavelet. The plots on the left are the low frequency content of the signal while the plots on the right are the high frequency content.

At levels $J = 1$ and $J = 2$ in all figures (right) and at level $J = 3$ in Fig 5.20-5.23 (right), the two spikes at 0.8 msec and 1.48 msec appear and are associated with the beginning and end positions of the zero padding for the signal. In Fig 5.18 (right) for the normal incidence orientation, at level $J = 2$ two small peaks appear approximately at 1.13 msec and 1.16 msec with amplitudes less than +/- 0.05. At level $J = 3$, the peaks become more distinct at the same places in time with amplitudes close to +/- 0.2. From Eqn. 5.3, with $c = 1500\, m/s$, $b = 0°$, and a time delay of 0.03 msec, the spatial separation is approximately equal to 2.25 cm. As the signal is further decomposed, the peaks are no longer distinct.

Similarly, in Fig 5.19 (right), two small peaks appear at approximately at 1.12 msec and 1.16 msec with amplitudes less than +/- 0.05 at level $J = 2$. The peaks also become more distinct at $J = 3$ at the same places in time with similar amplitudes. From Eqn. 5.3, with $c = 1500\, m/s$, $b = 0°$, and a time delay of 0.04 msec, the spatial separation is approximately equal to 3 cm. As the signal is further decomposed, the peaks are no longer distinct.

In Fig 5.20 (right) for the near normal incidence orientation, level $J = 3$ shows its largest peak at approximately 1.1 msec and its next largest peak at 1.2 msec, although both peaks are really not substantial compared to the rest of the signal. However, level $J = 4$ resolves these peaks much better, showing them more distinctly at 1.12 msec and 1.19 msec with amplitudes close to +/- 0.3. From Eqn. 5.3, with $c = 1500\, m/s$, $b = 10°$, and a time delay of 0.07 msec, the spatial separation is approximately equal to 5.33 cm. As the signal is further decomposed, the peaks are no longer distinct.

In Fig 5.21 (right) for the near normal incidence orientation, level $J = 3$ is very similar to that same level in Fig 5.20. The largest peak is around 1.1 msec and its next largest peak is close to 1.25 msec, although the peaks are not substantial compared to the rest of the signal. Level $J = 4$ resolves these peaks much better, revealing them more specifically at 1.1 msec and 1.2 msec with similar amplitudes close to +/- 0.3. From Eqn. 5.3, with $c = 1500\, m/s$, $b = 10°$, and a time delay of 0.09 msec, the spatial distance is

approximately equal to 6.85 cm. As the signal is further decomposed, the peaks are no longer distinct.

In Fig 5.22 (right), there are no distinct peaks at level $J = 3$. However, at level $J = 4$, two distinct peaks appear at approximately 1.14 msec and 1.2 msec with amplitudes between 0.3 and 0.4. From Eqn. 5.3, with $c = 1500\, m/s$, $b = 30°$, and a time delay of 0.06 msec, the spatial distance is approximately equal to 5.2 cm. As the signal is further decomposed, the peaks are no longer distinct.

Similar to Fig 5.22, there are no distinct peaks at level $J = 3$ in Fig 5.23 (right), but there are two distinct peaks at approximately 1.14 msec and 1.22 msec with amplitudes between 0.3 and 0.4. From Eqn. 5.3, with $c = 1500\, m/s$, $b = 30°$, and a time delay of 0.08 msec, the spatial distance is approximately equal to 6.9 cm. As the signal is further decomposed in Fig 5.23, the peaks are no longer distinct.

E. DISCUSSION

1. Scalograms

The depictions of the received backscattered signal, v_{bs}^{R}, at the normal, near normal, and oblique incidence angles in Fig 5.6-5.11, respectively, show the relative intensity as a function of frequency and time. The scalograms associated with the Morlet wavelet have better resolution. This makes it relatively difficult to determine an exact scale and time location of the larger coefficient amplitudes. Ideally, the preference is a more refined scalogram where the larger coefficient amplitudes are not all meshed together into one relatively large area of the scalogram. As previously mentioned, these scalograms are center-based approximations of the wavelet transformed signal and give a relative approximation of the signal intensity based on the angle of incidence.

Due to the complexity of these scattered signals, it is recognized that using only the built-in functions for the continuous wavelet transforms in MATLAB limits the feature extraction capability. While these scalograms give a prudent first order approximation, the respective wavelets do not have a center frequency that optimizes the features of the received backscattered signal, v_{bs}^{R}. A wavelet that better represents the

frequency spectrum of the scattered signal may enhance and reveal the prominent features of v_{bs}^{R} at varying angles of incidence.

2. Absolute Target Strength

Although the target strengths of the received backscattered signal, v_{bs}^{R}, over all scales at the normal, near normal, and oblique incidence angles in Fig 5.12-5.17, respectively, were within the range of target strengths over the frequency band from Reeder *et al*. (2004), the shapes of the plots did not reveal the constructive and destructive interferences between the multiple arrivals as the angle moved away from normal incidence. Similar to the issues with the scalogram, the center frequencies of the Morlet and Mexican hat wavelets do not seem to optimize or enhance the features of v_{bs}^{R} in terms of overall target strength by depicting a series of peaks and nulls as the angle moved away from normal incidence.

Recall from Fig 5.5 that the two largest peaks of the received backscattered signal were separated in time and the target strength was calculated for each peak, commonly referred to as the partial wave target strength (PWTS). Overall, the target strengths as determined by the Morlet wavelet are shapelier and are somewhat closer to resembling the PWTS found in Reeder *et al*. (2004). Since the Mexican hat wavelet is a simpler wavelet, it is expected that the absolute target strength results are a flat spectrum (Figs 5.13, 5.15, and 5.17).

More specifically, the results at oblique incidence as determined by the Morlet wavelet even closer resemble the PWTS found in Reeder *et al*. (2004). Apart from the others, these results are very encouraging. If the windowing effects of the Morlet wavelet are capable of capturing the PWTS, then wavelets could have substantial operational significance on acoustically scattered signals. The time it took to compute the PWTS using match filtering from Reeder *et al*. (2004) was on the order of hours compared to the time it took to compute the PWTS using wavelets which was on the order of minutes. Overall, this reduction in computational time could effectively alter the method for calculating the PWTS.

However, the inability of the Morlet and Mexican hat wavelets to enhance and reveal the multiple arrivals of the received backscattered signal suggest that these are not

the optimal wavelets to use for this type of signal. The fact that the range of target strengths over all scales were within the range of target strengths over the frequency band from Reeder *et al*. (2004) is very encouraging. To the best of my knowledge and research efforts, this is the first attempt at using wavelets to calculate absolute target strength for acoustic signals. Although a more extensive study is required in finding the wavelet that can handle this type of signal complexity to further extract multiple arrivals, this a good attempt at a first order approximation in determining absolute target strength.

In attempt to verify that the methodology used in this study is correct, the same process was done using the Morlet wavelet for the real part of a standard Gaussian function over time given by

$$p(t) = \cos(w_c t)\, e^{-s^2 t^2/2}, \tag{5.4}$$

where w_c is the center radial frequency and s is the standard deviation. In general, $w_c = 2p\, f_c$, where f_c is the center frequency of a given signal; in this example, $f_c = 60\,\text{kHz}$ and $s = 10\,\text{kHz}$, and the time ranges from $-17\ m\sec < t < 17\ m\sec$ (Fig 5.24).

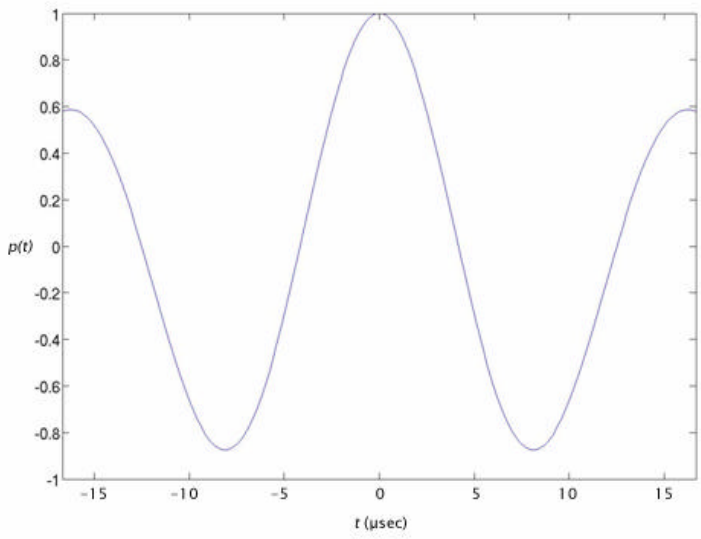

Figure 5.24: Depiction of the standard Gaussian function in Eqn. 5.4.

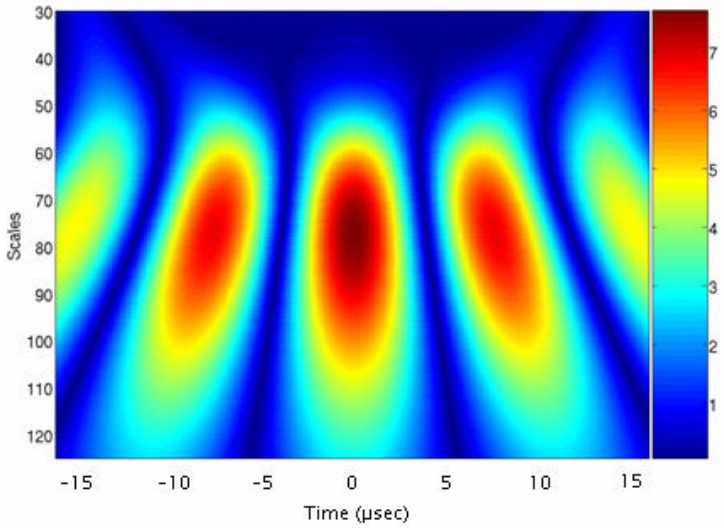

Figure 5.25: Scalogram of the standard Gaussian function in Eqn. 5.4.

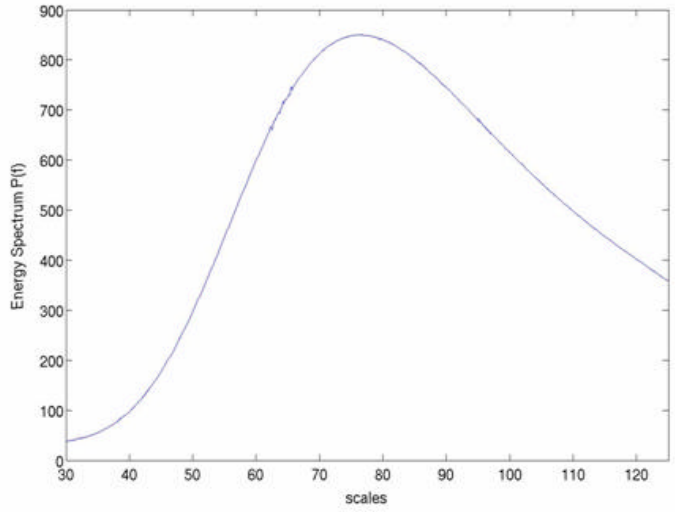

Figure 5.26: Wavelet spectrum $P(f)$ of the standard Gaussian function in Eqn. 5.4.

Recall from chapter III that a Morlet wavelet is constructed by modulating a sinusoidal function by a Gaussian function; therefore, applying a Morlet wavelet to Eqn. 5.4 will clearly bringing out the maximum and larger coefficient amplitudes associated with the features of the original function (Fig 5.25). In addition, the wavelet spectrum clearly determines the exact scale (or pseudo-frequency) of the maximum signal energy (Fig 5.26). In this example, the maximum signal energy is located at scale 76, or 16 kHz.

Therefore, this example shows that the methodology is correct; however, due to the complexity of the received backscattered signal in this study, the Morlet and Mexican

hat wavelets clearly are not the optimal wavelets to depict multiple arrivals from the scattered signal as the angle of orientation moves away from normal incidence.

3. Multi-level Decomposition

Reeder *et al*. (2004) showed that the separation of the largest peaks of the normalized compressed pulse output (CPO) correlates with a physical separation between the skull and swimbladder of the alewife of approximately 10 cm (Fig 5.27).

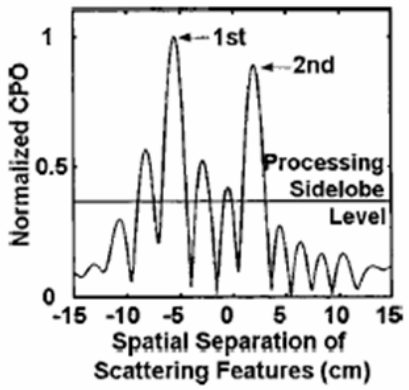

Figure 5.27: Depiction of the two largest peaks of the normalized compressed pulse output (CPO) as correlated to the spatial separation of the skull and swimbladder of the alewife used in the experiment (From Reeder *et a*l., 2004).

For the signals decomposed in Figs 5.18-5.23, the spatial separations as determined from the time delay of the two largest peaks in each figure are not equal to the spatial separation of 10 cm as found in Reeder *et al*. (2004). The closest value to that found in Reeder *et al*. (2004) was at the oblique angle using the Symmlet wavelet, a spatial separation equal to 6.9 cm. In fact, comparing all the angles based on which wavelet decomposed the signal, the Symmlet wavelet decomposed the signal to reveal a time delay that correlated closer to the spatial separation as found in Reeder *et al*. (2004). Also, the spatial separation of the decomposed signal at the near normal and oblique angles of incidence are very close in proximity compared to the decomposed signal at normal incidence.

The difference between the spatial separation found in Reeder *et al*. (2004) and the spatial separation found from the wavelet decomposed signal may be a combination of numerous factors. The variability in these results is partly a function of the fish moving during the experiment and the signal complexity. At near normal and oblique

incidence, the spatial separation ranging between 5-7 cm are very promising results. The 10 cm spatial separation from Reeder *et al*. (2004) was based on the acoustic center of the swimbladder. Therefore, by accouting for the variability as mentioned above, these results are acceptable.

Another important factor is in relation to the wavelets used to decompose these signals. Although the nearly symmetric Symmlet wavelet resolved the time delay of the high frequency peaks better to correlate closer to the spatial separation between the skull and the swimbladder, the Daubechies and the Symmlet wavelets have difficulty capturing the multiple arrivals of the high frequency content of the signal. Therefore, it is recommended that other wavelets are considered for this multi-level decomposition process.

F. FUTURE RESEARCH

Meyers *et al*. (1993) mentions that the appropriate choice of $\Psi(t)$ is dictated by the goals of the analysis. Similarly, if one knows the characteristics of the signal or pattern being sought, the wavelet should be chosen to have the same pattern. While choosing wavelets within the wavelet toolbox in MATLAB were considered appropriate for the two main parts of this study, the outcome was not exactly analogous to the Fourier method as demonstrated in Reeder *et al*. (2004).

Meyers *et al*. (1993) describes a mother wavelet that would be more applicable to the type of signal analyzed in this study. Meyers *et al* (2003) mentions that if one is seeking the short segments of linearly increasing frequency (or "chirps") like the signal in this study, an appropriate mother wavelet would be (Meyers *et al*., 2003, Eqn. 4)

$$\Psi(t) = e^{ikt^2/2} e^{ict} e^{-t^2/2}. \tag{5.5}$$

Due to the limitations of the built-in functions in MATLAB on this signal type, further research is needed to design a wavelet algorithm that is synonymous with the mother wavelet in Eqn. 5.5. If such an algorithm is generated, it is possible that a wavelet analogous method for determining scattering features in fish will exist. As a result of this development, acoustic scattering models such as the Kirchhoff-ray mode

(KRM) model and the newly developed Fourier matching method (FMM) could be further enhanced as well as creating a separate wavelet model for acoustic scattering.

THIS PAGE INTENTIONALLY LEFT BLANK

VI. MARINE MAMMAL STUDY

In the last decade, the U.S. Navy has been recognized and criticized for its potentially harmful impact on the environment using high frequency (HF) active sonars during anti-submarine warfare (ASW) operations. Active sonar releases energy into the ocean, and there is evidence to suggest that this may have an adverse effect on both the physiology and behavioral patterns of marine mammals. Although the precise scientific effects are not entirely clear, the Department of Defense (DOD) has developed a policy that any activity which may have a potentially harmful impact on the environment requires mitigating measures to reduce any adverse effects. The DOD is committed to taking all reasonable and practical measures to protect the environment and has since developed a precautionary principle to mitigate against undue effects on the marine environment.

Similar to the Royal Navy's policy on avoiding marine mammal disturbances while using active sonar, the U.S. Navy developed a guiding principle for their use of active sonar which is defined in a simple process: (1) Plan, (2) Look, (3) Listen, and (4) Act. This process underlines awareness which underpins the principle of environmental compliance.

By developing an awareness of emerging responsibilities for marine mammals and the actions necessary to minimize potentially damaging effects, the U.S. Navy in conjunction with other government agencies has devoted their research efforts to developing methods to avoid marine sensitive areas. Therefore, when U.S. Navy assets are planning active sonar operations, any clear evidence of mammal activity in close proximity will be available. All ships, submarines, and aircrafts can essentially avoid those areas and can minimize any potentially damaging environmental effects.

The remainder of this chapter will discuss the acoustic monitoring of several *Odontocetes* with bottom-mounted hydrophones on the Southern California ASW Range (SOAR) off the coast of San Clemente Island. The first section will describe the SOAR range, the locations of each hydrophone used to passively monitor the mammals, and the six different vocalizations used in this study; the second section will discuss the

methodology in determining the approximate position of each mammal and the multi-level decomposition of the received signals with the Haar wavelet; the third section will present and discuss the results of the multi-level decomposition of each signal and its correlation to the mammal's position relative to each hydrophone; and the final section will provide recommendations for further research.

A. BACKGROUND

Since the early 1930s, San Clemente Island (SCI) has been owned and operated by various naval commands. Currently, the Commander-in-Chief, Naval Forces, Pacific (CINCPACFLT) is the major claimant for the island, and the Naval Air Station, North Island (NASNI) is responsible for its administration.

Over a dozen range and operational areas are clustered within a 60-mile radius of the island. San Clemente Island is the southernmost of the eight California channel islands which lies 55 nautical miles south of Long Beach and 68 nm west of San Diego (Fig 6.1). The island is approximately 21 miles long and is 4-1/2 miles across at its widest point, with its highest elevation of 1,964 feet located at Mount Thirst.

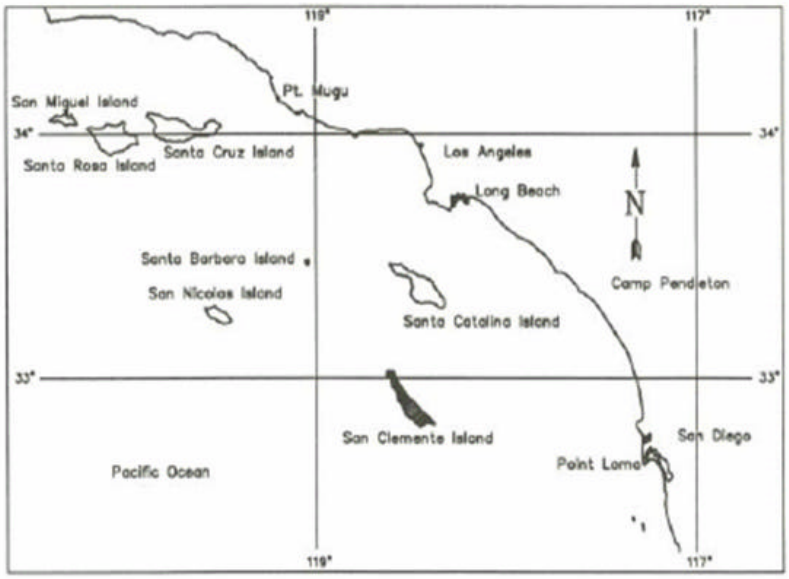

Figure 6.1: Geographic location of San Clemente Island (From Sturgeon, 2002).

The San Clemente Island Range Complex (SCIRC) is the cornerstone of the tactical training ranges supporting the Southern California Operations Area (SOCAL).

SOCAL supports the largest concentration of naval forces in the world. The land, air, and sea ranges around San Clemente Island provide the U.S. Navy, U.S. Marine Corps, and other military services, space and facilities which they use to conduct readiness training and test and evaluation activities. The distance of San Clemente Island from the mainland and its complete Navy ownership make the island and its surrounding area ideal for fleet training, weapon and electronics system testing, and research and development activities.

The Southern California Offshore Range (SCORE) is a state-of-the-art, multi-warfare, integrated training facility which provides tactical range training and testing services to U.S. Navy units of the Pacific Fleet. With its forward deployed forces and rapid reaction capabilities, the U.S. Navy is at the forefront of that defense. Consequently, a high level of operational readiness by fleet forces is essential to maintain peace in the international arena. Since fleet readiness is a direct function of quality training, SCORE was established and designed to provide Fleet operators with this essential training.

Under the command of the Fleet Area Control and Surveillance Facility, San Diego (FACSFACSD), SCORE conducts a multitude of operations including multi-warfare and battle group evolutions, on and around San Clemente Island (SCI). SCORE consists of several sub-range components: the Southern California Anti-Submarine Warfare Range (SOAR), the Electronic Warfare Range (EWR) which includes the Range Electronic Warfare Simulator (REWS) and a variety of multi-axis emitters and jammers, two MINEX Training Ranges (MTR), a training minefield (Kingfisher) and the Shore Bombardment Area (SHOBA).

The Southern California Anti-Submarine Warfare Range (SOAR) conducts anti-submarine warfare (ASW) training by utilizing a mix of air/surface tracking systems and underwater tracking with highly sophisticated hydrophone arrays. The ASW range is comprised of seven sub-areas and encompasses approximately 670 square miles of 3-D underwater tracking area, located 68 nautical miles off the coast of San Diego. The range routinely supports air, surface, and subsurface unit level torpedo firing exercises as well

as inner and middle zone battle group training, supporting the vast majority of Pacific Fleet Undersea Warfare (USW) training exercises.

B. METHODOLOGY

In this study, the hydrophones on the SOAR were used to monitor several marine mammal vocalizations (Fig 6.2, highlighted area). In August 2004, six different vocalizations were received on four separate hydrophones: H70 (32.806° N, -118.643° E), H71 (32.785° N, -118.681° E), H77 (32.789° N, -118.609° E), and H78 (32.767° N, -118.639° E) (Fig 6.3).

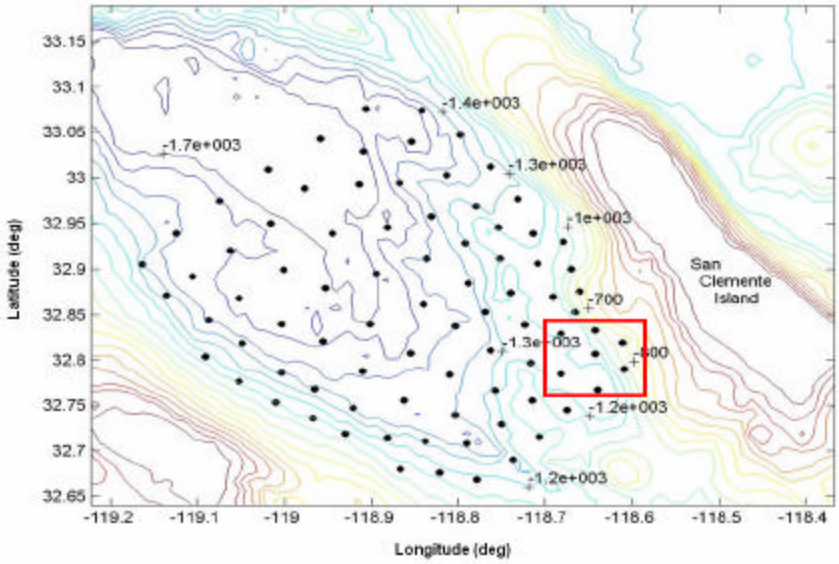

Figure 6.2: Location of hydrophones on the SOAR relative to SCI.

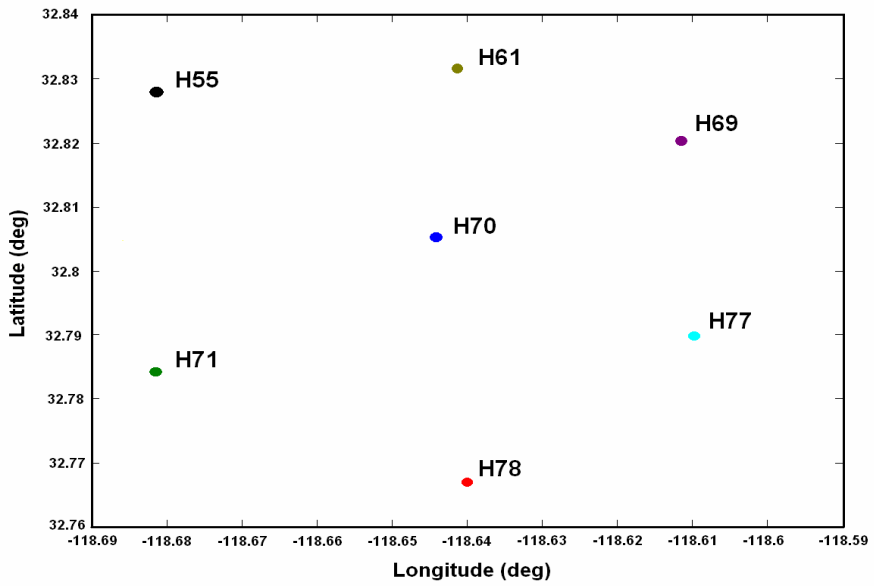

Figure 6.3: Close-up of the numbered hydrophones on the SOAR.

The vocalizations are single channel clips of raw hydrophone data recorded at a frequency of 80 kHz. Each vocalization was process through a Butter filter, a fourth order bandpass filter with a frequency band of 5 kHz to 30 Khz. Each vocalization was then displayed in a spectrogram (Fig 6.4-6.9).

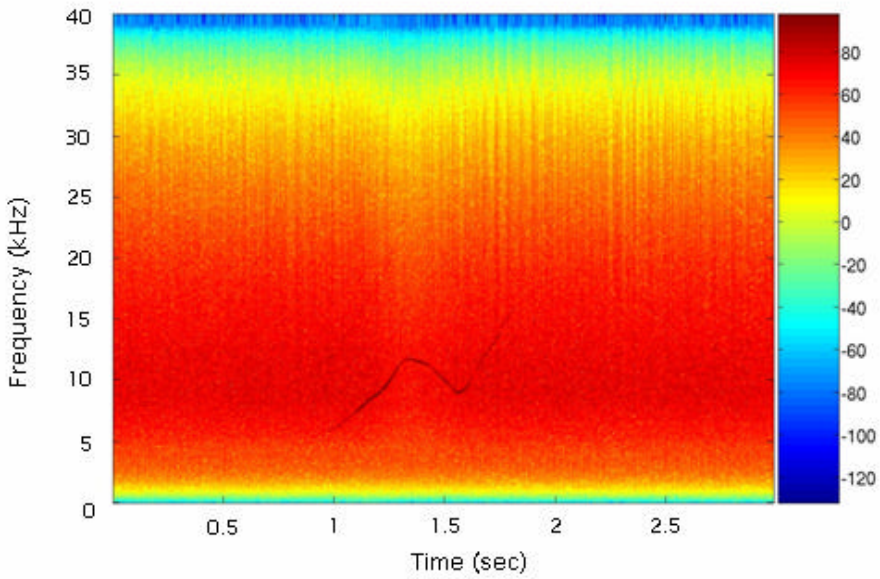

Figure 6.4: Spectrogram of Clip 1 received August 12, 2004, on H71 at 0501 GMT.

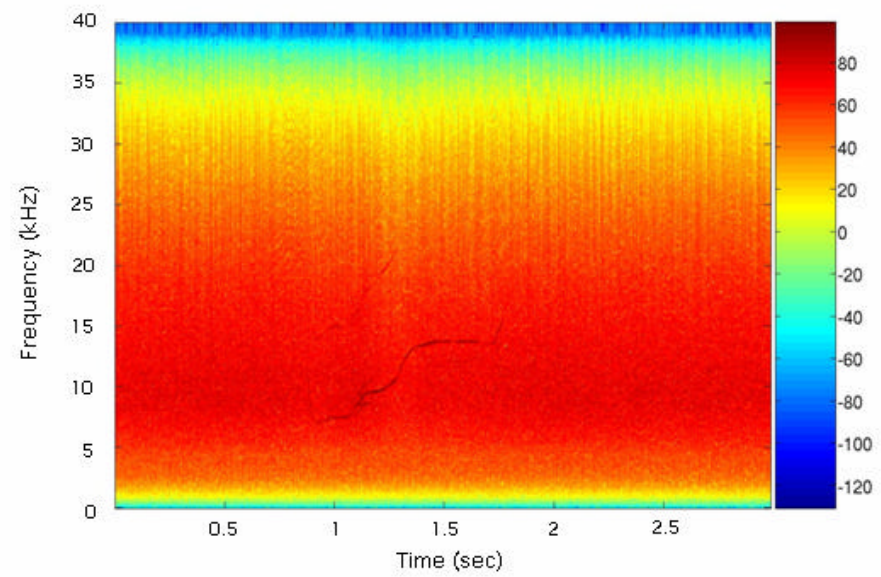

Figure 6.5: Spectrogram of Clip 2 received August 12, 2004, on H71 at 0503 GMT.

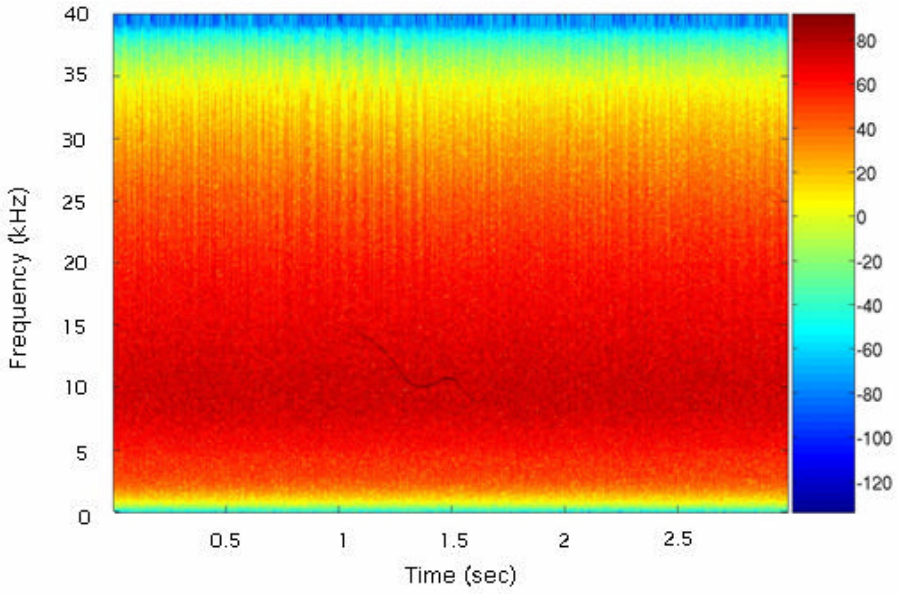

Figure 6.6: Spectrogram of Clip 3 received August 12, 2004, on H71 at 0505 GMT.

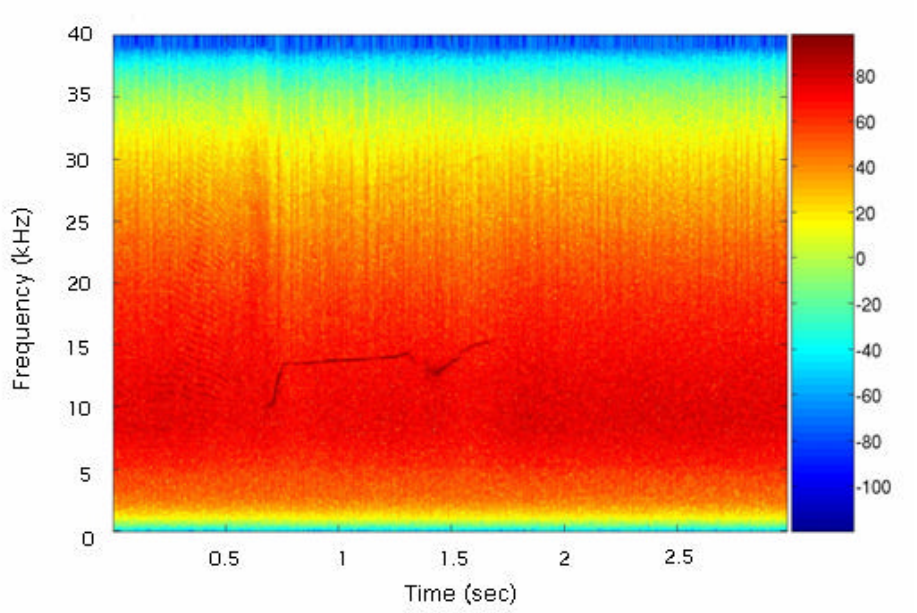

Figure 6.7: Spectrogram of Clip 4 received August 12, 2004, on H71 at 0612 GMT.

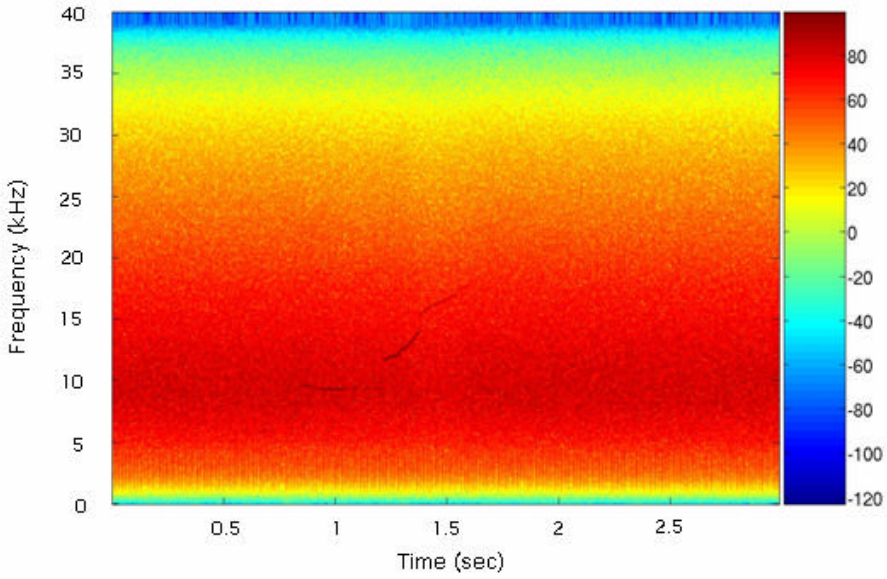

Figure 6.8: Spectrogram of Clip 5 received August 12, 2004, on H70 at 0613 GMT.

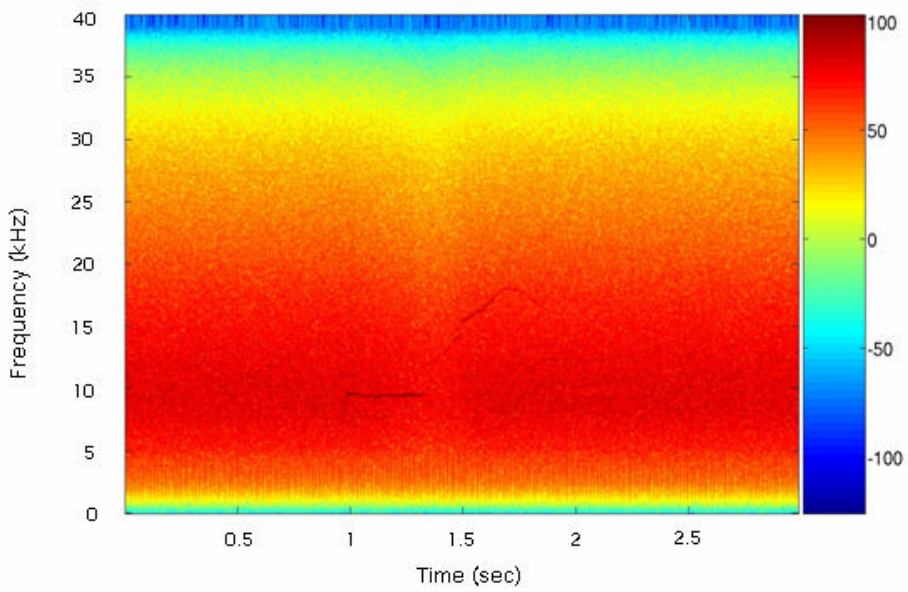

Figure 6.9: Spectrogram of Clip 6 received August 12, 2004, on H70 at 0614 GMT.

The objective in this study is to use wavelet multi-level decomposition to determine the root-mean square (RMS) energy of each vocalization in comparison to the range of each mammal from the respective hydrophones. The following two sections will describe the method in calculating the mammal's position and the multi-level decomposition process for each vocalization.

1. Time Difference of Arrival (TDOA)

The methodology to find the approximate position of the mammal which will be described in the remainder of this section was conducted by the Ocean Acoustics Laboratory at the Naval Postgraduate School, Monterey, CA. Before describing this calculative method, it is important to consider two assumptions. The first assumption is the sound speed is constant throughout the entire water column, averaging 1485 m/s. Therefore, only a direct propagation path is considered for each vocalization. The second assumption considers all hydrophones and mammals are in the same plane. Therefore, water depth is not taken into consideration in this process.

A 100×100 model grid was placed over the SOAR range (Fig 6.2, highlighted area) where the distance between each grid point was $1/10^{\circ}$, or approximately 94 m. Since these vocalizations were received on H70, H71, H77, and H78, the expected time of arrival (t_e) of the sound source was determined based on the range and location of the

grid point near or between the respective hydrophones. Since the mean sound speed (c) in this area is 1485 m/s and the distance (r) of the grid point can be determined from each hydrophone, the expected time of arrival is given by

$$t_e = \frac{c}{r}. \tag{6.1}$$

Finding the expected time difference of arrival (TDOA) first required finding the hydrophone closest to the grid point. Once t_e is determined from Eqn 6.1, the time lag $\Delta t_e = 0$ for that hydrophone. The expected TDOA (Δt_e) for the other hydrophones was calculated by subtracting t_e of each hydrophone and t_e of the closest hydrophone. Therefore, every grid point had its respective expected TDOA (Δt_e) with the four hydrophones (Fig 6.10).

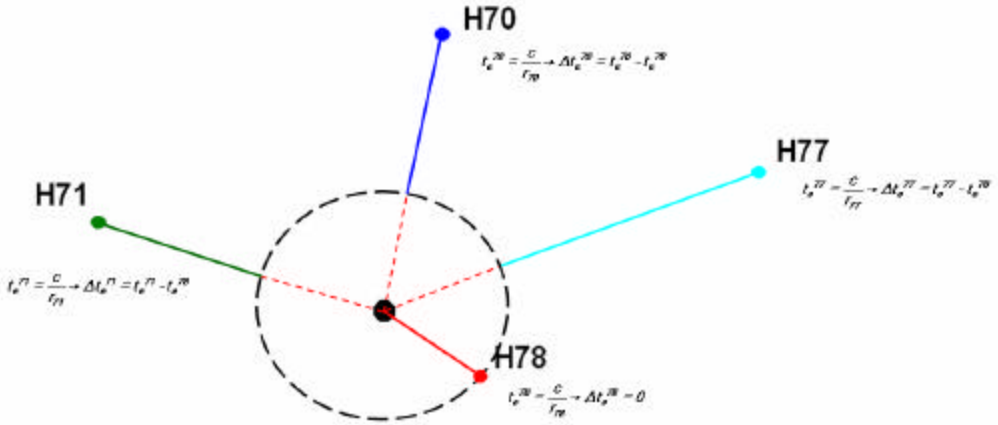

Figure 6.10: Example of expected TDOA (Δt_e) calculations for a given grid point.

Finding the observed TDOA for each clip first required finding the hydrophone with the strongest signal. Once determined, $\Delta t_o = 0$ for that hydrophone. The signal at the other hydrophones were then individually cross-correlated with the strongest signal over a 6 second period which found the time of maximum correlation between the two signals. Therefore, the time lag (Δt_o) for the signal at the each of the other hydrophones is equal to the time of maximum correlation minus the observed time of arrival (t_o) of the strongest signal.

For every grid point, the sum of squares difference was determined to find the approximate position of the mammal given by

$$\sum_{n=1}^{4} (\Delta t_o - \Delta t_e)_n^{\,2} \tag{6.2}$$

where $n = 1$ through 4 corresponds to H70, H71, H77, and H78, respectively. Note this was done for each clip and wherever the least sum of squares difference was located in the grid was the position of the mammal associated with that clip.

2. Multi-level Decomposition

Anticipating correlating the root mean square energy of the decomposed signal with the hydrophone range, each clip was decomposed separately with the Haar wavelet transform. Based on the size of each vocalization (240000×1), the maximum decomposition level for each clip was determined via a built-in function in the wavelet toolbox. For the Haar wavelet, the maximum decomposition level for each vocalization is $J = 16$. At this level, the signal was flattened and there were no distinct features. However, at level $J = 13$, each clip had several peaks that were representative of the energy in the signal. Therefore, the root mean square (RMS) energy was calculated at level $J = 13$ for each clip as received on all four hydrophones and was compared to the mammal's range from the respective hydrophone.

C. RESULTS

Clip 1 and 2 both came from a mammal at the same location: 32.792° N, -118.68° E; Clip 3 came from a mammal at 32.788° N, -118.678° E; Clip 4 came from a mammal at 32.786° N, -118.676° E; and Clip 5 and 6 came from a mammal at the same location: 32.762° N, -118.664° E. Clips 1 through 4 were located in the vicinity of H71 and Clip 5 and 6 are closest to H78 (Fig 6.11).

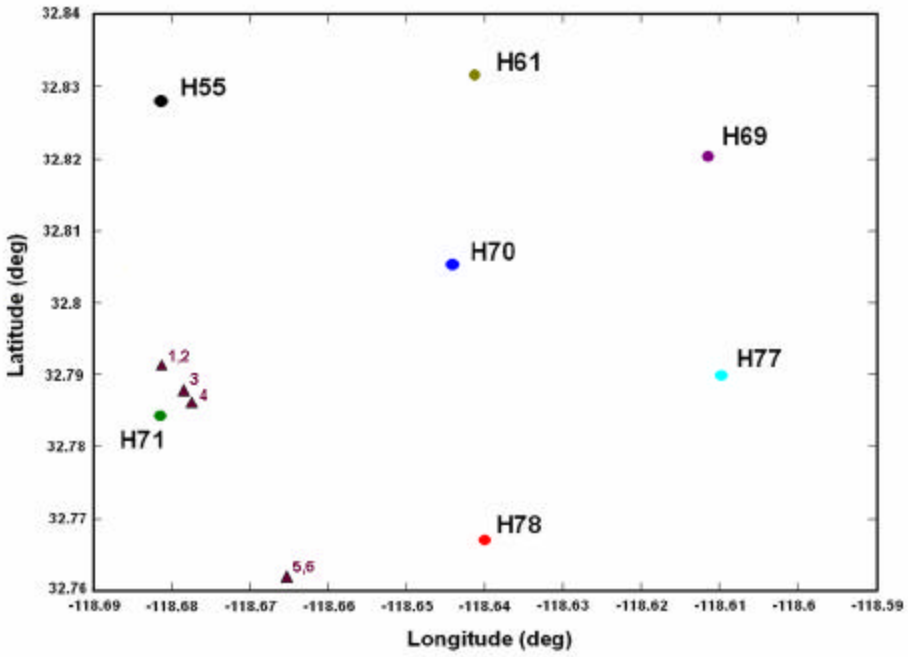

Figure 6.11: Mammal's position (clips 1 through 6) relative to the hydrophones.

Fig. 6.12 through 6.17 shows clips 1 through 6, respectively, decomposed through $J = 16$ levels. For clip 1, the closest hydrophone is H71 at 784 m, followed by H70 and H78 at 3792.5 m and 4735 m, respectively, and finally H77 at 6645.2 m. The RMS energy of clip 1 associated with these hydrophones is 15.08, 12.86, 11.4, and 11.41, respectively.

Similarly, for clip 2, the closest hydrophone is H71 at 784 m, followed by H70 and H78 at 3792.5 m and 4735 m, respectively, and finally H77 at 6645.2 m. The RMS energy of clip 2 associated with these hydrophones is 15.08, 19.7, 11.4, and 11.41, respectively.

For clip 3, the closest hydrophone is H71 at 436 m, followed by H70 and H78 at 3835 m and 4330 m, respectively, and finally H77 at 6451 m. The RMS energy of clip 3 associated with these hydrophones is 12.3, 13.6, 13.0, and 9.5, respectively.

For clip 4, the closest hydrophone is H71 at 480 m, followed by H70 and H78 at 3803 m and 4053 m, respectively, and finally H77 at 6272 m. The RMS energy of clip 4 associated with these hydrophones is 9.5, 13.7, 14.5, and 9.6, respectively.

For clip 5, the closest hydrophone is H78 at 2403 m, followed by H71 and H70 at 3011 m and 5272 m, respectively, and finally H77 at 5954 m. The RMS energy of clip 5 associated with these hydrophones is 8.7, 11.6, 16.1, and 9.0, respectively.

For clip 6, the closest hydrophone is H78 at 2403 m, followed by H71 and H70 at 3011 m and 5272 m, respectively, and finally H77 at 5954 m. The RMS energy of clip 5 associated with these hydrophones is 10.4, 10.2, 14.0, and 8.4, respectively.

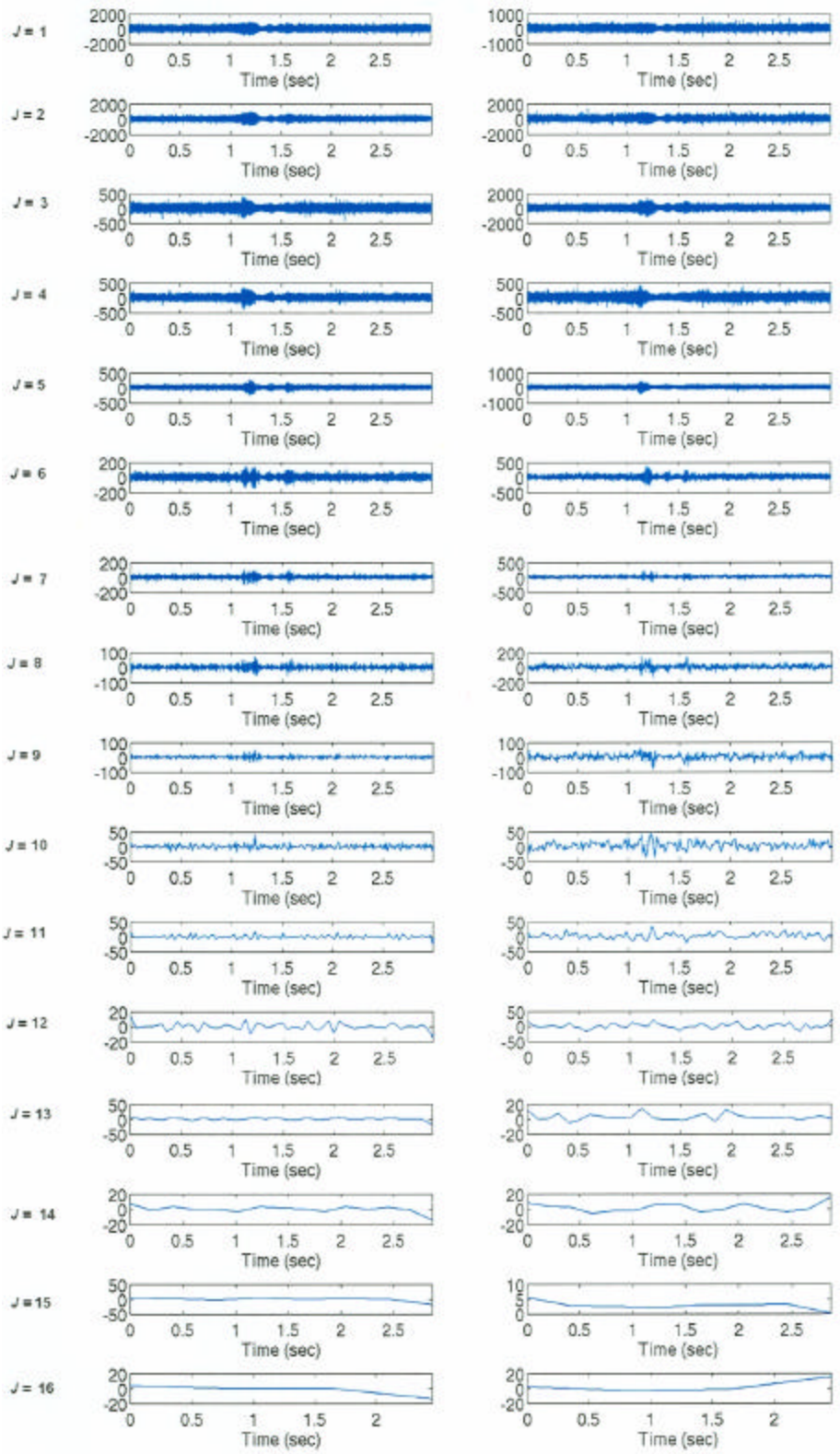

Figure 6.12: Multi-level decomposition for $J = 16$ levels of clip 1 using the Haar wavelet. The plots on the left are the low frequency content of the signal while the plots on the right are the high frequency content.

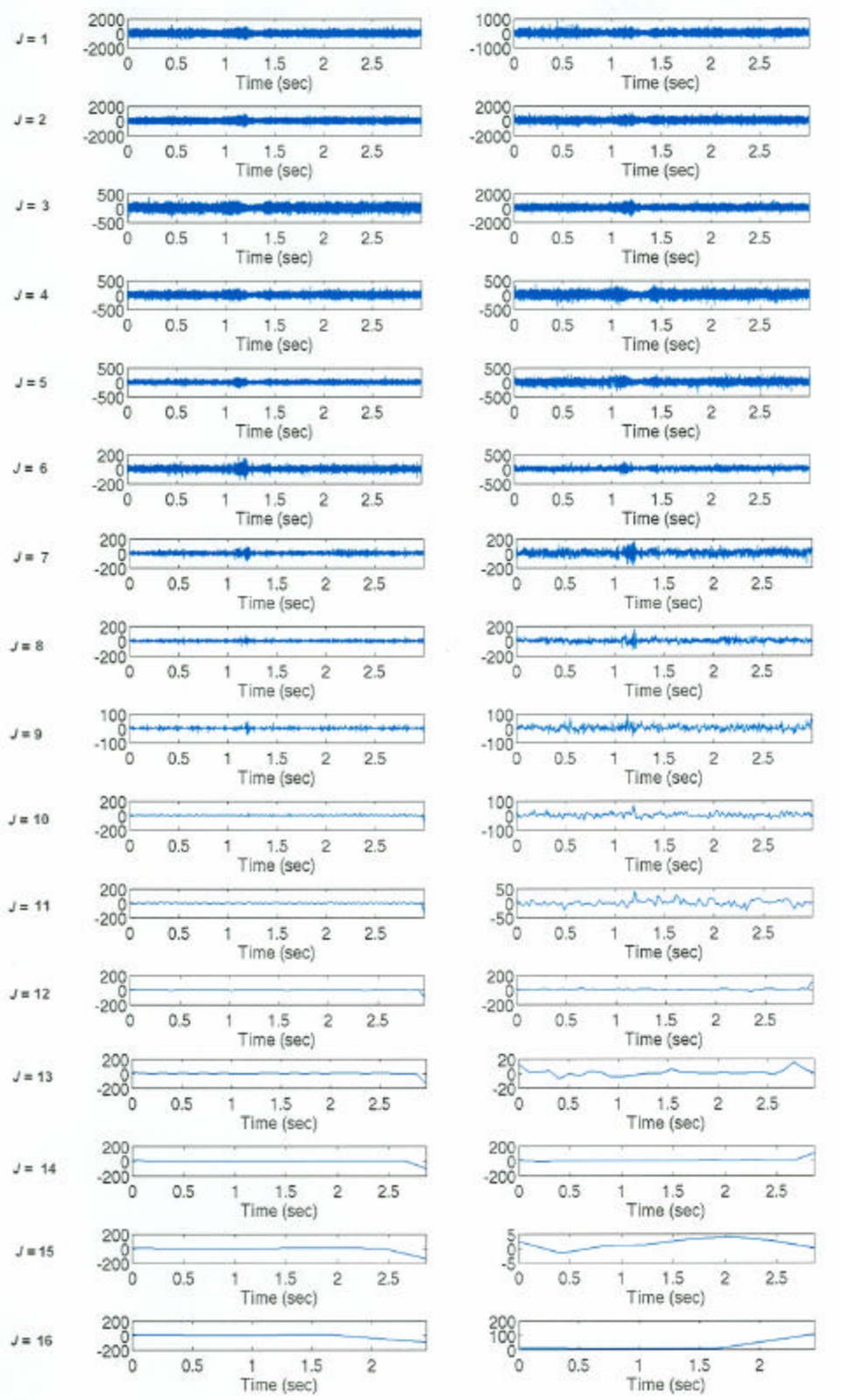

Figure 6.13: Multi-level decomposition for $J = 16$ levels of clip 2 using the Haar wavelet. The plots on the left are the low frequency content of the signal while the plots on the right are the high frequency content.

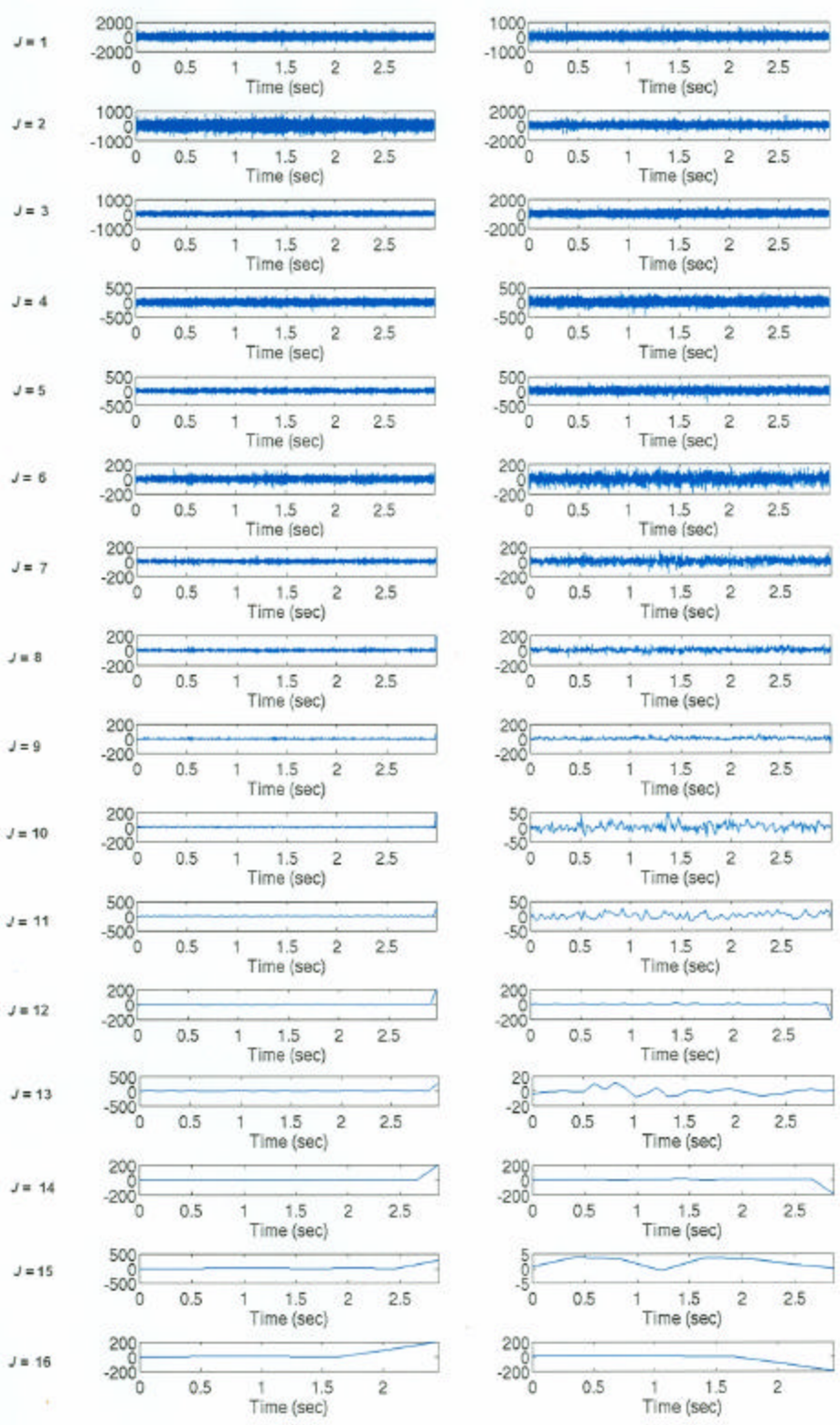

Figure 6.14: Multi-level decomposition for $J = 16$ levels of clip 3 using the Haar wavelet. The plots on the left are the low frequency content of the signal while the plots on the right are the high frequency content.

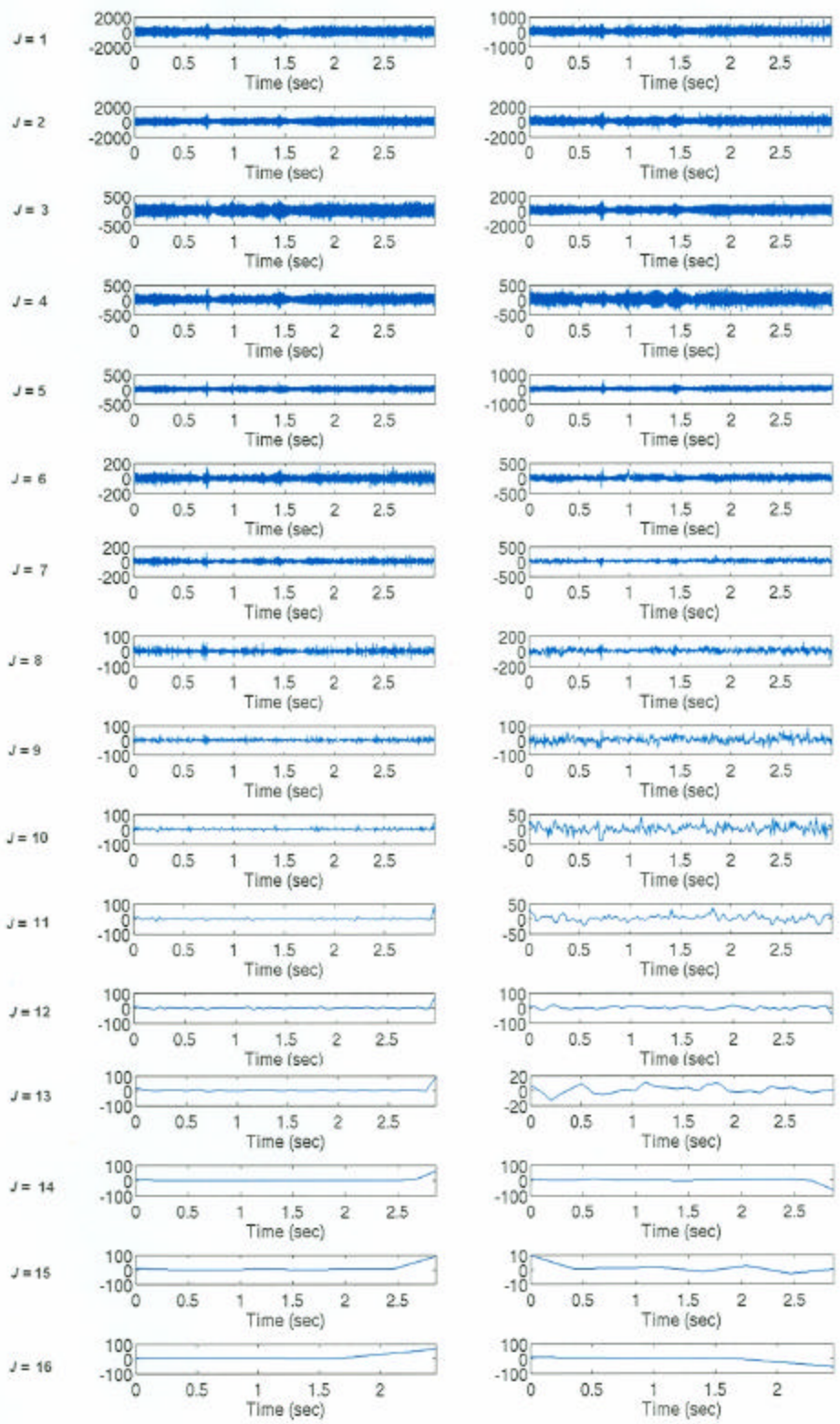

Figure 6.15: Multi-level decomposition for $J = 16$ levels of clip 4 using the Haar wavelet. The plots on the left are the low frequency content of the signal while the plots on the right are the high frequency content.

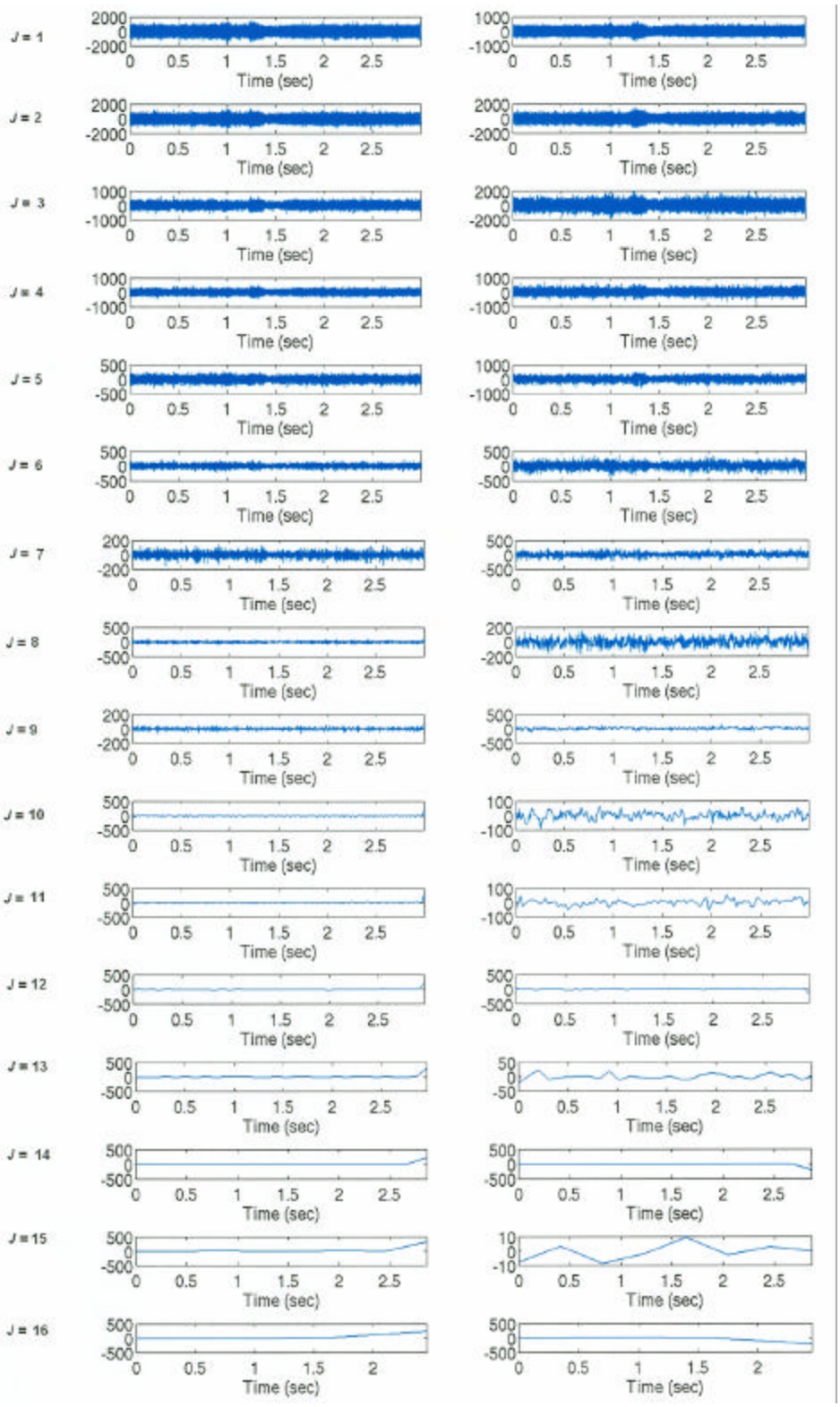

Figure 6.16: Multi-level decomposition for $J = 16$ levels of clip 5 using the Haar wavelet. The plots on the left are the low frequency content of the signal while the plots on the right are the high frequency content.

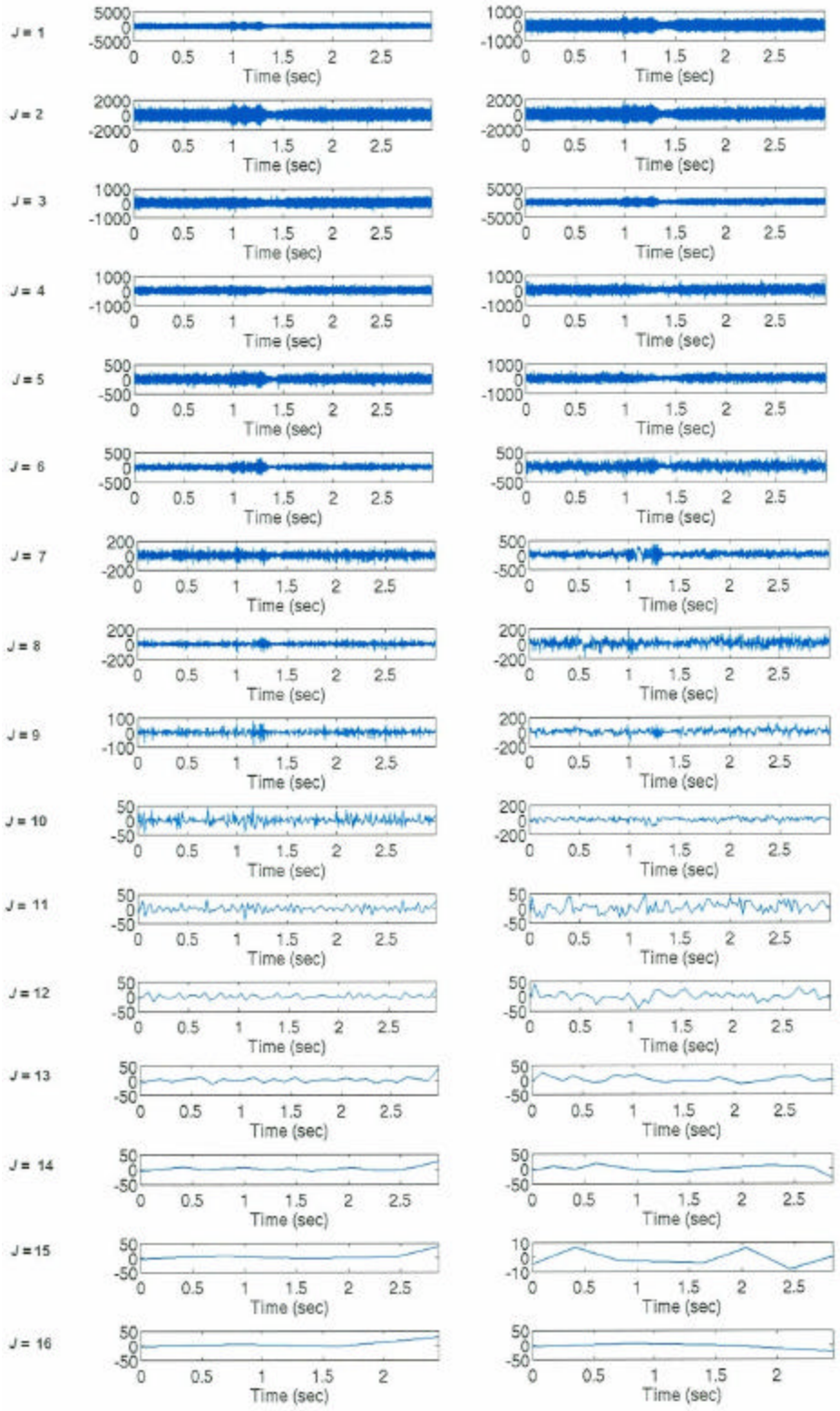

Figure 6.17: Multi-level decomposition for $J = 16$ levels of clip 6 using the Haar wavelet. The plots on the left are the low frequency content of the signal while the plots on the right are the high frequency content.

D. DISCUSSION

Assuming a constant source level, the comparison of the root mean square (RMS) energy of each wavelet decomposed clip to the mammal's range from the respective hydrophones shows the potential of this process to provide a near real time, first order estimate of range. Fig 6.18 shows the RMS energy of each clip as measured at each hydrophone versus the range of the mammal from that corresponding hydrophone.

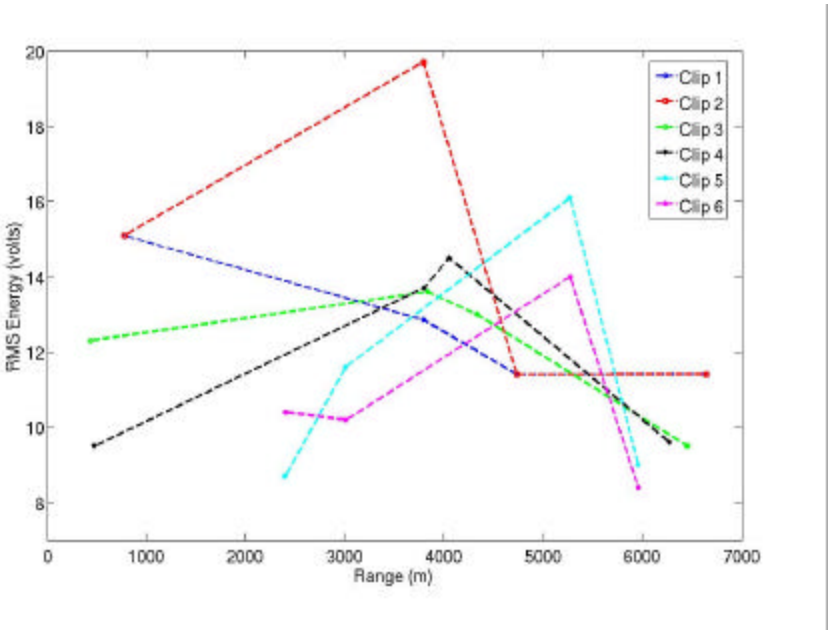

Figure 6.18: Root mean square (RMS) energy of each clip versus range of the mammal from the hydrophone. The first point is the RMS energy of the vocalization received on the closest hydrophone; the second point is the RMS energy received on the next closest hydrophone, and so on.

The first point of each clip in Fig 6.18 corresponds to the RMS energy of the vocalization received at the closest hydrophone; the second point corresponds to the RMS energy of the same vocalization as received at the next closest hydrophone, and so on. For example, the closest hydrophone to the mammal associated with clip 1 (blue dashed line) is H71, followed by H70, H78, and H77, respectively. For the other clips, refer to the previous section for the order of hydrophones.

Clip 1 (Fig 6.18, blue dashed line) shows that the maximum RMS energy is received at the closest hydrophone. As the vocalization is received at the other hydrophones (in terms of increasing range), the RMS energy decreases. This directly

corresponds to high frequency transmission loss; as range increases, the intensity of the high frequency vocalization decreases due to absorption in sea water.

Clip 2 (Fig 6.18, red dashed line) shows the exact same relationship to clip 1 except for the second point (associated with the second closest hydrophone, H70). The RMS energy is its maximum at H70; the RMS energy of the other three points is exactly equal to the RMS energy of the first, third, and fourth points of clip 1 (associated with H71, H78, H77, respectively). Since clip 1 and clip 2 are in the same location and the first, third, and fourth points have exactly the same RMS energy, it is considered that these vocalizations came from the same mammal. The reasoning for the maximum RMS energy at H70 (clip 2, second point) may be due to a multiple path arrival of the vocalization at that hydrophone. However, the sound speed profile is not known for that region and it is difficult to determine if that was in fact the case.

Clip 3 (Fig 6.18, green dashed line) and clip 4 (Fig 6.18, black dashed line) have their maximum RMS energy at the second closest hydrophone, H70, and the third closest hydrophone, H78, rspectively. Clip 3 and clip 4 are both located near H71 (Fig 6.11); however, their maximum RMS energy is at H70 and H78, respectively. Zimmer *et al.* (2005) discusses the three-dimensional beam pattern of a sperm whale, which falls under the *Odontocetes* suborder (Fig 6.19).

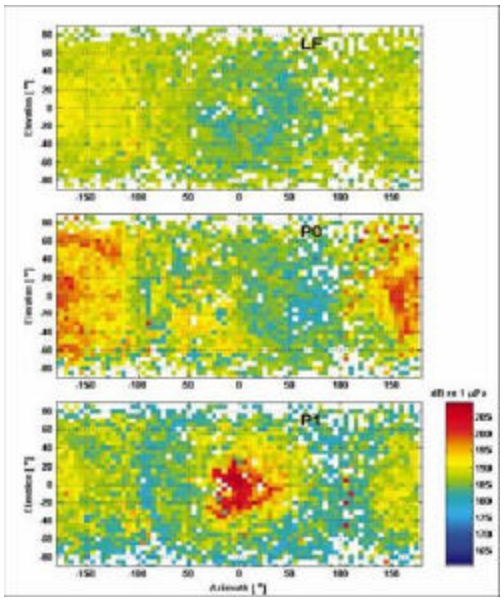

Figure 6.19: Beam pattern of three components of clicks recorded from a tagged sperm whale (From Zimmer *et al*., 2005).

For sperm whales, Zimmer *et al.* (2005) observes that the three-dimensional beam pattern can be viewed in terms of azimuth and elevation. It is important to note that the three plots in Fig 6.19 use a coordinate as seen by the whale. The center of each plot indicates an azimuth and elevation of 0°. This corresponds to the direction directly in front of the whale. Negative azimuth values indicate angles to the left of the whale, positive azimuth to the right. Similarly, positive elevation indicates angles above the horizontal, while negative angles are downward.

Figure 6.19 shows peak-level bean pattern of the LF component (top), the P0 pulse (middle), and the P1 pulse (bottom). Zimmer *et al*. (2005) confirms a nearly omnidirectional LF component with maximum levels ranging from ~ 170-190 dB_{peak} *re:* 1 mPa at 1 m, the P0 beam pattern pointing backwards with low directionality at maximum levels of ~ 200 dB_{peak} *re:* 1 mPa at 1 m and the P1 component pointing forward with high directionality and a maximum measured level of 210 dB_{peak} *re:* 1 mPa at 1 m.

If the mammals associated with clips 3 and 4 were facing away from H71, the low directionality and a lower source level associated with the beam pattern pointing backwards could explain why the RMS energy of the vocalization received at H71 was less than that received at H70. Additionally, as the clip 3 is received at the other hydrophones (in terms of increasing range), the RMS energy decreases. This directly corresponds to high frequency transmission loss as discussed with clip1; as range increases, the intensity of the high frequency vocalization decreases due to absorption in sea water. For clip 4, if the mammal may have been facing more towards H78, the high directionality and higher source level associated with the beam pattern pointing forward could explain why its RMS energy is slightly higher at H78 than at H70.

Clip 5 (Fig 6.18, light blue dashed line) and clip 6 (Fig 6.18, pink dashed line) show a very different pattern than the other clips. The maximum RMS energy for both clips is at their third closest hydrophone, H70. Although both clips are closest to H78, the mammals associated with these clips could be facing more towards H71 which could explain overall the lower RMS energy received at H78. Additionally, both clips have similar peaks associated with their maximum RMS energy. This could be an indication

of multiple arrival paths of the vocalizations to H70 via surface reflection and bottom bounce. Similar to the case with clip 2, the sound speed profile is not known for that region and it is difficult to determine if that was in fact the case.

Additionally, the hydrophones that received these vocalizations have automatic gain control (AGC) which means they automatically adjusted the vocalization intensity in a specified manner as function of the received signal level. The AGC levels were unknown and not considered for this study which, if known, may have explained our results. Therefore, for future studies, the AGC levels of the hydrophones would have to be known and accounted for to make this a systematic process.

E. FUTURE RESEARCH

Although this thesis shows potential in providing a near real time, first-order estimate of range using wavelets, a more extensive, in-depth study is needed to validate this process. Without knowing the sound speed profiles at the time these vocalizations were recorded, the AGC levels of the hydrophones, and the vocalization source levels, the results can only suggest the physical possibilities as a function of decomposing each vocalization with wavelets. Additionally, the small sample space limits the resourcefulness of this method. Proficiency would require that more vocalizations are decomposed and analyzed in a similar manner.

The three-dimensional beam pattern in Zimmer *et al*. (2005) demonstrates that marine mammal vocalizations should be modeled to determine the manner in which the mammal propagates sound. Additionally, these vocalization models should operate in conjunction with sound propagation models. The sound propagation models will acknowledge the appropriate geometric configurations and physical considerations of the sound propagation paths in a given area. Therefore, based on the marine mammal type and the sound propagation paths in conjunction with wavelet decomposition, the model could provide a near real-time, first-order estimate of range.

VII. CONCLUSION

The wavelet-based techniques as demonstrated in this thesis show the potential in providing viable information for these different acoustic data sets. For the alewife study, applying the Mexican Hat and Morlet continuous wavelet transforms to the received backscattered signal (v_{bs}^{R}) revealed an approximation of the absolute signal intensity for the transducers that were at three different angles of incidence. More importantly, the target strength of v_{bs}^{R} estimated over all scales and all angles were within the range of target strengths over the frequency band from Reeder *et al*. (2004), demonstrating that the procedure is the correct methodology and a reasonable attempt at a first order approximation of absolute target strength using wavelets. Since the peaks and nulls in the target strength associated with the constructive and destructive interference are not apparent, it is obvious that the Morlet and Mexican hat wavelets do not optimize or enhance the features of the received backscattered signal. The wavelet based transform acts a partial wave target strength which is expected based on the mathematics. This reveals the limitations of the built-in functions in MATLAB on this type of signal and the need for a wavelet-based algorithm designed specifically for such complex acoustic signals.

Additionally, the multi-level decomposition of v_{bs}^{R} with the Daubechies and Symmlet wavelets demonstrated that the time delay of the two largest peaks of the normalized compressed output (CPO) closely correlates with a physical separation between the skull and swimbladder of the fish. Although not exact, it shows the capability of wavelets to depict the relationship as discovered in Reeder *et al*. (2004). Since MATLAB's built-in wavelet functions do not incorporate all the mathematically available wavelet basis functions, signal processing of v_{bs}^{R} with wavelets for the purpose of this thesis requires the development of a wavelet-based algorithm as given in Meyers *et al*. (1993).

For the marine mammal study, the multi-level decomposition of six *Odontecetes* vocalizations with the Haar wavelet revealed the potential of wavelets to provide a near

real time, first-order estimate of range from a passive receiver. By decomposing these vocalizations, the physical expectation of high frequency attenuation as a function of range was only unmistakably revealed in clip 1. The three-dimensional beam pattern discovered by Zimmer *et al.* (2005) could be a plausible explanation of the patterns of the RMS energy for the other vocalizations as it is received on each of the four hydrophones. Additionally, multiple arrivals via different propagation paths could also explain some of the behavior of the RMS energy of these vocalizations as they were received on the hydrophones.

However, a small sample space and a lack of environmental data in regards to the sound speed profile in addition to the unknown AGC levels of the hydrophones and the constant source level assumption are significant limitations in establishing this method as a systematic process. If a larger number of vocalizations were decomposed with the Haar wavelet and analyzed by its RMS energy at each receiver accounting for the limitations found in this thesis, it is conceivable that this wavelet-based method could become a favorable algorithm for determining the range of a marine mammal from a passive receiver. However, more extensive research is needed to validate this methodology.

Overall, despite the lack of statistical analysis, this thesis demonstrates that wavelets can provide viable information as it pertains to these particular acoustic data sets. Using only built-in functions in MATLAB limits the data processing ability; however, with further research and development, wavelets may provide a promising alternate method in processing acoustic scattered signals and marine mammal vocalizations.

LIST OF REFERENCES

Barsanti, R.J., 1996: Denoising of Ocean Acoustic Signals Using Wavelet-Based Techniques. Master's Thesis, Department of Electrical and Computer Engineering, Naval Postgraduate School, 104 pp.

Chui, C.K., 1992: *Wavelets: A Tutorial in Theory and Applications*. Academic Press, Inc., 723 pp.

Daubechies, I., 1992: *Ten Lectures on Wavelets.* Society for Industrial and Applied Mathematics, 357 pp.

Farge, M., 1992: Wavelet transforms and their applications to turbulence. *Annu. Rev. Fluid Mech.*, **24**, 395-457.

Graps, A., 1995: An Introduction to Wavelets. *IEEE Comp. Sc. & Eng.*, **2(2)**, 50-61.

Kumar, P., and E. Foufoula-Georgiou, 1997: Wavelet Analysis for Geophysical Applications. *Rev. Geophys.*, **35(4)**, 385-412.

Kobayashi, M., 1998: *Wavelets and Their Applications: Case Studies*. Society for Industrial and Applied Mathematics, 142 pp.

Mackenzie, D., 2001: *Wavelets: Seeing the Forest and Trees*. National Academy of Sciences, 8pp. [http://www.beyonddiscovery.org/content/view.article.asp?a=1952]. Sept 05.

Meyers, S.D., B.G. Kelly, and J.J. O'Brien, 1993: An introduction to wavelet analysis in oceanography and meteorology: With application to the dispersion of Yanai waves. *Mon. Wea. Rev*., **121**, 2858-2866.

Rao, R.M., and A.S. Bopardikar, 1998: *Wavelet Transforms: Introduction to Theory and Applications*. Addison Wesley Longman, Inc., 310 pp.

Reeder, D.B., J.M. Jech, and T.K. Stanton, 2004: Broadband acoustic backscatter and high-resolution morphology of fish: Measurement and modeling. *J. Acoust. Soc. Am.*, **116**(2), 747-761.

Sturgeon, W.J., 2002: *San Clemente Island – A Chronological Military History (1932-2000)*. Central Plains Book Manufacturing, 98 pp.

The Math Works, Inc., 2004: Wavelet Toolbox User's Guide Version 3.0.1. The MathWorks, Inc.

Torrence, C. and G.P. Compo, 1998: A practical guide to wavelet analysis. *Bull. Am. Meteorol. Soc.*, **79**, 61-78.

Zimmer, W.M.X., P.L. Tyack, M.P. Johnson, and P.T. Madsen, 2005: Three-dimensional beam pattern of regular sperm whale clicks confirms bent-horn hypothesis. *J. Acoust. Soc. Am.*, **117**(3), 1473-1485.

THIS PAGE INTENTIONALLY LEFT BLANK

BIBLIOGRAPHY

Hubbard, B. B., 1998: *The World According to Wavelets: The Story of a Mathematical Technique in the Making*. A K Peters, Ltd., 330 pp.

Mallat, S., 1999: *A Wavelet Tour of Signal Processing*. 2nd ed. Academic Press, 637 pp.

Medwin, H. and C. Clay, 1998: *Fundamentals of Acoustic Oceanography*. Academic Press, 712 pp.

Mix, D.F. and K.J. Olejniczak, 2003: *Elements of Wavelets for Engineers and Scientists.* John Wiley & Sons, Inc., 236 pp.

Strang, G. and T. Nguyen, 1997: *Wavelets and Filter Banks.* Wellesley-Cambridge Press, 520 pp.

Urick, R.J., 1983: *Principles of Underwater Sound*. 3rd ed. McGraw-Hill, Inc., 423 pp.

Ziomek, L..J., 1995: *Fundamentals of Acoustic Field Theory and Space-Time Signal Processing.* CRC Press, Inc., 692 pp.

THIS PAGE INTENTIONALLY LEFT BLANK

INITIAL DISTRIBUTION LIST

1. Defense Technical Information Center
   Ft. Belvoir, Virginia

2. Dudley Knox Library
   Naval Postgraduate School
   Monterey, California

3. Dr. Mary L. Batteen, Chair
   Department of Oceanography
   Naval Postgraduate School
   Monterey, CA

4. CDR D. Benjamin Reeder, USN
   Department of Oceanography
   Naval Postgraduate School
   Monterey, CA

5. Dr. John A. Colosi, Code OC
   Department of Oceanography
   Naval Postgraduate School
   Monterey, CA

6. LT Elizabeth M. Scheidecker, USN
   Operations Department
   Naval Maritime Forecasting Center
   Pearl Harbor, HI